Journal of Engineering, Emerging Technologies and Applied Sciences -– Volume 1 Issue 2, Nov. 2023

Available at ***https://www.ndu.edu.ng/journalofengineering/***

RESEARCH ARTICLE OPEN ACCESS

Bioremediation of Crude Oil Polluted Soil Using a Blend of NPK Fertilizer and Periwinkle Shell Ash

Blessing Zekieni Yelebe, Zekieni Robert Yelebe

Department of Chemical Engineering, Niger Delta University, Bayelsa State, Nigeria

byelebs@gmail.com

----------**********----------

Abstract:

Analysis on the bioremediation of crude oil polluted soil using a blend of NPK (15-15-15) fertilizer and Periwinkle Shell Ash (PSA) is presented. The analysis involves using 7-batch bioreactors under aerobic conditions with each bioreactor containing 2 kg of soil sample and spiked with 200 ml of crude oil except for the control experiment, and were properly mixed and periodically tilled during the experimentation period of 90 days. The substrate concentration was analysed as Total Petroleum Hydrocarbon (TPH) while the microbial concentrations Total Heterotrophic Bacteria (THB) and Hydrogen Utilising Bacteria (HUB) was also analysed, including the soil pH, during the period. Soil parameters (nitrogen, organic compound, phosphorus and potassium) were also measured at the beginning and at the end of the experiments. The results showed that THB increased with time from 6.0×10^5 cfu/g to 3.02×10^8 cfu/g for the control experiment, to 3.3×10^8 cfu/g for sample with 100 g NPK, to 3.95×10^8 cfu/g for sample with 100 g NPK and 200 g PSA during the period. HUB also increased from 2.74×10^4 cfu/g to 4.45×10^7 cfu/g for the sample during the same period. TPH values reduced from 58,200 mg/kg to 34,591 mg/kg for the control and to 18,045 mg/kg been the lowest for sample with 100 g NPK and 500 g PSA during the same period. pH values varied from 5.7 – 8.8 for all sample during the experimentation. Also nitrogen increased from 0.42% to 0.91%, organic carbon from 1.65% to 1.78%, organic matter from 2.58% to 3.20% phosphorus from 26.8% - 31.57%, and potassium from 0.35% - 0.46%.

Keywords — **Bioreactors, Biodegradation, Monod growth kinetics, substrate concentration, Total Heterotrophic Bacteria**

----------**********----------

I. INTRODUCTION

Crude oil pollution, as a result of exploration, exploitation, production and processing operations is an environmental challenge globally and particularly in Nigeria's Niger Delta area (Odukoya, Lambert and Sakrabani, 2019). For the past forty years of petroleum exploration and exploitation in Nigeria, over 6000 cases of crude oil spills have been recorded with an average of about 150 crude oil spills per year (Department of Petroleum Resources, 1997). Crude oil spills into the environment may be from technical errors, deliberate human sabotage (vandalism), transportation problems and storage faults (Khamehchiyan, Hossein and Tajik, 2007; Ajagbe, Omokehinde, Alade and Agbede, 2012; Ivshina, Kuyukina, Krivoruchko, Evkin, Makaraov, Cummngham, Peshkur, Allas, and Philip, 2015; Ndimele, Saba, Ojo, Ndimele, Anetekhai, and Erondu, 2018).

II. RELATED LITERATURES

Schmidt-Etkin 2011, observed that although large spills may sometimes occur with severe environmental and socio-economic damage, small spills are often more common. The impacts and damages as a result of crude oil spills depends generally depend on the spill location, the type of crude oil, the volume of the spill, the closeness to sensitive or critical resources and the season it occurred, for example in Nigeria whether rainy or dry season, among other factors (Schmidt-

Etkin,2011). Odukoya *et al.*, 2019 explained in their work, that a significant part of the petroleum hydrocarbon contamination in the world is as a result of large-scale accidents of crude oil spills. They further explained that, there are more cases of crude oil spills on land, than those recorded in aquatic environment in which plant life especially in farmland becomes exposed to petroleum hydrocarbon with subsequent effects on agricultural produce.

In Nigeria for example, there is significant spillage of crude oil into the environment from various sources including leakages of crude oil pipelines, human sabotage, damaged crude oil tankers and storage vehicles, oil tankers overflow, equipment failures, technical errors (Nas, 1975; Nicolotti and Egli, 1998). Bioremediation is defined as the use of micro-organisms for the degradation or removal of environmental pollutants in an established and feasible technique and is now being used for the removal of crude oil contaminants from soil (Yelebe, Samuel, Yelebe, 2015). Bacteria that metabolize naturally occurring hydrocarbons such as petroleum hydrocarbon are wide spread in the environment (Yelebe et al., 2015).

The environmental consequences of crude oil pollution are enormous. Crude oil spills, especially in the Niger Delta have destroyed agricultural lands, traditional fishing grounds, fishing ponds etc. Studies have shown that, there is a reduction in soil fertility leading to low productivity and hence, the need for a solution (Odjuvwuederhie, Douglason and Adun, 2006; Osuagwu, Okigbo, Ekpo, Chukwurah, and Agbor, 2013). Insufficient aeration of the soil as a result of the oil pollution has been observed to be the major contributing factor to the retarded growth identified in plants and the chlorosis of the leaves (Udo and Fayemi, 1975).

Considering the overall adverse effects of crude oil pollution and consequently, its implications on food security and environment in the oil rich Niger Delta region, it has become increasingly necessary to develop new technology or improve on the existing technologies on the treatment of the crude oil polluted soils to mitigate the food security crises.

III. MATERIALS AND METHODOLOGY

Materials used for this work include; crude oil, Periwinkle shell ash, NPK fertilizer,Soil sample, GC/MS.

A. Methods

The method in this research involves the collection and preparation of the following samples:

1. Crude Oil Sample:mCrude oil (Bonny light) was obtained from Agip flow station in Brass, Bayelsa State, Nigeria.
2. Periwinkle Shell Sample: Periwinkle shell (Tympanotomus Fuscatus Specie) samples used for this experiment were collected from Amassoma waste dump in Southern Ijaw Local Government Area of Bayelsa State.
3. Preparation of Periwinkle Shell Ash: Fresh periwinkle shells were weighed, then heated in an oven to a temperature of 1000oC, and then weighed again. Fine particles were obtained using a 2mm mesh after the periwinkle shells have been crushed.
4. NPK Fertilizer: N.P.K fertilizer used for this work was obtained from Rivers State Ministry of Agriculture, Port-Harcourt.

B. Chemical Analysis of Periwinkle Shell Ash

Results of chemical analysis of the Periwinkle shell ash was obtained from literature and presented in Table 1

TABLE I
CHEMICAL ANALYSIS OF PERIWINKLE SHELL (SOURCE: UKPAKA AND OKOCHI, 2018)

Element	Content	Element	Content	Element	Content
Mg	0.0000	Cr	0.0000	Ca	60.5899
Al	0.3685	Mn	0.0079	Ti	0.0000
Si	0.3033	Co	0.0007	V	0.0041
P	0.2704	Fe	0.1604	Zn	0.0436
S	0.4609	Ni	0.0261	As	0.0000
K	0.0000	Cu	0.0230	Pb	0.0000

.

C. Collection and Preparation of Soil Sample

Random collection of soil samples from fallow land that is not polluted with crude oil within the Niger-Delta University was done using a shovel and hand auger digging up to 20 cm. The collected soils were homogenized and air dried for a period of one week in a clean well-ventilated laboratory and sieved by passing through a 2 mm mesh sieve to remove stones, sticks and any unwanted particles. 2 kg of soil was each measured into clean dry experimental planting containers and moistened with distilled water to ensure proper mixing with the crude oil.

D. Characterization of Soil Samples

Standard procedures using Boyoucus hydrometer method to carry out the physical and chemical analysis of the soil sample was followed (Sheldrick & Wang, 1993).

E. Total Petroleum Hydrocarbons (TPH) Determination

The method of Ahmadi *et. al*. (2006), which is described in ASTM D3291 was used. This is the standard method for TPH extraction.

F. Preparation of Broth Culture

The broth culture was prepared by seeding three different types of bacteria obtained from soil into medium containing vital broth nutrient at a pH of 7.4. Before been used for the study, the inoculated broth was incubated for 24 hours at 37oC. These experiments were carried out at the Microbiology Laboratory of the Department of Biological Science, Niger Delta University, Bayelsa State.

G. Experimental Procedure

2 kg of soil sample was put into each container, and 200 ml of crude oil was measured and poured into the container also. Proper mixing was done to achieve 10% pollution as reported by Osuji and Adesiyan (2005). In variation, 100 g, 200 g, and 300 g and 500 g of the periwinkle shell ash were added to the containers and 100 g of N.P.K fertilizer respectively and thoroughly mixed to obtain homogeneity, for one week with constant watering to allow proper decomposition.

The first container having 2 kg of crude oil polluted soil served as control 1, while the second container, containing 200 ml of crude oil stimulated soil plus 100 g of NPK served as control 2, another container, containing 200 ml of crude oil stimulated soil and 500 g periwinkle shell ash, control 3, and the fourth, fifth, sixth and seventh containers, containing 200 ml of crude simulated soil with variations of 100 g, 200 g, 300 g and 500 g of periwinkle shell ash plus 100 g of NPK fertilizer were set up. Standard procedure as described by Ofunne (1999) was used in the enumeration and isolation of THB.

IV. RESULTS AND DISCUSSION

A. Microbial Population Evaluation

Bioremediation of Petroleum hydrocarbon polluted soil was investigated using a combination of NPK fertilizer and Periwinkle Shell Ash (PSA) to stimulate the population of the indigenous micro-organisms: The baseline bacterial count for the total heterotrophic bacteria (THB) and hydrocarbon utilizing bacteria (HUB) obtained were 6.0 × 105 cfu/g and 2.74 × 104 cfu/g respectively. THB and HUB increased progressively during the period of study.

Figure 1 is a comparative plot of changes in THB against time for crude oil polluted soil for three different cases (i.e., (1) control (2) only NPK, and (3) a blend of NPK and PSA). THB increased progressively from an initial value of 6.0×10^5 cfu/g at the beginning of the experiment to 2.64×10^8 cfu/g after 30 days and then to 3.02×10^8 cfu/g after 60 days of experimentation for the control experiment. The increase showed that indigenous micro-organism in the solid have the ability to use petroleum hydrocarbon as a carbon source and energy. This has been reported by other researchers (Rosenberg and Ron, 1996).

The THB counts for crude oil polluted soil amended with 100 g of NPK fertilizer was higher compared to the counts for the control experiment. From the same initial value of 6.0 × 105 cfu/g at the commencement of the experimental process, the THB increased to 2.88 × 108 cfu/g after 30 days and then to 3.3 × 108 cfu/g after 60 days of experiments,

figures higher than that of the control process. This could be ascribed to be the effect of the NPK fertilizer as these nutrients are necessary for bacterial growth and degradation activities (Gadhvi, 2019; Ekenwosu, 2019).

TABLE III
RESULTS OF MICROBIAL POPULATION DURING THE EXPERIMENTATION PROCESS

	Sample \ Time	0 day	30 days	60 days
THB values in cfu/g	Control	6.0×10^{5}	2.64×10^{8}	3.02×10^{8}
	100 g NPK	6.0×10^{5}	2.88×10^{8}	3.3×10^{8}
	100 g NPK + 200 g PSA	6.0×10^{5}	2.95×10^{8}	3.95×10^{8}
HUB values in cfu/g	Control	2.74×10^{4}	2.31×10^{5}	2.59×10^{6}
	100 g NPK	2.74×10^{4}	2.6×10^{7}	3.33×10^{7}
	100 g NPK + 200 g PSA	2.74×10^{4}	4.2×10^{7}	4.45×10^{7}

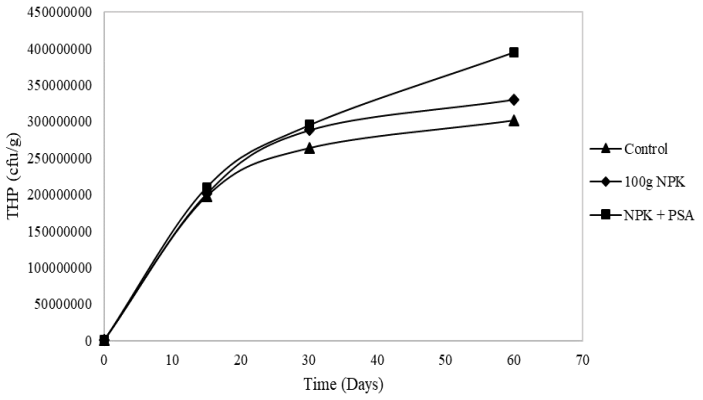

Figure 1: Plot of comparative changes in THB with time

For crude oil polluted soil amended with a blend of 100 g NPK fertilizer and 200 g PSA. As clearly seen, THB count increased from 6.0 × 105 cfu/g to 2.95 × 108 cfu/g after 30 days and increased further to 3.95 × 108 cfu/g after 60 days of experimentation, given values for THB higher than the control experiment and that when only NPK fertilizer was used. This trend is supported by studies carried out by Obiakalaije et. al., 2015; Oyedele and Amoo, 2014; Adesodu and Mbagwu, 2008; Ijah and Antai, 2003, and Nakasaki et. al., 1992.

The changes in the hydrocarbon utilizing bacteria (HUB) count also followed the same pattern in all three cases. For Figure 2, HUB increased from 2.74 × 104 cfu/g at the commencement of the experiment to 2.3 × 105 cfu/g after 30 days and to 2.59 × 106 cfu/g after 60 days of the experimentation process for the control experiment.

For the sample amended with 100 g of NPK fertilizer, HUB grew from 2.74 × 104 cfu/g to 2.6 × 107 cfu/g after 30 days and further increased to 3.33 × 107 cfu/g after 60 days.

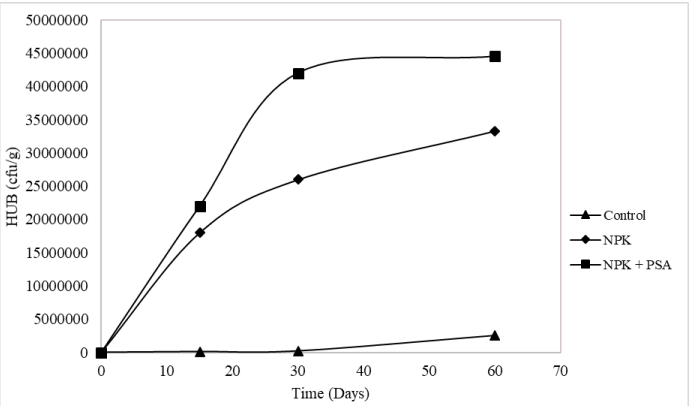

Figure 2: Plot of comparative changes in HUB with time

B. Total Petroleum Hydrocarbon (TPH) Count Evaluation

The degree of biodegradation of petroleum hydrocarbon polluted soil was investigated using a blend of NPK fertilizer and Periwinkle Shell Ash as stimulants to stimulate the indigenous micro-organisms population. The Total Petroleum Hydrocarbon (TPH) content removal effect was used as the indicator parameter for the bioremediation and it was seen to reduce with time during the period of study. The result also shows that the effect of time was highly significant.

Figure 3 is a plot of comparatives changes in TPH of the polluted soil samples with Time. The results

shows a decrease in TPH concentration with Time during the period of the experiment for all cases. The TPH decreased from an initial value of 58,200 mg/kg at the commencement of the experiment to 48,007.55 mg/kg to 34,891 mg/kg on the 90th day of experimentation for the control experiment. This depletion of TPH in the soil shows that indigenous micro-organisms in the soil have the natural ability to degrade the petroleum hydrocarbon and use it as a carbon source and energy. This is in line with the findings of Rosenberg and Ron (1996). Rosenberg and Ron (1996) in their bioremediation study carried out shortly after the Exxon Valdez oil spill during the summer of 1989 in which they used Oleophillic fertilizer to remediate the crude oil polluted shorelines. A similar study carried out by Obiakalaije et. al., (2015), in which they used various animal wastes as amendment to treat crude oil polluted soil, also observed a reduction in TPH with time in the control sample. However, in this study it is shown that the stimulation of the crude oil polluted soil with NPK fertilizer, and/or Periwinkle Shell Ash enhanced the rate of TPH degradation.

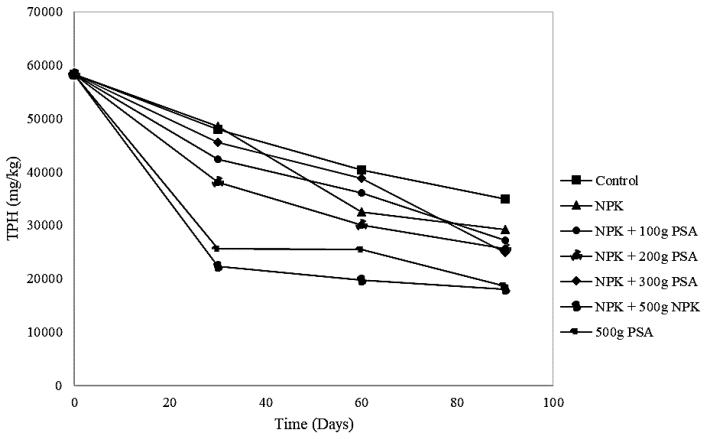

Figure 3: Plot of comparative changes in TPH with time

For TPH concentration against time for crude oil polluted soil with 100g of NPK fertilizer as stimulant. The result shows a significant reduction in TPH from the initial value of 58,200 mg/kg at the commencement of the experiment to 29,183 mg/kg after 90 days of the experiment.

Table 3: Results of TPH concentration during the Experimentation Process

	Sample \ Time	0 day	30 days	60 days	90 days
TPH values in mg/kg	Control	58,200	48,007.53	40,383.20	34,891
	100 g NPK	58,200	48,561.53	32,527.80	29,183
	100 g NPK + 100 g PSA	58,200	42,381.00	36,006.60	27,103
	100 g NPK + 200 g PSA	58,200	38,103.8	30,086.60	25,636
	100 g NPK + 300 g PSA	58,200	45,529.25	38,728.40	24.857
	100 g NPK + 500 g PSA	58,200	22,254.20	19,729.30	18,045
	500 g PSA	58,200	25,522	25,407.31	18,640
ln(TPH)	Control	10.972	10.78	10.61	10.46
	100 g NPK	10.972	10.79	10.39	10.28
	100 g NPK + 100 g PSA	10.972	10.65	10.49	10.21
	100 g NPK + 200 g PSA	10.972	10.55	10.31	10.15
	100 g NPK + 300 g PSA	10.972	10.73	10.56	10.12
	100 g NPK + 500 g PSA	10.972	10.01	9.89	9.8
	500 g PSA	10.972	10.15	10.14	9.83

This clearly shows the effect of the stimulation on the remediation process when compared to the control experiment. Gadhvi (2019) explained that nitrogen deficiency in crude oil polluted soil as a result of increase in organic carbon retards bacteria growth and hence a limiting factor. This position is also corroborated by Asuquo, Ibanga, and Idunafa (2001), where they observed that increase in organic carbon in petroleum hydrocarbon polluted soil creates an initial scarcity of nitrogen. The supply of nitrogen through the NPK fertilizer has now stimulated the bacteria growth and enhanced the ability of the nitrogen fixing bacteria and hence enhanced the biodegradation activity leading to the reduction in TPH, since nitrogen is a source of nutrient for micro-organisms (Ekenwosu, 2019).

For the case of TPH concentration against time for crude oil polluted soil with a blend of 100 g of NPK

fertilizer and 100 g of Periwinkle Shell Ash. From the results obtained, there was a further reduction of TPH from 58,000 mg/kg to 27,103 mg/kg during the same 90 days experimentation period, a value lower than the 29,183 mg/kg obtained when only 100 g of NPK fertilizer was used. This difference was believed to be the effect of the addition of the periwinkle shell ash used in combination with the NPK fertilizer. The additional nutrients supplement being supplied by the PSA like calcium, zinc, iron and phosphorus have microbially mineralized the stimulated soil and have contributed to the remediation. This is in agreement with the findings of researchers like Oyedele and Amoo (2014), and Gadhvi (2019).

When, only 500 g of PSA was used with no addition of NPK fertilizer, and the result shows a significant reduction of TPH to 18,640 mg/kg during the same period of study. This clearly agrees with the findings of Ofoegbu et. al., (2015).

V. CONCLUSION

A simple, very effective, cheap, readily available and environmentally friendly technology for bioremediation of crude oil polluted soil was employed in this research work (Periwinkle Shell Ash (PSA) and N.P.K fertilizer). The experiment was carried out under aerobic conditions using seven batch bioreactors in the laboratory. Indigenous micro-organisms were identified, cultured and used for the process. The result showed that for crude oil polluted soil amended with NPK, and NPK + PSA and the control sample, the THB increased from 6.0 × 105 cfu/g to 3.3 × 108 cfu/g, 3.95× 108 cfu/g and 3.02 × 108 cfu/g respectively after 60 days of the experimentation process.

In the same vein, HUB also increased from 2.74 × 104 cfu/g to 3.33 × 107 cfu/g, 4.45 × 107 cfu/g and 2.59 × 107 cfu/g for NPK, NPK + PSA and control respectively after 60 days of the experimentation process.

Total Petroleum Hydrocarbon (TPH) reduced from 58,200 mg/kg to 34,891 mg/kg for control sample, 29,183 mg/kg for sample amended with 100g NPK, 27,103 mg/kg for sample with 100g NPK + 100g PSA; 25,636 mg/kg for sample with 100g NPK + 200g PSA, 24,857 mg/kg for sample with 100g NPK + 300g PSA, 18,045 mg/kg for sample with 100g NPK + 500g PSA and 18,640 mg/kg for sample with 500g PSA respectively at the end of the 90 days experimentation period.

The soil PH decreased as a result of the pollution of the soil with crude oil, increased with the addition of the biostimulants, and hence improved the soil properties.

Finally, remediation of crude oil polluted soil with periwinkle shell ash and NPK fertilizer have proven to be effective in improving the physicochemical properties of the soil.

REFERENCES

Adesodu J. K. and Mbagwu J. S. C. (2008) Biodegradation of Waste Lubricating Petroleum Oil in a Tropical Soil as Mediated by Animal Droppings. *Bioresources Technol*, 99: 5659 – 5665.

Agarry, S. E. (2010) Bioremediation of Soil Artificially Contaminated with Petroleum Hydrocarbon Mixtures: Evaluation of the use of Animal Manure and Chemical Fertilizer. *Bioremediation J.*14 (4), 189-195.

Ahmadi, F., Assadi, Y., Milani-Hosseini, S. M. R. and Rezaee, M. (2006) Determination of organophosphorus pesticides in water samples by single drop microextraction and gas chromatography-flame photometric detector. Journal of Chromatography A, Volume 1101, Issues 1–2, pp 307-312.

Ajagbe, W. O., Omokehinde, O. S., Alade, G. A., and Agbede, O.A. (2012) Effect of Crude Oil Impacted Sand on Compressive Strength of Concrete. *Constr. Build. Mater*, 26, 9-12.

Akbari, A., and Ghoshal, S. (2014) Pilot-Scale Bioremediation of a Petroleum Hydrocarbon-Contaminated Clayey Soil from a Sub-Arctic Site. *J. Hazard Mater.* 280: 595 - 602.

Asuquo, F. E., Ibanga, I. J. and Idunafa, N. (2001) Effect of Qua-Iboe Crude Oil Contamination on Germination and Growth of Okro (Abelmoschusesculentus L.) and Fluted Pumpkin (Telfairia Occidentalis L.). *Proc. of the 27th Annual Conf. of the Soil Science of Nigeria, University of Calabar*: pp 5 – 9.

Atuanya, E. (1987) Effects of Waste Engine Oil Pollution on Physical and Chemical Properties of the Soil. *Nigerian Journal of Applied Science*, 55, 155-176.

Bento Fatima M., Flavio AO Camargo, Benedict C. Okeke and William T. Frankenberger (2005) Comparative Bioremediation of Soil Contaminated with Diesel oil by Natural Attenuation, Biostimulation and Bioaugmentation. *Bioresource technology,* 96 (9), 1049 – 1055.

Danjuma, B. Y., Abdulsalam, S. and Sulaiman, A. D. I (2012) Kinetic Investigation of Escravos Crude Oil Contaminated Soil Using Natural Stimulants of Plant Sources. *International Journal Emerging trends in Eng, and Development*, 2 (5) 478-486.

Department of Petroleum Resources (1997).

Ekenwosu J. U (2019) Bioremediation of Arable Soil Using Nitrogen, Phosphorus, Potassium Fertilizer Treatment. *Sustinere Journal of Environment and Sustainability*, Vol. 3, Issue 1, pp 15 – 23.

Gadhvi, S. N. (2019) Remediation of Petroleum Oil Contaminated Soil by Using Organic Fertilizer. *ACTA Scientific Agriculture*, 3 (10): pp 177 – 180.

Ijah, U. J. J. and Antai S. P (2003) The Potential Use of Chicken Droppings Micro-Organisms For Oil Spill Remediation. *The Environmentalist*, 23: 89 – 95.

Ivshina, I. B., Kuyukma, M. S., Krivoruchko, A. V., Elkin A. A., Markarov, S. O., Cunningham, C. J., Peshkur, T. A., Atlas, R. M., and Philip, J. C. (2015) Oil Spill Problems and Sustainable Response Strategies through New Technologies. *Environ. Sci. Process Impacts* 17, 1201-1219.

Jobson, A., McLaughlin, M., Cook, F. D. and Westlake D. W. S. (1974) Effects of Amendments on Microbial Utilization of Oil Applied to Soil. *Appl*. *Microbial*, 27: 166 – 171.

Kalyuzhnyi, S., Veeken, A. and Hamelers, B. (2000) Two-particles Model of Anaerobic Solid State Fermentation. *Water Science Technology,* 41 (3), 43 – 50.

Khamehchiyan, M., Kossein Charkhabi, A., and Ind Tajik, M. (2007) Effects of Crude Oil Contamination on Geotechnical Properties of Clayey and Sandy Soils. *Eng. Geol*., 89, 220-229.

Margesin, R. and Schinner, F. (1997) Efficiency of Endogenous and Inoculated Cold-Adapted Soil Microorganisms for Biodegradation of Diesel Oil in Alpine Soils. *Appl. Environ Microbiol*.

Margesin, R. Hammerle, M. and Tscherko, D. (2007) Microbial Activity and Community Composition during Bioremediation of Diesel-Oil Contaminated Soil; Effects of Hydrocarbon Concentration, Fertilizers and Incubation Time. *Microbail Ecol*., 53, 259 – 269.

Nakasaki, K., Yaguchi, H., Sasaki, Y. and Kubota H. (1992) Effect of C/N Ratio on Thermophillic Composting of Garbage. *Journal of Fermentation and Bioeng.*, 73: 43 – 45.

Nas (1975) National Academy of Science. Under – Exploited Tropical Plants with Promising Economic Value Washington DC, PP 37 – 44

Ndimele, P. E., Saba, A. O., Ojo, D. O., Ndimele, C. C., Anetekhai, M. A., and Erondu, E. S. (2018) Remediation of Crude Oil Spillage in the Political Ecology of Oil and Gas Activities in the Nigeria Aquatic Ecosystem. In Academic Press: London UK. pp 369-384.

Nicolotti, G., and Egli, S. (1998) Soil contamination by crude oil: impact on the mycorrhizosphere and on the revegetation potential of forest trees. *Environ Pollut*, 99(1):37-43. doi: 10.1016/s0269-7491(97)00179-6.

Nyankanga, R. O., Onwonga, R. N., Wekesa, F. S., and Nakimbugwe D. (2012) Effect of Inorganic and Organic Fertilizers on the Performance and Profitability Of Grain Amaranth (Amaranthus

caudatus L.) in Western Kenya. *Journal of Agricultural Science,* 4 (1), 223.

Obiakalaija, U. M, Makinde O. A, and Amakoromo E. R. (2015) Bioremediation of Crude Oil Polluted Soil Using Animal Waste. *International Journal of Environmental Bioremediation and Biodegradation*, Vol. 3, No. 3, pp. 79 – 85, doi:10.12691/jebb-3-3-2.

Odukoya Johnson, Lambert Ronnie and Sakrabarmi Ruben (2019) Understanding the Impacts of Crude Oil and its Induced Abiotic Stresses on Agrifood Production. A Review. *Horticultural*, 5, 47, pp1-27.

Ofoegbu, R. U., Momoh, Y. O. L. and Nwagozie I. L. (2015) Bioremediation of Crude Oil Contaminated Soil Using Organic and Inorganic Fertilizers. *Journal of Petroleum and Environmental Biotechnology*. Vol. 6, Issue 1, pp 1 – 6.

Ofunne, J. I. (1999) Bacteriology Examination of Clinical Specimens. Achugo Publications, Ama J. K, Recreation Park, Owerri, Nigeria pp. 24 – 35.

Osuagwu, A. N., Okigbo, A. U., Ekpo I. A., Chukwurah, P. N., and Agbor, R. N., (2013) Effect of Crude Oil Pollution on Growth Parameters, Chlorophyll Content and Bulbils Yield in Air Potato (Dioscorea Bulbifera L.,). *International Journal of Applied Science and Technology.* 3 (3) pp 37 – 42.

Osuji, L. and Adesiyan, S. O. (2005) The Isiokpo Oil-Pipeline Leakage: Total Organic Carbon/Organic Matter Contents of Affected Soils. *Chemistry and Biodiversity,* 2 (8): 1079 – 1085.

Oyedele, A. O. and Amoo, I. A. (2014) Remediation of Crude Oil Polluted Soil Using Cow Dung Manure in Relations to the Growth of Maize (zea mays L.). *Canadian Open Agricultural and Soil Science Journal*. Vol. 1, No 1, pp 1 – 16.

Rahman, K. (2002) Bioremediation of Gasoline Contaminated Soil by a Bacterial Consortium Amended with Poultry Litter, Coir Pith and Rhamnolipid Biosufactant. In K. S. Rahman, 'Bioremediation of Gasoline Contaminated Soil by a Bacteria Consortium Amended with Protein Littre, Coir Pith and Rhamnolipid Biosurfactant. *Bioresource Technology*, 81 (1) (pp. 23-32).

Richard, J. & Vogel, T. (1999) Characterization of a Soil Bacterial Consortium Capable of Degrading Diesel Fuel; *Int. Biodeterior. Biodegradation* 1999 (44, pp. 93-100).

Rosenberg, E. and Ron, E. Z. (1996) Bioremediation of Petroleum Contamination. In: Crawford R. L. and Crawford D. L. (eds.) Cambridge: Cambridge University Press. Bioremediation: Principles and Application, pp. 100 – 124.

Schmidt – Ethin (2011) Spill Occurences: A World Overview. In Oil Spill Science and Technology: Prevention, Response, and Clean Up, 1st ed.; Fungas M.Ed; Gulf Professional Publishing: Amsterdam, The Netherlands.

Seklemova, E. P. (2001) Biostimulation based Bioremediation of Diesel Fuel: Field Demonstration. Biodegradation 12 (pp. 311-316).

Sheldrick, B. H. and Wang, C. (1993) Particle Size Analysis. In: Carter, M. R., Ed., Soil Sampling and Methods of Analysis, Lewis Publishers, Boca Raton, 499 – 517.

Udo, E. J., and Fayemi, A. A. A., (1975) The Effect of Oil Pollution on Germination, Growth and Nutrient Uptake of Corn. *Journal of Environmental Quality*, 4, pp 537 – 340.

Ukpaka, C. P., and Okochi, G. I. (2018) Production of Cement from Mixture of Palm Kernel Periwinkle Shell. *Indian Journal of Engineering*, 15, 166 – 179.

Yelebe, Z. R., Samuel, R.J., and Yelebe, B. Z., (2015) Kinetic Model Development for Bioremediation of Petroleum Contamination Soil using Palm Bunch and Wood Ash. *Int. Journal of Engineering Science Invention*, Vol. 4, Issue 5, pp 40 – 47.

Journal of Engineering, Emerging Technologies and Applied Sciences -– Volume 1 Issue 2, Nov. 2023

Available at ***https://www.ndu.edu.ng/journalofengineering/***

RESEARCH ARTICLE OPEN ACCESS

Recycling of Waste Engine Oil using Acetic and Lactic Acids as Washing Agents

Orlando Ketebu, Ebiundu Komonibo, Emmanuel Marine Gbafade

(Department of Chemical Engineering, Niger Delta University, Wilberforce Island Bayelsa State

Email: ketebu.orlando@ndu.edu.ng)

----------**********----------

Abstract

Waste engine oil (WEO) is known to contain metal, carbon and oxidized contaminants which are harmful to human and the environment. This research refines WEO using acetic and lactic acids as washing agents. Parameters such as kinematic viscosity, flash point, pour point, specific gravity were analysed for oils. The result of the experiment showed that the kinematic viscosity of WEO (165.52 cSt) increased when washed with acetic (181.20 cSt) and lactic acids (179.96 cSt) at 40ºC similarly at 100ºC closer to fresh oil value (192.71 cSt). The decreased flash point of WEO (175 ºC) increased when treated with acetic (215 ºC) and lactic acids (212 ºC) compared to fresh oil (230 ºC). The increased pour point of WEO (-6 ºC) was reduced when treated with acetic (-11.5 ºC) and lactic acids (-10.9 ºC) which are close to fresh oil (-13 ºC). The high specific gravity of WEO (0.9186) were reduced by acetic (0.8756) and lactic acids (0.8745) closer to fresh oil (0.8815). These reduced parameters in the WEO and its increased pour point and specific gravity indicates impurities and contaminants in WEO. The improved values with acetic and lactic acids showed that they are good washing agents. FTIR analysis of WEO showed additional peaks at frequencies 1054.8, 1109.2 and 2310 cm^{-1} representing the primary oxidized products at high temperature which are absent in fresh oil and WEO treated with acetic and lactic acids.

Keywords — Recycling, Waste engine oil, Acetic and lactic acid, Acid/clay technique, Oil parameters, Fourier transform infrared spectroscopy (FTIR).

----------**********----------

I. INTRODUCTION

Engine oil (lubricating oil) is a complex hydrocarbon having large numbers of carbon atoms per molecule obtained through fractional distillation of crude oil. It is known for its application in the lubrication of engines, machines and automobiles (Ugwele et al., 2020). Engine oil prevents wear and tear in machine parts alongside removing contaminants from engine. It also acts cleaning agent, anti-corrosive and anti-cooling agent for machine parts. During usage, engine oil accumulates and absorbs impurities which affect its efficiency as lubricating, cooling and anti-corrosive oil. Impurities such as burnt carbon, sulfur, lead, oxidized hydrocarbons, barium, zinc, steel, copper, water, etc. have been reported to be present in used or waste engine oil and some of them are poisonous and harmful to human and the environment (Kwao-Boateng et al., 2020, Abro et al., 2013).

Waste engine oil (WEO) is contaminated used engine oil, cutting and servicing oil depending on the application that is to be disposed. WEO is a pollutant that affects our health, environment, plants and animals if not well disposed. In Nigeria, most WEO are poured directly on the ground or in water ways which in turn contaminates the water ways and soil affecting aquatic and plant growth and also exposing us to dangerous metal and oxidized pollutants (Sardasht et al., 2013).

This environmental and health concern about the disposing of WEO to the environment has brought

the need for recycling of WEO to its original base form for re-use and the removal of its impurities. Different techniques have been applied to recycle WEO such as vacuum distillation, which uses sulphuric acid to refine the WEO but also produces by-products with high sulphuric contents and also damages essential additives in the oil (Udonne et al., 2011). Acid-clay techniques, solvent extraction and membrane filtration techniques have also been used but they have their drawbacks such as being too expensive to operate, generation of more pollutants, wastage of solvent, damage of essential base oil additives and the inability to refine modern multi-grade oil (Anisuzzaman et al., 2021, Sardasht et al., 2013, Boadu et al., 2019).

Another way of refining WEO is through the use of inorganic acid. This involves the use of mostly concentrated sulphuric acid which is found to be effective but is known to produce toxic by-product which is harmful to the environment. This has made researchers to look at using organic acids as washers for recycling waste WEO. Different researchers have carried out recycling of WEO using organic acids and other acids such as acetic acid (Sardasht et al., 2013), acetic and formic acid (Saleh et al 2017), acetic, phosphoric, nitric and sulphuric acid (Stan et al. 2018). Their results showed improvement in the specific gravity, viscosity and flash point of the used oil compared to fresh oil when formic, sulphuric and phosphoric acids were used. Also a combination of acetic and formic acid improves the viscosity and colour of the used oil. But these non-organic acids (formic, sulphuric, phosphoric, nitric) affected other parameters such as removal of oil additives, kinematic viscosity, and pour point of the used oil and besides they are not environmentally friendly. Acetic acid on the other hand improved the used oil parameters close to the fresh oil with minimal distortion of the oil properties. This research work uses organic acids; acetic and lactic acid as refining agents in recycling WEO and compares the effectiveness of these organic acids in recycling WEO with one another.

II. MATERIALS AND METHOD

The following chemicals and equipment were used for to carry out the experiment.
($Al_2O_3.SiO_2.2H_2O$), Visco 2000 WEO and fresh oil (SAE 20W-50). Beaker, stirrer, electric heater, mass balance, measuring cylinder, centrifuge and magnetic stirrer.

A. Filtration and acid treatment of the waste engine oil

500 ml of the WEO was measured with a measuring cylinder and filtered with a filter paper to remove dirt's and colloidal particles. 150ml of the filtered WEO respectively was placed in two 250ml beakers respectively and heated at 250^oC for one hour to vapourize water and volatiles that might be present in the oil. The acids were added to the oils in the beakers at ratio 1:10 volume of acid to WEO. That is 15 ml of acetic acid (AC) was mixed with WEO in one of the beakers and 15 ml of lactic acid (LC) in the other beaker. The mixtures were left at room temperature and pressure for 24 hours. Supernatants in the acid treated oil (acidic base oil) were decanted into two 250ml beakers respectively. The acid sludge left in the beakers was discarded and the acidic base oil (ABO) in beakers were centrifuged at 3000 rpm for 30 minutes and decanted to remove impurities.

B. Bleaching and neutralization of the decanted base oil

The decanted ABO's were mixed with Kaolinite in the ratio of 1:25 by volume of Kaolinite to base oil. 4g Kaolinite was stirred in 100ml of base oil in beakers while heating the mixtures on hot plate at 110^0C for 15 minutes. This process changes the dark coloured base oils to red. Kaolinite addition to the oil removes the smell from the oil and changes the dark colour of the oil caused by oxidation of the oil during use.

The pH of the treated oils was neutralized with hydrated lime in the ratio 1:25 volume of lime to base oil. 4g of hydrated lime was mixed with 100 ml of the bleached oil with continues manual

stirring for 15 minutes. The mixtures were left to sediment for 24 hours and filtered with a filter paper.

C. Determination of oil parameters

The oil samples were taken to a laboratory in Port Harcourt where the flash point of the oils were analysed using an open cup flash point tester with ASTM D-92 guidelines. ASTM is American Standard for Material Testing. The pour points of the oils were measured using Ducom pour point tester machine following ASTM D5949 guidelines. The kinematic viscosities were measured using Brookfield DV-E viscometer and the specific gravity of the oils measured using oil density hydrometer.

III. RESULT AND DISCUSSION

Fig. 1 shows the WEO (A), fresh oil (B) and WEO treated with acetic (C) and lactic acid (D) respectively. From the figure it can be seen that WEO is dark in colour due to contaminants and usage. The fresh oil labelled B is clean with green brown colouration. The acetic and lactic treated WEO had similar colour compared to fresh oil but darker. This is due to the washing activities of acetic and lactic acid in recycling of WEO and removal of some oil additives in the process.

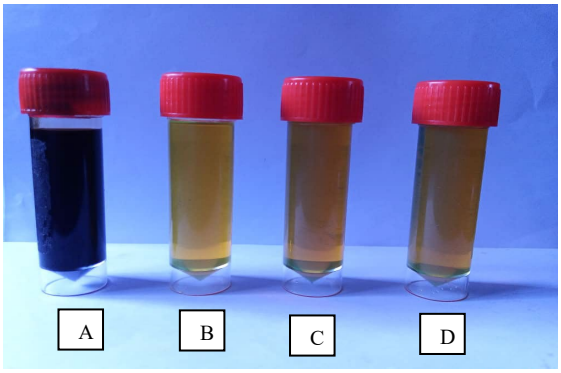

Fig. 1 WEO compared to fresh oil and acetic and lactic treated WEO.

Table 1 shows the measured properties of fresh oil, WEO and acid treated WEO. The table showed that the kinematic viscosity of WEO decreases by 27.19 centistoke (cSt) to 165.52 (cSt) at 40^0C compared to the fresh oil (192.71cSt). Also at 100^0C, the kinematic viscosity of WEO decreases by 4.15 to 14.20 cSt compared to the fresh oil (18.35 cSt). These decreases in viscosity indicate the presence of contaminants in the WEO. The kinematic viscosity is a measure of how oil flows when force is applied. Thus the higher the kinematic viscosity, the lesser the shear stress and oxidized products.

Table 1 Measured oil parameters

S/N	Samples	Kinematic viscosity (40^0C) (cSt)	Kinematic viscosity (100^0C) (cSt)	Specific gravity	Flash Point ^{0}C	Pour Point ^{0}C
1	Fresh oil (SAE 20W-50)	192.71	18.35	0.8815	230	-13
2	WEO	165.52	14.20	0.9186	175	-6
3	WEO + Lactic acid	179.96	15.77	0.8745	212	-10.9
4	WEO + Acetic acid	181.20	16.10	0.8756	215	-11.5

Table 1 also showed that acetic and lactic acids when added to WEO at 40^0C and100^0C, the kinematic viscosity were slightly affected by the acids. Acetic acid had 181.20 centistokes and lactic acids (179.96 cSt) at 40^0C compared to fresh oil (192.71 cSt). Also minimal difference in kinematic viscosity were observed at 100^0C with 16.10 cSt for acetic treated WEO and 15.77 cSt for lactic acid treated WEO compared to the fresh oil (18.35 cSt). This slight difference in the value of the kinematic viscosity treated with acetic and lactic acids showed that these two acids are less destructive to the mixtures and additives of the base oil while refining the WEO. This indicates that acetic and lactic acids are good washing agents in refining WEO.

The specific gravity of the WEO (0.9186) in Table 1 is higher compared to the fresh oil (0.8815) and WEO treated with acetic (0.8756) and lactic acids (0.8745). This is because the WEO contains contaminant such as metals, condensed and oxidized products rich in carbon which increases the specific gravity of the WEO. Specific gravity is known to increase in oil if there is an increase presence of aromatic compounds and solids in the oil and decreases when saturated compounds are present (Abu Elella et al. 2015). Also the specific gravity of WEO treated with acetic (0.8756) and lactic acid (0.8745) is lower than that of the fresh oil (0.8815) because of additives in the fresh oil to aid performance of the fresh oil. The low value of specific gravity of acetic (0.8756) and lactic acid (0.8745) showed that they are good washing agents for WEO in removing contaminants with acetic acid being less destructive to additives in the oil.

The flash points of the oils in Table 1 showed that the fresh oil had highest value of 230^0C due to additives in the oil to enhance performance. Flash point is the lowest temperature for an oil to ignite when heated under certain conditions. And it is used to determine the degree of contamination of oil. Decreasing flash point values of oils is known to be as a result of metallic contents, fuel and oxidation products in oil (Abu Elella et al. 2015). The flash point of WEO in table 1 is 175^0C compared to 230^0C for fresh oil. This shows that the WEO is contaminated. Washing the WEO with acetic and lactic acids increased the flash point of the WEO to 215^0C and 212^0C respectively. This showed that acetic and lactic acids are effective in removing contaminants in WEO and improving its flash point.

Table 1 also showed that treating the WEO with acetic and lactic acid improved the pour point of WEO from -6^0C to -11.5^0C for acetic and -10.9^0C lactic acid treated. The pour point values of -11.5^0C and -10.9^0C are close to the value recorded for fresh oil (-13^0C) with minimal differences of 1.5^0C and 2.1^0C for acetic acid treated and lactic acid treated WEO respectively. This shows that the treated WEO with acetic and lactic acid can enable engine starts at cold weather. This is because pour point is the lowest temperature for engine oil to remain in a flowing state. The pour point values of oils is affected by the viscosity of the oil, thus high viscosity oil have high pour point and contaminants in oil increases oil viscosity.

Fig. 2 shows the FTIR spectrum for the fresh oil. The spectrum shows oxidation of the oil at frequency 1748 cm^{-1} which might be due to the production quality of the oil. Spectral band 1700 to 1750 cm^{-1} indicates oxidation compounds is present in the oil and carbonyl compound (C=O) are easily absorbed in this frequencies. The spectrum also shows the presence of alkenes, aromatics, alkyl halides, alkanes and carbonyl compounds in the fresh oil and their corresponding frequencies explained in table 2.

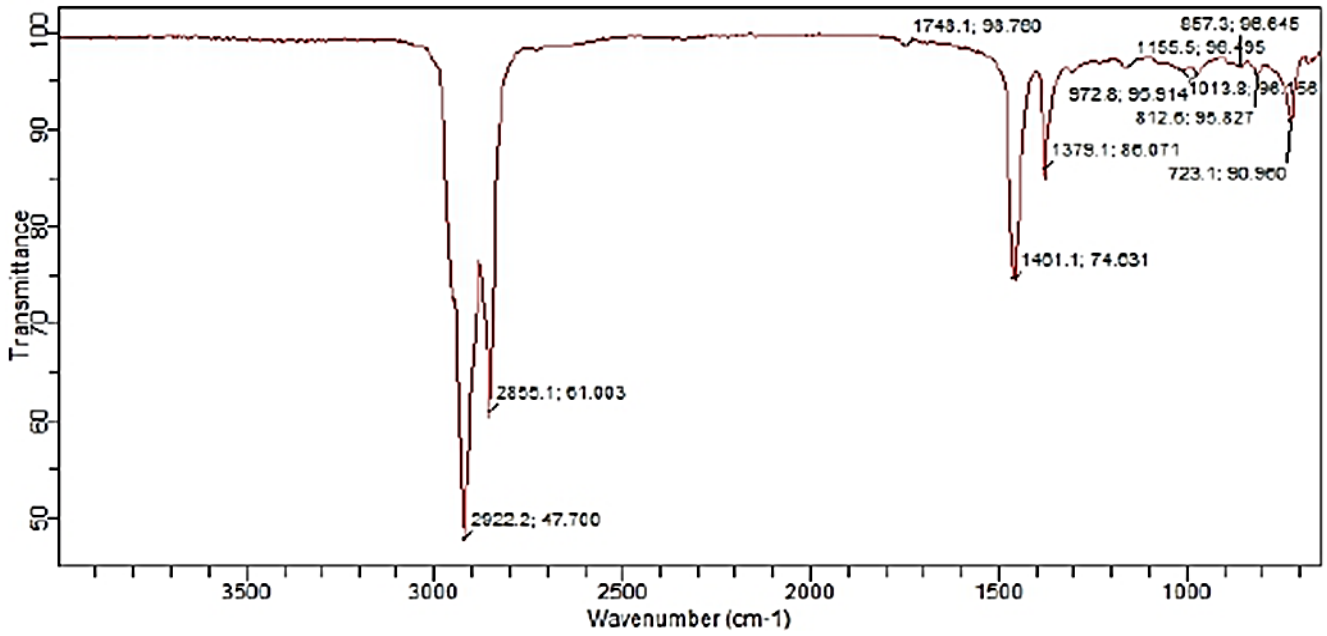

Fig. 2 FTIR spectra of fresh engine oil

Table 2 FTIR Analysis of fresh oil

Frequency cm-1	Bond	Functional Group
723.1	C – H	Alkenes
812.0	C – H	Alkenes
957.3	C – H	Aromatics
972.8	C – H	Aromatics
1155.5	$CH_2 - X$	Alkyl Halide
1379.1	C – H	Alkanes
1401.1	C – H	Alkanes
1748.1	C = H	Carbonyl compound
2855.1	C – H	Alkanes
2922.2	C – H	Alkanes

Fig. 3 shows the FTIR spectra for WEO showing additional peaks at frequencies 1054.8, 1109.2 and 2310 cm^{-1} representing the primary oxidized products at high temperature as analyzed in table 3. These are indications of the oil been used compared to the fresh oil.

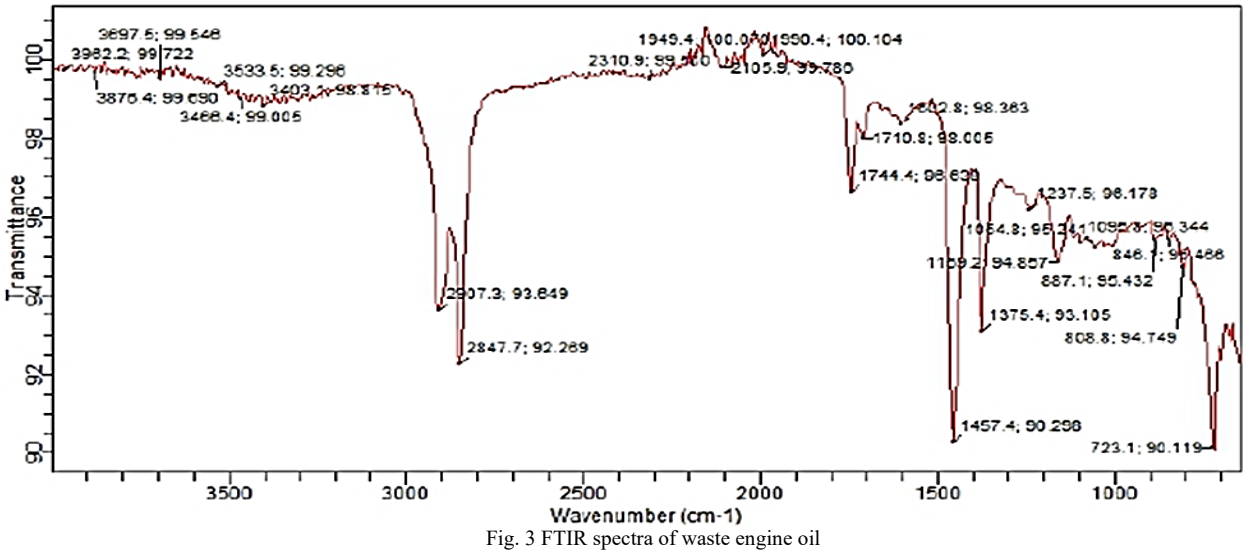

Fig. 3 FTIR spectra of waste engine oil

Table 3 FTIR Analysis of waste oil

Frequency cm-1	**Bond**	**Functional Group**
723.1	$C-H$	Alkenes
808.8	$C-H$	Alkenes
848.1	$C-H$	Alkenes
887.1	$C-H$	Alkenes
1054.8	$C-O$	Carboxylic acid
1109.2	$C-O$	Carboxylic acid
1237.6	CH_2-X	Alkyl Halide
1375.4	$C-H$	Alkanes
1457.4	$C-H$	Alkanes
1602.8	$C=H$	Aromatics
1710.8	$C=H$	Carbonyl compound
1744.4	$C=H$	Carbonyl compound
2310.9	$C-O$	Carboxylic acid
2847.7	$C-H$	Alkanes
2907.3	$C-H$	Alkanes

Fig. 4 and table 4 are the FTIR spectra for WEO with acetic acid and its analysis respectively. The result shows similarity with the fresh oil with the exception of an oxidized product at frequencies 1054.8 cm^{-1} and 1182.9 cm^{-1} which originates from the waste oil.

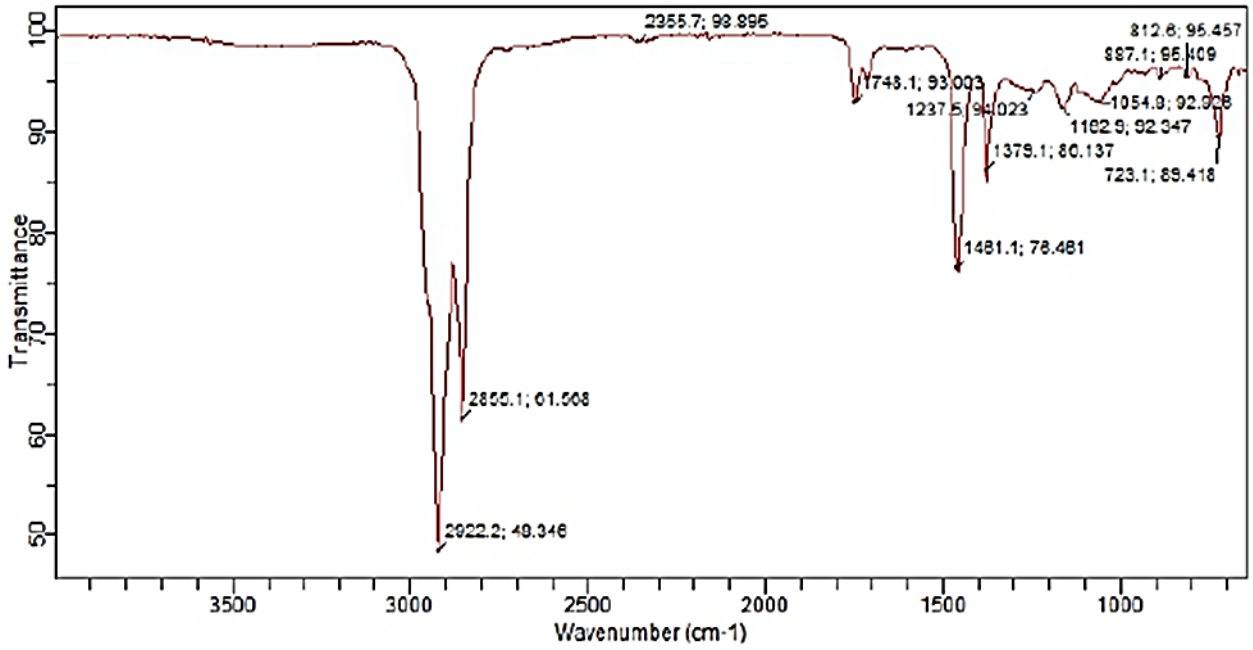

Fig. 4 FTIR spectra of WEO treated with acetic acid

`Table.4 FTIR Analysis of WEO treated with acetic acid

Frequency cm-1	Bond	Functional Group
723.1	C – H	Alkenes
812.6	C – H	Alkenes
1054.8	C – O	Carboxylic acid
1182.9	C – O	Carboxylic acid
1379.1	C – H	Alkyl Halide
1481.1	C – H	Alkanes
1748.1	C = H	Carbonyl compound
2855.1	C – H	Alkanes
2922.2	C – H	Alkanes

The FTIR spectra in Fig 5 for WEO treated with lactic acid and its analysis in table 5 showed similarities with the fresh oil. There were no oxidized products in the treated oil compared to that treated with acetic acid. This might be due to the ability of lactic acid to refine the WEO and remove the oxidized products

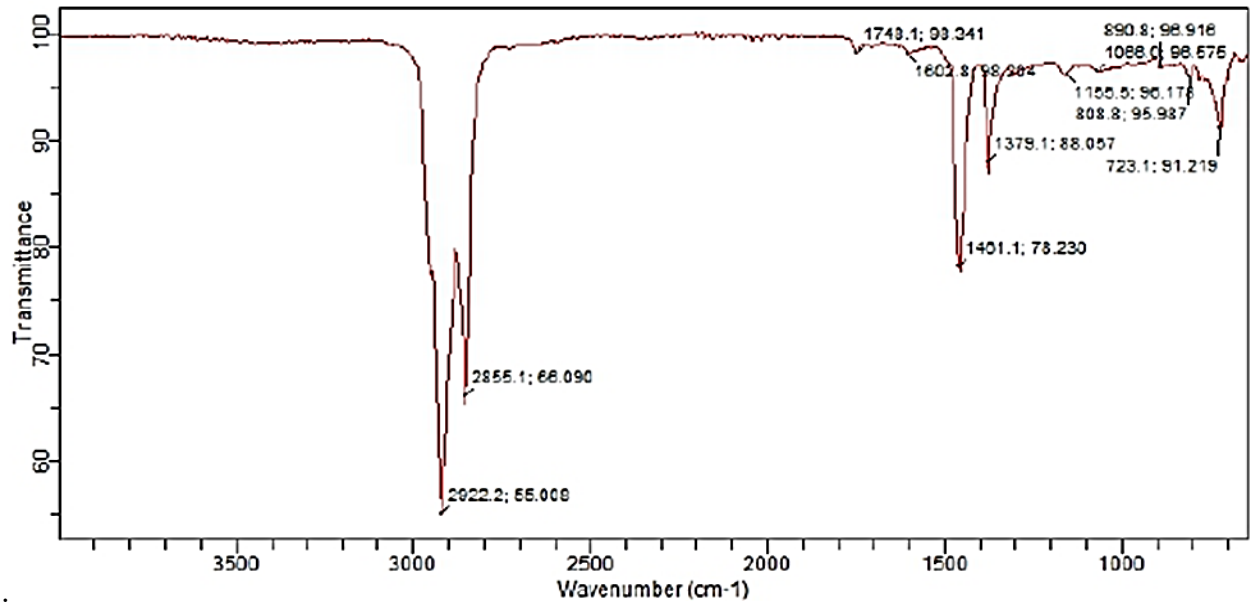

Fig. 5 FTIR analysis of WEO treated with lactic acid

Table 5 FTIR Analysis of Waste oil treated with lactic acid

Frequency cm-1	Bond	Functional Group
723.1	C – H	Alkenes
808.8	C – H	Alkenes
1155.5	$CH_2 - X$	Alkyl Halide
1379.1	C – H	Alkyl Halide
1401.1	C – H	Alkanes
1602.8	C = H	Aromatics
1748.1	C = H	Carbonyl compound
2855.1	C – H	Alkanes
2922.2	C – H	Alkanes

IV. CONCLUSION

In conclusion the FTIR analysis and oil parameters such as kinematic viscosity at 40°C and 100°C, flash and pour point, specific gravity, showed that acetic and lactic acids are good refining agents for WEO. The results for acetic and lactic acids are close to the fresh oil values with no oxidized products found in lactic acid treated WEO but acetic acid treated WEO results are closer to fresh oil values.

REFERENCES

Ugwele, F.O, Aninwede, C.S, , T.O, Christian, O.A, Innocent, S.I. (2020). Application of response surface methodology in optimizing the process conditions for the regeneration of used mobil oil using different kinds of acids. *Heliyon*. 6 (10), :e05062.

Kwao-Boateng, E., Terza, A. P., Anthony, N. P. A., Michael, K. F. (2022). "Re-refining Used Engine Oil in Ghana Using Solvent Extraction and Acid-Clay Treatment", *International Journal of Chemical Engineering*, 2022, Article ID 6344409, 8 pages,

Abro, R., Xiaochun ,C., Khanji , H., Zulifqar, A. D., Muhammad, "A. (2013). Comparative Study of Recycling of Used Engine Oil Using Extraction by Composite Solvent, Single Solvent, and Acid Treatment Methods", *International Scholarly Research Notices*, 2013, Article ID 952589, 5 pages.

Sardasht, T., Hamawand, I., Yusaf, T.F. (2013). Recycling of Waste Engine Oils Using a New Washing Agent, *Energies*., 6. 10.3390/en6021023.

Udonne, J. D. (2011). A comparative study of recycling of used lubrication oils using distillation, acid and activated charcoal with clay methods. *Journal of Petroleum and Gas Engineering,* 2(2), 12-19.

S Anisuzzaman, S .M., Jumaidi, M. H., Nasir , N. N .M. (2021). Used lubricating oil recovery process and treatment methods: A review *IOP Conference Series.: Material Science Engineering*. 1195 012031

Boadu, K. O., Joel, O. F., Essumang, D. K., Evbuomwan B. O. (2019). A Review of Methods for Removal of Contaminants in Used Lubricating Oil, *Chemical Science International Journal*, *26*(4): 1-11,

Salah, E.F., Hegazi, Y.A., Mohamd, M.I.H. (2017). Recycling of Waste Engine Oils Using Different Acids as Washing Agents, *International Journal of Oil, Gas and Coal Engineering*, *5*, (5), pp. 69-74.

Stan, C., Cristian, A., Marius, T. (2018). Some aspects of the regeneration of used motor oil, *Procedia Manufacturing, 22*, *709-713*

Abu-Elella, R., Ossman, M., Farouq, R., Abdel, F.M. (2015). Used Motor Oil Treatment: Turning Waste Oil Into Valuable Products, *International Journal of Chemical and Biochemical Sciences, 7*, 57-67.

Journal of Engineering, Emerging Technologies and Applied Sciences -– Volume 1 Issue 2, Nov. 2023

Available at ***https://www.ndu.edu.ng/journalofengineering/***

RESEARCH ARTICLE OPEN ACCESS

Niger Delta University Campus Borehole Water Quality Analysis for Domestic Purposes: Treated Versus Untreated Water

R. K. Douglas*, E. Komonibo*, A. W. Opukumo**

*Department of Chemical Engineering, Niger Delta University, Wilberforce Island, Amassoma, Bayelsa State, Nigeria.

Email: rewardkdouglas@gmail.com

**Department of Geology, Niger Delta University, Wilberforce Island, Amassoma, Bayelsa State, Nigeria.

----------**********----------

Abstract:

This study compared the quality of treated versus untreated water of the Niger Delta University campus borehole water for domestic purposes. Consequently, one untreated water, and 6 treated water samples were collected from source, and taps in 6 different hostels, respectively. Total heterotrophic bacteria (THB) count showed no THB for the treated samples, while 1.04 x 10^4/ml and 3.2 x 10^3/ml were Nutrient agar and MacConkey agar nutrient media, respectively for the untreated water.These values exceed the WHO maximum value (100/ml) for potable water. Similarly, themorphological characterization and biochemical tests revealed seven bacteria species in the untreated water sample, whereas none was identified in the treated samples.Results of the untreated water sample showed the presence of faecal coliform bacteria (FCB);while FCB was absent in the treated water samples.

The physiochemical parameters of the samples showed that the water is mildly acidic. The EC, TDS, turbidity, TSS, Cl^-, SO_4^{2-}, NO_3^-, HCO_3, TA, TH, Ca^{2+}, Mg^{2+}, Na^+, K^+, and Fe contents of the treated and untreated samples were below WHO permissible limits. Overall, results suggest treated water for domestic use. However, we recommend that water users should boil and disinfect water before use.

Keywords —Borehole water, Niger Delta University, faecal coliform bacteria, anions and cations.

----------**********----------

1.INTRODUCTION

Water is indispensable for living organisms, human health, food production, economic development and ecological systems. It is the most essential solvent for humamwelbeing (Livinus, 2014).There are various sources of water including rain water, surface water and ground water. Borehole water (BHW) is abstracted from ground water (GW); which is the best source of water for drinking, domestic, and irrigation purposes. Hence it is essential not only to know the groundwater contamination but also to examine and preserve the resource (Mayuri et al., 2018). However, GW quality is severely declining due to changes in the environment and increasing anthropogenic activities, resulting in a high impact on human health through intake of contaminated water. GW is contaminated with bacteria, viruses, heavy metals, nitrates, salts among others due to indiscriminate and improper disposal of wastes, unlawful waste management practices; which is more common in the cities due to high level of industrialization (Singh et al., 2011). Since one cannot do without water, there is high need for water in the society in all works of life. Thus, to service the water needs in any society, government and/or organization must provide potable water for her people and ensure its

quality. Consequently, the Niger Delta University has her own borehole that supplies water to the various student hostels and other quarters.

Environmental pollution and GW pollution can be related to human health, which are the most widespread problems in both the arid and semi-arid regions(Adimalla &Venkatayogi, 2018). According to (Penwick, 2006),2.5 billion people have no access to improved sanitation, and more than 1.5 million children die each year from diarrhea. World Health Organization (WHO, 2006) also reported that the mortality rate attributed to water associated diseases exceeds five million (5 million) people per year. From these records, more than 50% are microbial intestinal infections with cholera standing out as first. Also, GW pollution has been reported to have caused epidemic and chronic diseases in human beings.However,limited studies have shown a correlation between cardiovascular deaths and polluted water consumption (Olias et al., 2004; Pitt et al., 1995). Teeth and bones disorder was attributed to the consumption of fluoride-rich water (Susheela, 1999).

Freshwater is probably the most valuable of the natural resources. However, chronic GW contamination may reduce the availability of freshwater, breaking the balance between water supply and demand leading to socioeconomic crises and even wars. Water shortages induced by contamination may become a factor causing conflicts among citizens in the future (Schillinger et al., 2020), possibly delaying the socioeconomic development of a nation. In addition to contamination of GW, trace elements can be transported via GW into surface waters and into oceans. It is glaring that GWis a prime source of water for human wel-being, it can also be a pathway for disseminating diseases. Thus, efficient and cost-effective technologies for removal of trace elements from groundwater, and wholistic water quality measures are crucial for the sustainable management of water resources.

The physicochemical quality of GW in Yenagoa metropolis, Bayelsa State, including the Niger Delta University campus BHW was investigated (Okiongbo & Douglas, 2013). The authors concluded that the GW (not-treated) in the study area was unsuitable for drinking and irrigation due to high total hardness and total dissolved solids. In terms of iron contents, > 90% of the samples exceeded the permissible limit for drinking water and needs treatment. It is pertinent to mention that there is nodocumented research yet on the microbial quality of BHW in Bayelsa State. Thus, there is little or no study on the microbial quality of the NDU BHW till date. More importantly, discussions with students living in the various hostels revealed that bathing the NDU BHW without disinfection causes itching, and skin infections. Hence, there is urgent research need to examine the water quality parameters of the NDU BHW for the well-being of students and staff living on campus. Consequently, this study is focused on the microbial quality and physio-chemical parameters analysis of the NDU BHW.

2. MATERIALS AND METHOD

2.1 Study area and sampling

Niger Delta University is located in Amassoma, Southern Ijaw Local government area of Bayelsa State, Nigeria (Figure 1). A total of seen (6 treated and 1 untreated) water samples were collected using 50cl plastic bottles. Prior to sampling, the sample bottles were soaked in 1:1 dilute HCl overnight and properly washed with distilled water before used for sample collection. Furthermore, sample bottles were rinsed 2–3 times with the sample water. Taps were opened, and allowed to run for 4-5 minutes before sampling to attain steady conditions. Sixtreated water samples were collected from six different hostels on campus, and onenot-treated water sample was collected from the water works (source) on campus. The temperature, pH, and electrical conductivity (EC) of each sample was measured by hand-held digital meters before samples were labelled appropriately and sent to the Central Research laboratory of the Niger Delta University for analysis.

All apparatus used for testing were properly sterilized before and after use to avoid cross contamination. Samples were analyzed for physio-chemical parameters (pH, electrical conductivity-EC, turbidity, temperature, total dissolved solids-TDS, iron-Fe, total alkalinity-TA, total hardness-TH, nitrates-NO_3, sulphate-SO_4, bicarbonate-HCO_3, chloride-Cl, calcium-Ca^{2+}, sodium-Na^{+}, potassium-K^{+}, and magnesium-Mg^{2+}); and microbiological parameters including *Baciliusspp, Enter bacteraerogene spp, pseudomas spp, micococcus spp, Citrobacter spp, streptococcus spp and protons spp.*

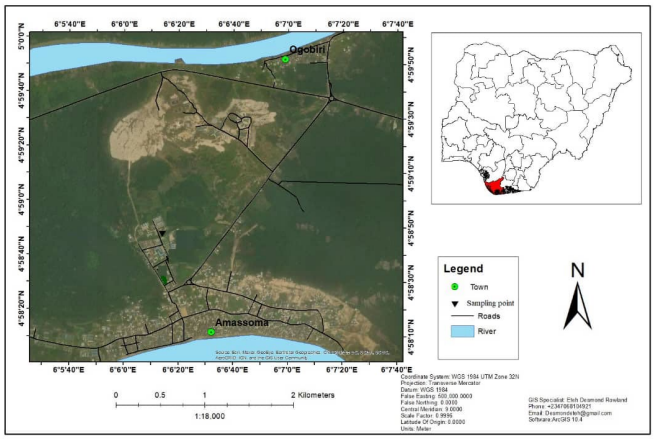

Figure 1: Water Sampling location-Niger Delta University. All the water samples were collected from the sampling location indicated in the map.

Microbiological Parameter Analysis: For quality assurance/quality control, all apparatus and/or equipment used for testing were properly sterilized before and after use. The microbiological parameters: *Bacillus spp, Enterobacteraerogenespp, Pseudomonas spp, Micrococcus spp, Citrobacterspp, Streptococcus spp and Protons spp* were analyzed usingsterilized bottles filled up allowing a small air space to allow for shaking.

Sterilization: Sterilization and disinfection were carried out to ensure that the apparatus used do not transmit microbial organism. The glassware, petri-dishes, nutrient media and reagents were sterilized by moist heat sterilization method using the autoclave. The instrument to be sterilized were first wrapped with aluminum foil. Then, the materials were arranged to ensure uninterrupted flow ofsaturated steam. The material was sterilized at 121^0C for 15 minutes to effect sterility. Sterilant liquid (alcohol at 70%) concentration was used to disinfect materials not suitable for moist heat sterilization. The bench was swab with alcohol before and after work.

Preparation of Nutrient Media: Nutrient Agar is a general medium use for the enumeration of heterotrophic colonies count. 28g was dissolved in 1000ml of distilled water in a borosilicate glass bottle. MacConkey agar is a differential medium use to distinguish Lactose-fermenting from the non-fermenting bacteria. 51.53g MacConkey agar was suspended in demineralize water. Salmonella Shigella Agar is a selective medium use for the identification of salmonella and shigella bacterial. 63grams of the powder was dissolved in 1000ml of distilled water. Kliger iron agar, simmon citrate, and peptone water were also included. The media was heated to dissolve completely in a water bath and sterilized by autoclaving for 15 minutes at 121ºC, in accordance with the manufacturer instruction.

The formulation of SIM media is designed to allow the detection of sulfide production, indole formation and motility. 30 grams of the medium was suspended in 1000 ml of distilled water, then heated to boiling with agitation to completely dissolve; and dispense into tubes and sterilized by autoclaving at 121°C for 15 minutes. MacConkey broth was prepared by dissolving 40g in 1 liter of distilled water, distributed into containers fitted with fermentation (Durham) tubes and sterilized by autoclaving at 121°C for 15 minutes

Calculation:

Based on the manufacturer's instruction for the use of nutrient agar, 28.g of nutrient agar was dissolved in 1000ml of water.

Bacteriological analysis: 1ml of the sample was also collected from the dilution factor of 1:100 and distributed into sterile broth contain in the Biju bottle with inverted Durham tube free of bubble. It was inoculated with the respective sample aseptically. The inoculated broths were incubated at 37°C for 24 hours with loosely capped. This was done to ensure the most probable number (MPN) of micro-organism.

$$\text{Coliform forming unit (CFU)} = \text{Degree of dilution} \times \text{aliquot} \times \text{No of colonies} \quad (1)$$

The colonies were randomly selected from the mixed culture using a sterile wire loop. The pick colonies were sub-cultured on a fresh nutrient agar plate by streaking method. The sub-cultured plate was inverted and incubated at 37° C to obtain a pure culture. The pure isolate was used for Gram staining and series of biochemical test in line with standard operational procedure.

Interpretation of Microbial Growth: Petri-dishes containing 30-300 colonies on nutrient agar plate, MacConkey agar and salmonella shigella agar were counted using the colony counter and multiply by the reciprocal of the appropriate dilution factor to obtain the viable count and expressed in CFU/g/cm^2.

The most probable techniques were examined for 24 to 48 hours. The bottle which had produced both acid and gas were counted. Acid production changes the colour of MacConkey Broth from purple to yellow and gas production by the collection of bubble in the Durham tube.

Characterization and Identification of Bacteria

Gram Staining: Gram staining of the various bacteria isolated were performed using the method introduced by Danish Bacteriologist Hans Christian Gram (1884). The microscopic glass slide was clean by washing with water and then wipe with alcohol and dry for use. The slide was labelled. Bacteria isolate were smear on the slide using sterilized wire loop and fixed by heating. Crystal violet staining reagent was poured and allow for 60 second and washed off with water. Lugol iodine solution was poured and allowed for 60 second and washed off with water. 95% of ethanol was poured to decolorize the dyes and allowed for 10 second, then it was washed off with water. Safranin was poured, allowed for 60 second and was washed off with water. This was allowed to air dry. The stained smear was observed using oil immersion under a light microscope.

Biochemical Test: The Biochemical test used in identification of the bacteria isolate are: Oxidase, catalase test, citrate test, indole test, motility and use of Klingler iron agar test involving "gas, H_2S, glucose and lactose.

Oxidase: A piece of filter paper was placed in sterile petri dish and 3 drops of freshly prepared oxidase reagent was added. A plastic loop was used to pick a small portion of the test organism which was rubbed on the soaked filter paper and observed for 10 minutes. Purple coloration on the smeared portion indicates positive result for oxidase test while no change in color on smeared portion indicates negative oxidase test.

Catalase Test: This test was performed in test tubes, 3ml of hydrogen peroxide was introduced into sterile test tubes using a sterile glass rod, colony of the pure culture was picked and dipped into the test tube and observed for the production of gas bubbles.

Citrate Test: Test organisms were streaked into sterile Simon's citrate agar pour in the test tube and incubated at 30°C for 24 hours. Growth with blue coloration indicate positive result while dark green coloration indicated negative result.

Motility and Hydrogen Sulfide Test: Using isolated colonies from an 18-24hour culture on solid media, inoculate in the SIM media by stabbing the center of the test tube containing 9ml medium to

a depth of 1/2 inch. Incubate the inoculated medium aerobically at 35ºC for 18-24hours. Observe for H_2S production and motility. Positive H_2S test is denoted by a blackening of the medium along the line of inoculation. A negative H_2S test is denoted by the absence of blackening. While positive motility test is indicated by a diffuse zone of growth flaring from the line of inoculation, negative motility test is indicated by growth confined.

Indole Test: This test was performed by culturing the isolate in peptone water containing tryptophan and incubated for 48 hours at 37ºC. Indole production was detected by adding 2-3 drops of Kovac's reagent to the 48 hours culture broth. Red ringed coloration indicated a positive result.

Sugar Fermentation Test: Klingler iron agar was prepared and 9ml of molten media were slanted and allow to be solidified. The isolate was stabbed and streaked on the slanted molten. It was placed in the incubator for 24 hours. Glucose fermentation indicated yellow coloration at the bottom giving a positive result. Lactose formation indicated yellow coloration at the slanted area giving a positive result while red indicated negative result.

Hydrogen Sulphide and Gas Production: The Klingler iron agar medium were prepared in a slanted test tube and organism were inoculated by streaking and stabbing and then incubated for 24-48 hours. Hydrogen sulphate production was indicated by black Mucor coloration on the surface of the slant while gas was indicated by cracking of the agar.

The material was sterilized at 121ºC for 15 minutes to affect sterility. Sterilant liquid such as alcohol at 70% concentration were used to disinfect materials not suitable for moist heat sterilization. The bench was swab with alcohol before and after work.

3. RESULTS AND DISCUSSION

3.1 Microbial analysis

Table 1 shows the analysis of the THB counts of the water samples analysed. Results indicate the presence of total heterotrophic bacteria in the not-treated water sample,while no THB was found in the treated water samples. The probability table for estimating the most probable number (MPN) of faecal coliform bacteria in the water samples are displayed in Table 2. Similarly, results confirm that the treated water samples analysed contain no faecal coliform bacteria, except the untreated samples. Furthermore, morphological characterization and biochemical tests revealed seven (7) isolates: *Proteus mirabilis; Micrococcus letues; Esichiaher coli; Enterococcus faecali; Staphylococcus aureus; Bacillus subtilis; and Streptococcus pyogene bacteria species* in the not-treated water sample, whereas none was identified in the treated samples. The results are presented inTable 3. Their presence indicates fecal contamination which might be due to the introduction of microbial contaminants into the borehole from the soakaway. The soakaway is about 15m away from the borehole, however, there is the posibiliy that microbes from the soakaway can infiltrate the borehole if the flow direction of soakaway is against the borehole location. Currently, there is no study on microbial quality analysis in borehole water in Bayelsa state to compare against the results of this study. However, (Onuoha et al., 2019) investigated the bacteriological quality of borehole water in Anambra state, Southern Nigeria and discovered the presence of total bacteria, total coliform, feacal coliform and vibrio choleraein borehole water.The authors recommended sand filtration, chlorination and boiling before drinking as treatment measures to avert a public health hazard.

3.2 Physio-chemical parameter analysis

The analysed results of the physio-chemical properties of water samples of the current study: treated and not-treated are presented in Table 4.The electrical conductivity (EC), turbidity, total dissolved solids (TDS), total suspended solids (TSS), Cl^-, SO_4^{2-}, NO^-_3, HCO_3, TA, TH, Ca^{2+}, Mg^{2+},

Na^+, K^+, and Fe levels of all the samples are all below WHO permissible limits. The physio-chemical parameters of same sample (not-treated) were analysed in 2013; and recommended for treated (Okiongbo& Douglas, 2013). As such, the results of the current study (treated and not-treated) were compared against those (Okiongbo& Douglas, 2013) and included in Table 4. The results current study were far better than those reported by(Okiongbo& Douglas, 2013), except the TA value. A plot of the not-treated 2013 data against the not-treated 2021 data was further generated in Figure 2; which clarifies the discrepancies that existed between the two data sets. The results could be attributed to better treatment and/or probably improved quality assurance and quality control measures put in place by the management over the years. However, the pH, TA and Ca^{2+} results deviated from the expected. That is, while the TA for the treated and not treated are same (i.e., 18), the pH, and Ca^{2+} of the treated were higher than those of not treated. Themean values of the physio-chemical properties of watersamples of the current study are presented in Table 5. Results were compared with WHO Standard, 2006. The results are all below WHO acceptable limits for drinking water. However, the treatment rather increased the concentrations of the pH, NO^-_3, and HCO_3; while the value for Fe was constant (i.e; 0.03). This may be attributed to the targeted treatment.

Table 1: Heterotrophic and enumeration bacteria count on nutrient media. **CFU**= coliform forming unit.

S/ID	**Media**	**No. of colonies plate count**	**Mean CFU/ml**
A^+	Nutrient agar	99 108 105	104 1.04×10^4
	MacConkey agar	32 34 30	32 3.2×10^3
	Salmonella shigella agar	** ** **	** **
A	Nutrient agar	** ** **	** **
	MacConkey agar	** ** **	** **
	Salmonella shigella agar	** ** **	** **
B	Nutrient agar	** ** **	** **
	MacConkey agar	** ** **	** **
	Salmonella shigella agar	** ** **	** **
C	Nutrient agar	** ** **	** **
	MacConkey agar	** ** **	** **
	Salmonella shigella agar	** ** **	** **
D	Nutrient agar	** ** **	** **
	MacConkey agar	** ** **	** **
	Salmonella shigella agar	** ** **	** **
E	Nutrient agar	** ** **	** **
	MacConkey agar	** ** **	** **
	Salmonella shigella agar	** ** **	** **
F	Nutrient agar	** ** **	** **
	MacConkey agar	** ** **	** **
	Salmonella agar	** ** **	** **

where **= absence of microorganisms; **A^+** = not-treated; **A-F** = treated; **S/ID** = sample identification

Table 2: Probability table for estimating the most probable number (MPN) of faecal coliform bacteria in the water samples

Volume of sample in each bottle	**50ml**	**10ml**	**1ml**	
Number of bottles used	**1**	**5**	**5**	**MPN/100ml**
RAW WATER SOURCE	1	3	3	18
TREATED WATER **A**	0	0	0	0
TREATED WATER **B**	0	0	0	0
TREATED WATER **C**	0	0	0	0
TREATED WATER **D**	0	0	0	0
TREATED WATER **E**	0	0	0	0
TREATED WATER **F**	0	0	0	0

Table 3: Results ofcharacterisation and identification of isolates from treated and raw borehole water samples.

Isolates	Morphology	GS	CAT	CI	IND	MOT	OX	GL	LAC	H_2S	Gas	Bacteria species
1	Rod	-	+	+	+	+	-	+	-	+	-	Proteus mirabilis
2	Coccus	+	+	+	-	-	+	-	-	-	-	Micrococcus letues
3	Rod	-	-	-	+	+	-	+	+	+	-	Esichiaher coli
4	Coccus	+	+	+	-	-	-	+	+	-	-	Enterococcus faecali
5	Coccus	+	-	-	-	-	-	+	+	-	-	Staphylococcus aureus
6	Rod	+	+	+	-	+	-	+	-	-	-	Bacillus subtilis
7	Coccus	+	-	-	-	-	-	+	+	-	-	Streptococcus pyogene

+ = indicates presence of bacteria;- = indicates absence of bacteria; **GS** = gram staining; **CAT** = catalase; **CI** = citrate; **IND** = indole, **MOT** = motility; **OX** = oxidase; **GL** = glucose; and **LAC** = lactose

Table 4: Results of current study compared with a previous study in 2013. Both studies sampled from same borehole.

a& b = current study;**c**= not treated;**na** = not analysed.

Properties	Untreated water[a]	Treated water (average)[b]	[11] [C]
pH	6.7	6.38	6.18
EC	49.4	60.30	495
Turbidity	0.01	0.34	NR
TDS	24.7	30.15	248
NO^-_3	0.13	0.12	1.6
Cl^-	7	10.00	14.2
SO_4^{2-}	0.51	0.65	4.7
HCO_3	1.2	0.40	36
TA	21	18.00	18
TH	10	29.00	42
Ca^{2+}	4.85	5.64	3.5
Mg^{2+}	1.18	1.43	1.8
Na^+	2.36	2.82	13.8
K^+	0.56	0.72	6.5
Fe	0.03	0.03	0.86

Table 5: Mean values of the physio-chemical properties water samples compared with WHO Standard, 2006.

Properties	Water: B-E (treated)	Water: A (untreated)	WHO (2006)max. permissible limit
pH	6.26	6.38	6.5-8.5
EC	45.40	60.30	1400
Turbidity	0.54	0.34	5
TDS	22.70	30.15	1000
NO^-_3	0.13	0.12	50
Cl^-	9.00	10.00	250
SO_4^{2-}	0.45	0.65	400
HCO_3	0.50	0.40	40
TA	16.00	18.00	500
TH	7.00	29.00	500
Ca^{2+}	5.04	5.64	75
Mg^{2+}	1.28	1.43	50
Na^+	2.54	2.82	200
K^+	0.67	0.72	55
Fe	0.04	0.03	0.3

TDS = Total Dissolved Solids; **TSS** = Total Suspended Solids; **TA** = Total Alkalinity; **TH** = Total Hardness; **EC** = electrical conductivity. All parameters have been expressed as mg/L, except pH and EC. The unit of EC is µS/cm while that of TA and TH is mg/L$CaCO_3$.

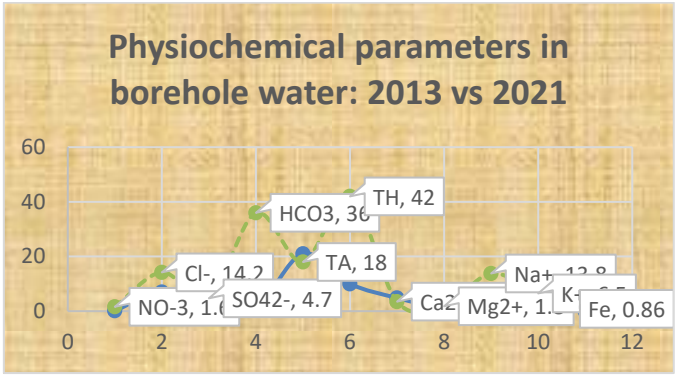

Figure 2: A plot of physio-chemical parameters of NDU campus borehole water for 2013 and 2021. Dashed curve represents 2013 parameters, while undashed represents 2021 parameters.

4. CONCLUSION

This study investigated and compared the quality of treated versus untreated water of the Niger Delta University campus borehole water for domestic consumption. Consequently, one raw water sample (source) and six (n = 6) treated water samples from 6 different student hostels were collected and analysed for both microbial quality and physio-chemical parameters. While there was no total heterotrophic bacteria (THB) for the treated water samples, the THB for the raw water sample for Nutrient agar and MacConkey agar nutrient media were 1.04 x 10^4/ml and 3.2 x 10^3/ml, respectively. Analysis on the faecal coliform count (FCC) showed the presence of faecal coliform bacteria (FCB) in the untreated water sample; whereas, no FCB was found in the treated water samples. Results of characterisation and identification of isolates from untreated water samples also revealed the presence of *Proteus mirabilis; Micrococcus letues; Esichiaher coli; Enterococcus faecali; Staphylococcus aureus; Bacillus subtilis; and Streptococcus pyogene bacteria species*. None of these isolates was identified in the treated water samples. The absence of the FCB, and the isolates in the treated water samples could be attributed to the effectiveness of the treatment measures by managers.

The physio-chemical parameter analysis of the water samples showed that the average value of pH

were 6.26 and 6.38 for the treated samples (n = 6), and the raw water, respectively. These values are within the WHO permissible limits for drinking water. The results of electrical conductivity, turbidity, total dissolvedsolids, total suspended solids, Cl^-, SO^{2-}_4, NO^-_3, HCO_3, TA, TH, Ca^{2+}, Mg^{2+}, Na^+, K^+, and Fe levels of all the samples were all below WHOacceptable limits. Overall, results of both the microbial and physio-chemical analysis suggest that the treated water is good for domestic consumption. However, the following recommendations are made: (a) the water should be boiled and disinfected before use since students reported that bathing the water without disinfection causesitching, and skin infections; (b) more research should investigate the causes of itching and skin infections as mentioned in (a) above; and (c) NDU borehole water managers should guide against rupture of water distribution pipe networks, as this may attract infiltration of dirts and microbes that may further contaminate the water.

ACKNOWLEDGMENT

The Niger Delta University Central Laboratory Team is acknowledged.

REFERENCES

Adimalla, N., &Venkatayogi, S. (2018). Geochemical characterization and evaluation of groundwater suitability for domestic and agricultural utility in semi-arid region of Basara, Talangana State, South India, *Appl Water Sci*. 8:44 doi:10.1007/s13201-018-0682-1.

Fenwick,A. (2006). Waterborne Diseases-Could They Be Consigned To History? *Science 2006,313,1077-1081*

Livinus, M. U. (2014). Physicochemical Analysis of Tap Water Obtained at Mass Water Works, GudiAkwanga, Nasarawa State, Int'l J. Chemical and Biological Sciences; *Vol.1(10): pp 10-13.*

Mayuri, P., Namrata, J., &Prasit A. (2018). Evaluation of groundwater quality with special emphasis on fluoride contamination using multivariate statistical analysis in rural parts of Surat district, Gujarat, ISH Journal of Hydraulic Engineering, DOI: 10.1080/09715010.2018.1468828.

Olias, M., Nieto, J.M., Sarmieto, A.M., Ceron, J.C., &Canovas, C.R. (2004). Seasonal water quality variations in a River affected by acid mine drainage, the Odiel River, South West Spain, *Science of the Total Environment*. 33, 267-281.

Okiongbo, K. S., &Douglas ,R. (2013). Hydrogeochemical Analysis and Evaluation of Groundwater Quality in Yenegoa City and Environs, Southern Nigeria, *Ife Journal of Science Is:209-222*

Onuoha, S., Igwemadu, N., &Odibe, F.(2019). Bacteriological Quality Assessment of Borehole Water in Ogbaru Community Anambra State Nigeria, *Universal Journal of Clinical Medicine 7(1):1-10*

Pitt, R., Lalor, M., & Brown, M. (1995). Urban stormwater toxic pollutants: Assessment, sources and treatability, *Water Environment Research*, 67, 260-275.

Schillinger, J., Ozerol, G., Guvwn-Griment, S., &Heldeweg, M. (2020). Water in War: Understanding the Impacts of Armed Conflict on Water Resources and Their Management,*WIREs Water 7: e1480*

Singh, K., Bharati, V., & Kumar, S. (2011). Physicochemical And Bacteriological Investigation Of Tuikhur Water, Sariha Town, Mizoram, India,*Screen viaion, vol.11, Issue1. pp 27-30.*

Susheela, A. K. (1999). Fluorosis management programme in India, Current Science 77, 1250-1256.

World Health Organization (2006). World Health Organization Guidelines for Drinking Water Quality. *3rd Edn. vol. 1 World Health Organization of the United Nations, Rome Italy.*

Journal of Engineering, Emerging Technologies and Applied Sciences -– Volume 1 Issue 2, Nov. 2023

Available at ***https://www.ndu.edu.ng/journalofengineering/***

RESEARCH ARTICLE OPEN ACCESS

Reducing Pipeline Corrosion in Oil and Gas Industries Using Ant Colony Optimization Techniques Agents

Easter Odonkumo Ikpaikpai, James Eke

Department of Electrical/Electronic Engineering, Enugu State University of Science and Technology (ESUT), Enugu

Email: odonseaster@gmail.com

----------**********----------

Abstract:

This paper aims at developing a model for the reduction in oil pipeline corrosion in oil and gas industries using ant colony optimization techniques. The main objective of the study is to examine the reduction of pipeline corrosion in oil and gas industries using ant colony optimization techniques. The specific objectives are; to develop mathematical model to reduce the oil pipeline rupture risks and oil spill probability; to design a MATLAB Simulink model for reducing oil and gas pipeline corrosion using ant-colony optimization. In this paper ant-colony based models were developed to assess API X46, X60 and X80 oil pipelines containing multiple corrosion defects, which were longitudinally aligned, circumferentially aligned or overcome with each other. The defect size and the grade of oil pipeline were considered to evaluate the interaction between adjacent defects. Ant-colony models enabling predictions of the failure pressure of pipelines containing a dent associated with a corrosion defect were also developed. In addition, a failure pressure-based criterion to properly assess the interaction of the dent and its adjacent corrosion feature was established. The mutual interaction between the adjacent corrosion defects affects not only the local stress and distribution, but also the electrochemical corrosion rate, due to the so-called Mechano-Electrochemical (M-E) effect. Due to the existence of the M-E effect, a new criterion is proposed to determine whether the mutual interaction exists between the adjacent corrosion defects, i.e., on the ratio of the anodic current density at the defect adjacency to that of the non-corrosion region on the oil pipeline body.

Keywords — **Corrosion, Ant-Colony Optimization, Pipeline, Matlab/Simulink, Defects**

----------**********----------

I. INTRODUCTION

Major pipelines across the world transport large quantities of crude oil, natural gas, and petroleum products (Husseini, 2018). These pipelines play an important role in modern societies and are crucial in providing needed fuels for sustaining vital functions such as power generation, heating supply, and transportation. In light of the hazardous properties of the products being transmitted through these pipelines, a ruptured pipeline has the potential to do serious environmental damage (Achebe et al., 2012). This problem is further compounded by the fact that many developing countries have not established proper guidelines and standards for the design, construction, and operation of major oil pipelines. This study concerns the analysis of oil pipeline corrosion in Nigeria with the aim to undertake a desk study to evaluate the procedures for pipeline maintenance and contingency plans for addressing oil pipeline failures in Nigeria using ant-colony optimization techniques. The risk associated with pipeline in terms of safety of people, damage to the environment and loss of income has been a major concern to pipeline integrity managers. The first ant colony optimization (ACO) called ant system was inspired through studying of the behaviour of ants in 1999 (Sallim et al., 2006). An ant colony is highly

organized, in which one interacting with others through pheromone in perfect harmony. Optimization problems can be solved through, simulating ant's behaviours. Since the first ant system algorithm was proposed, there is a lot of development in ant colony optimization. In ant colony system algorithm, local pheromone is used for ants to search optimum result. However, high magnitude of computing is its deficiency and sometimes it is inefficient. Stutzle and Hoos (2000) introduced MAX-MIN Ant System (MMAS) in 2000. It is one of the best algorithms of ant colony optimization. It limits total pheromone in every trip or sub-union to avoid local convergence. However, the limitation of pheromone slows down convergence rate in MMAS.

In optimization algorithm, it is well known that when local optimum solution is searched out or ants arrive at stagnating state, algorithm may be no longer searching the global best optimum value (Wu et al., 2023). In their algorithms, when ants arrived at local optimum solution, pheromone will be decreased in order to make algorithm escaping from the local optimum solution. When ants arrived at local optimum solution, or at stagnating state, it would not converge at the global best optimum solution. In this paper, a modified algorithm, multi-colony ant system based on a pheromone arithmetic crossover and a repulsive operator, is proposed to avoid such stagnating state (Dorigo et al., 2006). In this algorithm, firstly several colonies of ant system are created, and then they perform iterating and updating their pheromone arrays respectively until one ant colony system reaches its local optimum solution. Every ant colony system owns its pheromone array and parameters and records its local optimum solution. Furthermore, once an ant colony system arrives at its local optimum solution, it updates its local optimum solution and sends this solution to global best-found centre. Thirdly, when an old ant colony system is chosen according to elimination rules, it will be destroyed and reinitialized through application of the pheromone arithmetic crossover and the repulsive operator based on several global best-so-far optimum solutions. The whole algorithm implements iterations until global best optimum solution is searched out.

II. METHODOLOGY

The methodology employed for this research integrates the application of the ant colony optimization algorithm as a means to mitigate corrosion in pipelines. The process commenced with the development of an oil spillage probability formulation model. This model served as the foundation for understanding the potential risk of corrosion-related oil spillage occurrences within the pipeline system. Subsequently, the researchers implemented the ant colony algorithm, leveraging its capacity to simulate the behavior of real ant colonies seeking optimal paths. In this context, the algorithm was tailored to identify and target areas susceptible to corrosion, thereby facilitating the reduction of corrosion rates and the associated risks of oil spillage. By leveraging the collective intelligence of the algorithm, the paper aimed to enhance the overall resilience and longevity of the pipeline infrastructure, emphasizing the crucial role of intelligent algorithms in the realm of corrosion management and preventive measures within industrial settings.

A. Corrosion Reduction Model And Oil Spill Probability

This paper proposes a new model for oil-gas pipeline problem that is capable in reduce corrosion and addresses in the real situation. The mathematical model (Uthman, 2011; Adetunji, 2013; Emami, 2011)

$$minimize \sum_{i=1}^{n} Tc_i = \sum_{i=1}^{n} (LSD_I * cs) \quad (1)$$

Where LSD_I is the length of the pipe connecting two wells (km) and CS represents the cost of one pipe per km the following was used to interpretation was used to represent the real issue.

Interpretation 1-There exists an obstacle between two wells, this obstacle will lead to corrosion,W_i and W_j if the link between them is null as equation in (2) below. In this case, the distance between is zero as stated in (3).

$$\text{Link } (i, f) = \emptyset \quad (2)$$

$$D(W_iW_j) = 0, \forall\, link(i,j) = \emptyset \quad (3)$$

Interpretation 2: The distance between is zero for the same well given by

$$D(W_iW_j) = 0, \forall\, i = j \quad (4)$$

Interpretation 3: The connection between two wells, is possible in one direction only given by

$$D(W_iW_j) = 0, \forall\, D(W_iW_j) = d_i d_l \neq 0 \quad (5)$$

The distance W_i and W_j between interpret in (5) is given by

$$D(W_iW_j) = \sqrt{(x_i - x_l)^2 + (y_i - y_l)^2} \quad (6)$$

The new proposed model as below which is programmed using MATLAB software

*Ps*eudocode for New Proposed model

1. Input: WLT(X,Y) $\in R^{2*n}$ // $location\ table\ for\ all\ wells$
2. Output: shortPathTable
3. Begin:
4. Calcula$teD_{table} \in R^{n*n}$
5. For$i = 1{:}n$ Do // $i = l, 2, n;$
6. For $j = 1{:}n$ Do
7. If corrosion (i, j) = 1 THEN
8. $D(I,J) = \infty$
9. ELSE
10. $D(I,J) = SQR\left((X_i - x_j)^2 + (y_i - y_l)^2\right)$
11. End IF
12. Next
13. For well.$id = 2{:}n\ Do$
14. Determine short path for well (well.id)
15. Set $X \leftarrow well.id$
16. S_ID = Short Path(Well.id{D}) $\in R^{1*1}$
17. SET Well(well.id). Link = S_1D
18. SET D (Well.Id,S_ID)= ∞
19. SET $\gamma \leftarrow S\_ID$
20. Z = Short Path (Y, {D})
21. SET D(X,Z) = ∞,D(Z,X)=∞
22. ShortPathTable(Well. Id) =Well(Well. Id). Link
23. Next
24. End Algorithm

B. Development of Ant Colony Algorithm To Reduce the Oil Pipeline Corrosion and Oil Spill Probability

The ACO algorithm is an exploratory method capable of solving complex problems by looking for optimal solutions in the graphs within a range of possibilities. This algorithm mimics the natural behaviour of the ants in the search for food where ants come out to find food, and when it does, a chemical known as pheromone is released on the way back to the colony. The rest of the ants will pick up the scent and follows the same path. The more ants follow the path, the greater the concentration of the pheromone, which causes the long path to disappear as this material rapidly evaporates. In the end, there is only one path followed by the ants, which is the shortest path. On this basis, this algorithm is chosen for comparison purpose with the proposed algorithm. The standard ACO rule $p_{i,j}^k$ mentioned in equation (7)

$$p_{i,j}^k = \frac{[T_{i,j}][\gamma_{i,j}]^\beta]}{\sum_{\mathrm{i}}^{\mathrm{k}} zcallowed[T_{i,j}]^\beta][\gamma_{i,j}]^\beta]} \quad (7)$$

where $k \in \{1,2,3, \ldots \ldots . m\}$ is the number of ant, at node i. $p_{i,j}^k$ is the probability with which ant k chooses to move from node i to node j. $\gamma_{i,j}$ represents the amount of pheromone along the transition from node i to j. α is the parameter that controls the influence of $\gamma_{i,j}$, and $\gamma_{i,j}$ is the desirability of the node transition ij (a prior knowledge, typically $\frac{1}{d_{ij}}$ where d is the distance and $\beta \geq 1$ is a parameter that controls the influence of $\gamma_{i,j}$. While $\gamma_{i,j}T_{i,j}$ represents the attractiveness and trail level for the other possible node transition pheremonc update. When all the ant have complete a solution, trails are updated by $\gamma_{i,j} \leftarrow (1-\rho)\,\gamma_{i,j} + \sum_k^{\mathrm{i}} \Delta\tau_{ij}^k$, with

$$\Delta\tau_{ij}^k = \begin{cases} \frac{q}{l_k} & \text{if ant uses curve } ij \text{ in its tour} \\ 0 & \end{cases} \quad (8)$$

Where

l_k is the cost of the k_{th} ant's tour and q is a constant

Pseudo code for Ant Colony Algorithm

1. Input:WLT(X Y)∈ R^{n*n}// location Table all the wall
2. Output:ShortPathTable
3. Begin
4. Calculate $D_{Table} \in R^{n*n}$
5. For it =1: maxIt
6. For k = 1 :nAnt
7. Ant(k).Tour=randi([1nVar]);
8. For I=2:nVar
9. I= ant(k). Tour(end);
10. P=tau(I,:)^alph.*eta(I^beta;
11. P(ant(k).Tour)=0;
12. P=P/Sum(p)
13. J= RouletteWheelSelection(P)
14. Ant(k). Tour=[ant(k).tourj]
15. Ant(k).Cost = CostFunction(ant(k).Tour;
16. If ant(k).cost<bestsol.cost
17. BestSol=ant(k)
18. Update Phromones
19. For K=1:n Ant
20. Tour = ant(k).tour
21. Tour=[tour tour(1)];%#ok
22. For l=1;nVar
23. I= tour (1)
24. J = tour (l+1)
25. I = tou(ij) =tau(ij)+$\frac{Q}{ant(k).cost}$
26. Next

End algorithm

C. System Integration

The integration of the Ant Colony Algorithm for corrosion detection with the proposed algorithm for reducing oil pipeline corrosion and spill probability forms a comprehensive strategy. The Ant Colony Algorithm identifies corrosion-prone areas by optimizing paths, considering a defined cost function representing corrosion severity. The proposed algorithm, tailored for corrosion reduction, utilizes this information to calculate distances and paths, implementing protective measures. The integration combines these results, creating a holistic corrosion management approach. It continuously adapts based on real-time or periodic monitoring, optimizing strategies and scheduling maintenance for sustained effectiveness. This integrated system provides a robust solution for minimizing corrosion impact and spill probability in oil pipelines, offering a dynamic and responsive approach to pipeline integrity and safety. The lifecycle of the system Integration is reported in Figure 1

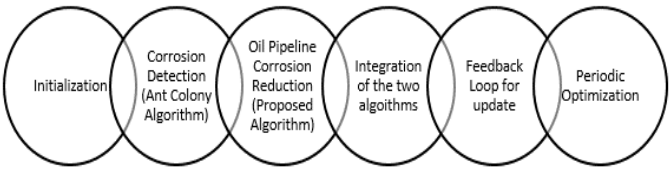

Figure 1: Lifecycle of the system integration

D. System Implementation

The developed ant-colony algorithm was implemented in the Java programming language. The Simulink model of the oil pipelines used in the case study was created using MATLAB Simulink 2018a. The study considered the properties of the X46, X60, and X80 oil pipelines. MATLAB Simulink provides Application Programming Interface (API) support for Java and C++ programming languages, enabling the loading of the Ant-colony algorithm code into its workspace for interaction with the MATLAB kernel. The Ant-colony program communicates with the MATLAB operating system object through Common Object Request Broker Architecture (CORBA) for seamless inter-object communication. This approach allowed the assessment of the performance of the proposed

Ant-colony techniques in corrosion detection and reduction for the specific oil pipelines. The simulation results were used to evaluate corrosion reduction and related factors, including the ratios of maximum von Mises stress and anodic current density concerning variations in defect depth.

III. RESULTS

To assess the impact of corrosion reduction on local maximum stress, this paper employs the maximum Ant-colony stress at a single corrosion reduction (top defect) as a reference, denoted as MaxSsingle. The stress concentration induced by overlapped defects is quantified as MaxSovercome/MaxSsingle, where MaxSovercome represents the maximum von Mises stress at the overlapped corrosion defects. Similarly, the maximum anodic current density at a single corrosion defect is labeled as MaxAsingle, and the effect of overlapped corrosion defects is evaluated through the MaxAovercome/MaxAsingle ratio, where MaxAovercome signifies the maximum anodic current density at the overcome corrosion defects.

Figure 2 illustrates the relationship between the maximum ant colony at overcome corrosion defects and that at a single defect, i.e., MaxSovercome/MaxSsingle, as a function of the ratio of defect depths, d2/d1, with d1 set at 4 mm and varying d2. It is evident that the presence of overlapped corrosion defects amplifies stress concentration compared to that at a single defect. As the d2/d1 ratio increases, signifying greater depth of the bottom defect, MaxSovercome/MaxSsingle also increases, indicating an escalation in local stress concentration with deeper bottom defects. Additionally, the impact of defect length on stress concentration is determined. The figure reveals that, at specific defect depth ratios, an increase in defect length results in elevated local stress concentration. For instance, at a d2/d1 ratio of 0.1, the maximum von Mises stress ratio is approximately 1.0 for three pairs of defect lengths (L1 and L2). However, when the d2/d1 ratio is 1.0, the maximum von Mises stress ratios increase to 1.16, 1.29, and 1.36 for defect lengths of L1 and L2, including 0.5l and 2l, and 1.5l and 3l, respectively. Therefore, as corrosion defects grow longer, the maximum von Mises stress ratio becomes larger at specific d2/d1 ratios, indicating that, while the defect depth remains constant, the length of the corrosion defect also significantly influences increased stress concentration.

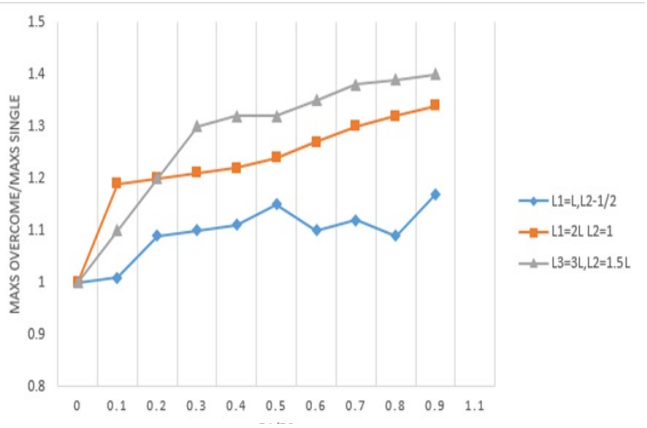

Figure 2: Proposed ant-colony ratio of the maximum ant-colony at overcome corrosion defects to that at the single defect

Figure 2 shows the proposed ant-colony ratio of the maximum ant-colony at overcome corrosion defects to that at the single defect, i.e., MaxSovercome /MaxSsingle, as a function of the ratio of the defect depth, i.e., D2/D1, where D1 is 4 mm and D2 is varied. The ratios of the maximum anodic current density at the overcome corrosion defects to that at the single defect, i.e., MaxAovercome / MaxAsingle, as a function of the defect depth, i.e., d2/d1, where d1 is 4 mm and d2 is varied are shown in Figure 3. Generally, the maximum anodic current density ratio increases with the increasing depth ratio, indicating that the presence of the bottom corrosion defect enhances the ant-colony on local corrosion growth, as compared to the single defect. With the increase of the lengths of the corrosion defects, the maximum anodic current density ratio increases rapidly at specific

defect depth ratios. Therefore, the proposed ant-colony at the overcoming corrosion defects also increases with the defect length.

Figure 3 shows the proposed ant-colony model based on Ratios of the maximum anodic current density at the overcome corrosion defects to that at

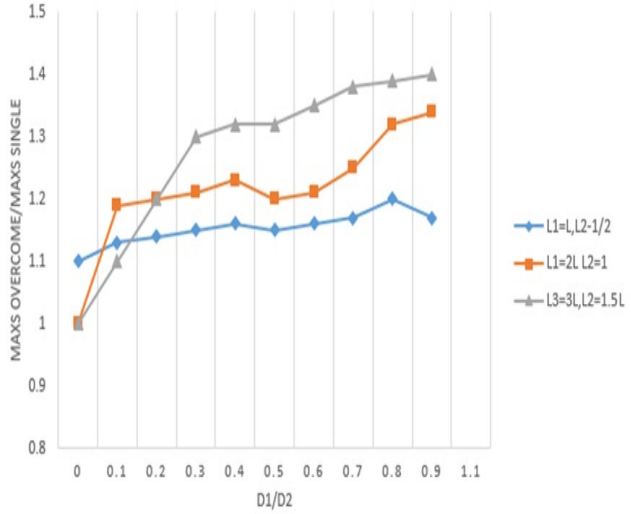

Figure 3: Proposed Ant-colony model based on Ratios of the maximum anodic current density at the overcome corrosion defects to that at the single defect

the single defect, i.e., MaxAovercome / MaxAsingle, as a function of the defect depth, i.e., d2/d1, where d1 is 4 mm and d2 is varied. In the figure 2, where MaxAovercome is the maximum anodic (corrosion) current density at locations with multiple corrosion defects, and MaxAsingle is the maximum anodic current density at a location with a single defect. The result takes into account the depth of the defects, which is represented by the ratio "d2/d1," where d1 is a constant value of 4 mm, and d2 is the depth of the corrosion defect. By varying the depth of the corrosion defects (d2), the model aims to understand how the ratio of anodic current densities changes as the defects become deeper or shallower.

This approach is valuable in corrosion analysis because it helps assess the severity of multiple corrosion defects compared to a single defect and how this severity changes with different defect depths. The ant-colony model likely uses these ratios to guide decisions or actions in managing corrosion in materials or structures, such as determining the most critical areas for repair or monitoring based on the depth and density of defects.

IV. CONCLUSION

In this paper, Ant-colony models were developed to reduce the corrosion of oil pipeline X46, X60 and X80 oil pipelines containing multiple corrosion defects with varied geometries and orientations by assessing the mutual interaction of the defects and the effect on pipeline integrity. Generally, the reduction of pressure of corroded pipelines decreases with the increasing interaction between corrosion defects. There is little effect of the pipeline grade on the interaction between defects. The interaction mainly depends on the mutual orientation of the defects and their geometry and spacing. Compared to circumferential corrosion defects, the longitudinal defects are associated with a larger spacing where the interaction between corrosion defects exists. The circumferential spacing of corrosion defects has a smaller impact on the failure pressure of corroded pipelines compared to the longitudinal spacing. The M-E effect resulting in a more negative corrosion potential and a larger anodic current density were found at the defect adjacency compared to the uncorroded area, resulting in accelerated localized corrosion around the defects. Due to the existence of the M-E effect, the interaction rule used to determine the critical spacing of adjacent corrosion defects should be redefined due to the synergism of multiple physics fields (e.g., stress field and electrochemical corrosion field) at the corrosion defects. It was also found that, for the circumferentially aligned corrosion defects, although the interaction between them is marginal when the pipelines primarily experience the hoop stress generated by an internal pressure, it can be significant when the pipeline is under an axial stress due to ground movement. This is because the maximum von Mises stress around the corrosion defects on stressed oil pipelines is located at the area perpendicular to the direction of the stress, while the minimum von Mises stress is at the area parallel to the stress direction. Under an internal pressure, the von Mises stress of the area between the

circumferentially aligned defects the lowest. However, under a tensile stress, the von Mises stress at the area between defects can be the highest. Therefore, the interactions are much more apparent, which also accelerates corrosion at the defects and their adjacency due to the M-E coupling effect.

The presence of overlapped corrosion defects results in a local stress concentration and enhanced M-E effect on corrosion defect growth. The maximum stress always generates at the corner of the bottom defect, which can exceed the ultimate tensile stress of the steel even under normal operating pressures while the stress in the pipe wall below yielding stress. The enhanced M-E effect causes an accelerated corrosion at the bottom defect, resulting in the rapid defect growth to cause pipeline leaking. The geometry of corrosion defects, especially the defect depth and length, affects local stress concentration and the M-E effect. With the increasing length and depth of either top or bottom corrosion defects, the overall stress level increases, but the effect is more apparent at the bottom defect. Similarly, the increased M-E effect due to the increasing length and depth of the corrosion defects results in a more accelerated corrosion at the bottom defect than the top one. In this work, Ant-colony models enabling the reduction of the failure pressure of pipelines containing a dent associated with corrosion feature were also developed. The interaction identification rule based on determination of the failure pressure of pipelines containing a dent with adjacency to a corrosion feature is proposed to assess the critical spacing between them to enable a mutual interaction to decrease the failure pressure. Moreover, the interaction between the dent and the corrosion feature is determined quantitatively by numerical modelling as a function of the corrosion length, corrosion depth and the dent depth

REFERENCES

Achebe C., Nneke U., & Anisiji O., (2012) "Analysis of Oil Pipeline Failures in the Oil and Gas Industries in the Niger Delta Area of Nigeria", Proceedings of the International Multiconference of engineers and computer scientists. Vol II IMECS 2012, March 14-16, 2012 Hong Kong

Adetunji O., (2013) "Modelling and Simulation of Pipeline Corrosion in the Oil and Gas Industries", Corrosion and Materials in the Oil and Gas Industries Chapter · October 2013 DOI: 10.1201/b14703-17

Di-Capro D., Ebrahimnejad A., Alrezaamiri H., & Santos-Arteaga F., (2022) "A novel ant colony algorithm for solving shortest path problems with fuzzy arc weights", Alexandria University Alexandria Engineering Journal https://doi.org/10.1016/j.aej.2021.08.058

Dorigo M., Birattari M., & Stutzle T., (2006) "Ant Colony Optimization", Institut de Recherches Interdisciplinaires et de D´eveloppements en Intelligence Artificielle UNIVERSITE´ LIBRE DE BRUXELLES Av F. D. Roosevelt 50, CP 194/6 1050 Bruxelles, Belgium – Technical Report Series Technical Report No. TR/IRIDIA/2006-023

Emami M., (2011) "Mathematical modelling of corrosion phenomenon in pipelines", The Journal of Mathematics and Computer Science Vol .3 No.2 (2011) 202 – 211

Husseini T., (2018) "Transporting Oil and Gas: The world's longest pipeline", Offshore Technology. The world's longest pipelines in the oil and gas industry (offshore-technology.com) Accessed November 2023

IBM (2017) "Common Object Request Broker Architecture (COBRA)", IBM Integration Bus. Common Object Request Broker Architecture (CORBA) - IBM Documentation Accessed November 2023

Sallim J., Hussin W., Abdullah R., & Khader A., (2006) "A Background Study on Ant Colony Optimization Metaheuristic and its Application Principles in Resolving Three Combinatorial Optimization Problems" School of Computer Sciences, Universiti Sains Malaysia, 11800 Penang, Malaysia

Stutzle T., & Hoos H., (2000) "Max-Min Ant System", FG Intellektik, TU Darmstadt, Germany Preprint submitted to Elsevier Science

Uthman H., (2011) "Mathematical Modelling and Simulation of Corrosion Processes in Nigerian Crude Oil Pipelines", Journal of Dispersion Science and Technology, 32: 4, 609 — 615

Wu S., Li Q., & Wei W., (2023) "Application of Ant Colony Optimization Algorithm Based on Triangle Inequality Principle and Partition Method Strategy in Robot Path Planning". Axioms 2023, 12, 525. https://doi.org/10.3390/axioms12060525

Journal of Engineering, Emerging Technologies and Applied Sciences -– Volume 1 Issue 2, Nov. 2023

Available at ***https://www.ndu.edu.ng/journalofengineering/***

RESEARCH ARTICLE OPEN ACCESS

ASSESSMENT OF STRESS- STRAIN BEHAVIOUR OF SEA SAND SANDCRETE BLOCKWALLS WITH DIFFERENT MIX RATIOS

WENAPERE Ambakederemo Dio *, ORUMU T. Solomon**

*(Department of Agricultural / Environmental Engineering,
Niger Delta University, Wilberforce Island, Bayelsa State, Nigeria
e-mail: wenaperedio@ndu.edu.ng)

** (Department of Civil Engineering
Niger Delta University, Wilberforce Island, Bayelsa State, Nigeria
e-mail: solorumu@yahoo.com)

----------**********----------

Abstract:

Irrespective of the wide technical reports on masonry structures, especially concrete structures there appears to exist a serious gap in research on sandcrete blocks, particularly the stress-Strain characteristics of failure of sandcrete blockwalls using sea sand. And painfully it appears no such research based on the structural model of prototype block units, which therefore constitutes the major focus of this research work. The strength evaluation tests for the physical and mechanical properties of sandcrete block units and block walls were carried out in accordance with BS 5628(1978) and NIS 74(1976). The compressive strength of blockwall with model sandcrete blocks varied with the strength of the sandcrete block units, the mortar strength and the length to height ratio of block wall. The numerical values averaged 9.30N/mm^2, 9.10N/mm^2, 6.85N/mm^2 and 6.40N/mm^2 for 1:4, 1:6, 1:8 and 1:10 mixes respectively. Thus, a systematic analysis of the effects of mix ratio, water-cement ratio, block and mortar strength on the resistance and failure mechanism of sandcrete blockwall, reported herein, provides good evidence of the reproducibility of prototype behaviour of sandcrete block wall by its ¼ -scale model. These conclusions open a wider scope and opportunity for research into sandcrete masonry structures especially, where heavier and expensive facilities for full-scale tests are not available. This study of investigation of stress- strain behaviour of sea sand sandcrete blockwalls using different mix ratios is aimed at providing knowledge on sandcrete blocks usage as walling materials in the construction of buildings.

Keywords — Stress- Strain, River Sand, Sandcrete Blockwalls

----------**********----------

I. INTRODUCTION

Different type of studies has been conducted on the stress-strain behaviour of masonry, especially on concrete, but it appears to be very few works on Sandcrete blocks and possibly no work on sea sand blocks. Abrams, D. P. and T. J. Paulson, (1991) and other researchers developed a non-linear stress-strain relationship for the walls they tested. Nuruddeen Muhammad Musa (2021) reported Strength Evaluation of Textile Fabric Fibre-Reinforced Sandcrete blocks using Schmidt Rebound hammer to evaluate the effect of textile fabric fibre on the strength properties of hollow sandcrete blocks

Masia, M.J., Kleeman, P.W. and Melchers, R.E., (2002) found that the stress-strain curve varied with

different types of mortar and unit. Ephraim, M.E. Chinwah J.G, Orlu I.D (1990) also found a variation in stress-strain behaviour and concluded that for design purposes different moduli should be used for the different types of masonry structures.

In the working stress range, the stress-strain relationship is essentially linear, although the modulus of elasticity is expected to vary with both materials and geometric configuration.

Stress-strain data were obtained from these test
The importance of housing in socio-Economic Development cannot be over emphasized. The great needs to reduce cost of buildings and therefore increase affordability and availability of housing for the ever-increasing population of the Nigerian citizenry has features as an important policy thrust of Government over the years. This has also continued to receive attention at the various works conferences of the Ministry of Works and Housing till dates,

However, while other local materials such as lateritic concrete and sandcrete are receiving some form of research attention, there appears to be little or no conscious research efforts in alternative building designs and appropriate construction technology development. The focus of this research therefore, is to investigate the structural adequacy and economic effectiveness of application of structural sandcrete hollow blocks for housing development using ¼ scale structural model.

Houses up to four floors using masonry unit in the form of concrete blocks and structural bricks as load bearing walls (without frame) have been in use for a very long time. This is also as reported by Kalluru.Rajasekhar, M.Praveen Kumar (2021) and Marco Breccolotti, Antonella D'Alessandro , Francesca Roscini, Massimo Federico Bonfigli (2015). Sandcrete blocks (hollow and solid) are extremely popular in Nigeria as walling material used in walls and partitions. Hallow blocks have the added advantage of increased stability, material economy and relative heat insulation than the solid block.

OBJECTIVE OF STUDY

1. To study the practical utilization of sandcrete blockwalls as load bearing members
2. To increased study and research into the quality of sandcrete materials, technology and workmanship of its application in buildings.
3. To verify and ensure the safety, durability, serviceability and reliability of sandcrete block building structures.
4. To add or contribute to bridge the gap of scanty information on the application of structural modelling to blockwalls, especially the sandcrete blockwalls.

DEFINITION OF PROBLEM

The study is justified based on the actuality of the need for more serious studies into the strength and deformations of sandcrete blocks materials and structures, especially in Nigeria where it enjoys extensive application. Such research will be geared towards development of greater evidence of the structural behaviour of sandcrete wall which when incorporated into design will provide greater guarantee of safety and reliability of the structure made from it. The problem being investigated can therefore be defined as that of determination of the structural characteristics of behavior and resistance of sandcrete blockwall under various conditions of loading based on structural models.

METHODOLOGY OF RESEARCH

This research work is intended as a contribution to bridge the gap of scanty information on the application of structural modelling to blockwalls,

especially the sandcrete blockwalls. Its focus consists mainly in the application of similarity mechanics and laboratory models to determine the structural behaviour of sandcrete blockwall under various loading conditions. This research work is aimed at achieving the following objectives.

a) Produce model sandcrete blocks at the selected optimum water-cement ratios, cure and erect model blockwalls for compressive strength test.
b) Select and structure loading arrangement and instrumentation.
c) To determine the structural behavior of sandcrete blockwalls under compressive loads of ¼ scale model sandcrete units.

OPPORTUNITIES AND CONSTRAINTS

A proper structural model reproduces the physical and mechanical behaviour of the complete structure; hence it presents an opportunity for research workers to test sandcrete structures in the laboratories using reduced scale structural model.

Generally, the prime motivation to conduct experiments on structural model at reduced scales is to reduce the cost and proper engineering property determination. Cost reductions comes about from three areas:

- Reduction of loading equipment and associated restraint frames
- Reduction in the restraint and load reactant frames
- Reduction in cost of fabrication, preparation, and disposal of test structure after testing

The major limitations of using structural models in a design environment are those of time and expense. In comparing physical models with analytical models, we find that the analytical models are normally less expensive and faster, and we cannot expect physical models to replace analytical modelling of structures when the analytical model procedure leads to acceptable definition of behaviour of the prototype structure. Thus, physical models are almost always confined to situations where the mathematical analysis is not adequate or not feasible. However, the behaviour of a blockwall comprising sandcrete blocks with big hollows and bonded with yet another material (mortar) require complex mathematical analysis and modelling is indicated as a most feasible study approach.

As stated earlier the strength of blockwalls depend on the block strength, mortar type and length to height ratio of wall. In the present studies, three variants of mortar and block strength were investigated. However, the loading was limited to compressive loads only.

Further work will be required to determine the flexural strength of the sandcrete blockwall in line with BS 5628 (1978) and other relevant standards.

MATERIALS FOR THE TESTS

The materials used in this research were basically sea sand, obtained from a local source in Sangana Akassa Bayelsa State: Cement (Dangote cement brand) and water from the Niger Delta University borehole, a 450X 150 X 225mm steel block mould.

PREPARATION OF TEST SPECIMENS

Model Sandcrete Blockwalls

The model blockwalls were constructed in accordance with BS 5628 (1978) to a ratio of height to horizontal dimension of 1.6, which BS 5628 allows, and were carefully placed by adopting the vertical bonding technique Becica et al (1977).

Thus, the accuracy of this method is greatly dependent on workmanship. To give vertical and horizontal alignment, an alignment board was used. The horizontal lines were set at a predetermined height proving for unit height plus mortar joint. The plumb line establishes vertical reference. Mortar was then trowelled on to the face shells of pre-soaked units while adjoining units were placed accordingly with firm pressure, causing mortar to squeeze out of the joint. This movement allows for vertical and horizontal alignment and establishment of the joint thickness. Gentle tapping with the trowel was required to further consolidate joints. After the specimen was boned, it was removed from the casting frame, and all the joints were pointed using the tip of a small trowel, as care was taken to ensure complete joint filling.

Results of the test performed on various mixes at water–cement ratio of 0.5 investigated are presented in Tables 1 to 4. Sandcrete blocks like many other structural materials appear to have elastic properties to some extent under load. This means that under increasing loads, stresses and strains are expected to increase. The strain readings were taken with DEMEC mechanical strain gauge placed at middle two-thirds of the blockwalls height. Strain readings recorded were taken immediately after loading, as shown in Plate 1 during testing of walls.

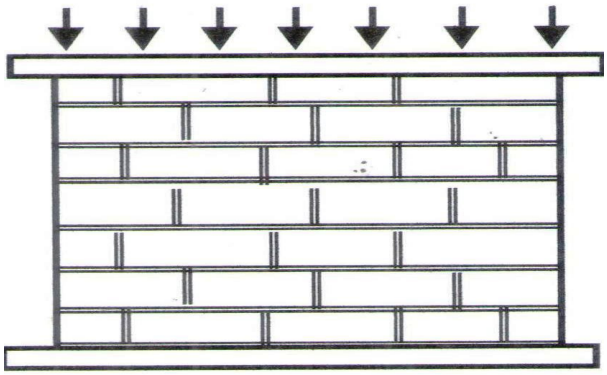

Figure 1: Loading Perpendicular to Bedding

PLATE 1: MEASUREMENT OF STRAINS (X-DIRECTION)

The loads were applied uniformly over the whole area of the top of the panel.

The platen through which the load was applied was restrained against rotation to produce a flat-ended condition as shown in Figure 1.

Generally, the load was applied at an increasing rate. The individual test results for the model wall are as shown in Tables 1 to 4.

The height to length of all the blockwalls was maintained at 1.6.

TEST RESULTS

The Tables below are results obtained from the various tests conducted in this research work as presented in Tables 1 – 4

Table 1: Stress- Strain Behaviour of Model Blockwall for Mix 1:4 (L/H= *1.6)*

S/No.	Applied load KN	Compressive Stress N/mm^2	Lateral Strain (x-Direction) (X10^{-5})	Longitudinal Strain (y – Direction) (X10^{-5})
1.	10.0	0.59	3.32	11.84
2.	25.0	1.48	7.60	30.40
3.	50.0	2.96	15.34	60.38
4.	100.0	5.90	29.30	115.40
5.	157.0	9.30	44.40	177.60
6.	150.0	8.9	56.02	223.2
7.	126.5	7.5	67.14	264.33

Table 2: Stress- Strain Behaviour of Model Blockwall for Mix 1:6 (L/H= 1.6)

S/No.	Applied load KN	Compressive Stress N/mm^2	Lateral Strain (y-Direction) (X10^{-5})	Longitudinal Strain (x – direction) (X10^{-5})
1.	10.00	0.59	20.20	5.67
2.	25.00	1.48	51.04	14.65
3.	50.00	2.96	87.50	24.50
4.	100.00	5.90	155.40	43.90
5.	153.00	9.10	230.98	65.60
6.	145.00	8.9	285.00	81.80
7.	138.40	8.2	303.00	92.00

Table 3: Stress- Strain Behaviour If Model Blockwall For Mix 1:8 (L/H= 1.6)

S/No.	Applied load KN	Compressive Stress N/mm^2	Lateral Strain (x-Direction) (X10^{-5})	Longitudinal Strain (y – direction) (X10^{-5})
1.	10.00	0.59	9.85	28.97
2.	25.00	1.48	23.00	70.98
3.	50.00	2.96	48.00	148.60
4.	100.00	5.90	98.50	303.00
5.	116.00	6.85	112.30	348.80
6.	114.80	6.80	123.40	403.20
7.	99.60	5.90	132.00	451.90

Table 4: Stress- Strain Behaviour of Model Blockwall for Mix 1:10 (L/H= 1.6)

S/No.	Applied load KN	Compressive Stress N/mm^2	Lateral Strain (x-Direction) (X10^{-5})	Longitudinal Strain (y – direction) (X10^{-5})
1.	10.00	0.59	26.99	112.00
2.	25.00	1.48	67.77	275.80
3.	50.00	2.96	135.30	551.60
4.	100.00	5.90	271.90	1122.90
5.	108.00	6.40	454.50	1298.70
6.	101.00	6.00	460.00	1320.00

STRESS - STRAIN RELATIONSHIP

The graphs in figure 2 demonstrated an approximately linear stress- strain relationship extending to about 90 percent of the maximum strength of the sandcrete walls tested in this study. This is followed by a non-linear segment of the curve up to the point of failure which was more clearly expressed for blockwall made with 1:6 and mixes sandcrete blocks.

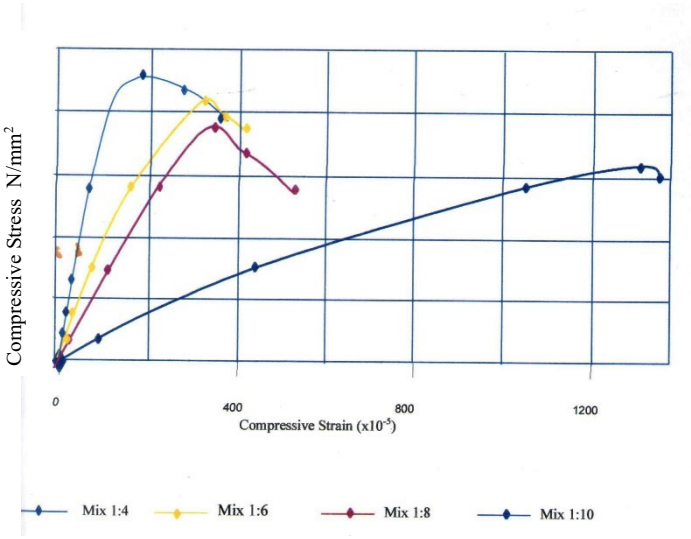

Figure 2: Stress- Strain Curves for Blockwall of Various Mixes At 28 Days and W/C = 0.5

The stress-strain curves for the various blockwall types SBW-1, SBW-2 SBW- 3 and SBW-2 tested are shown in on Figure 2, the maximum of major characteristics values are tabulated in Table 5

Table 5: Failure Loads and Stress-Strain Characteristics of Model Sandcrete Blockwalls

Mix Ratio	Lateral Strain x-Direction (x 10^{-5})	Longitudinal Strain Y-Direction (x 10^{-5})	Compressive Strength N/mm^2	Modulus of Elasticity, (kN/mm^2) $E = \frac{\sigma y}{Ex}$	Poisson's Ration, υ $\upsilon = \frac{\varepsilon x}{\varepsilon y}$
1:4	67.14	264.33	9.30	20.950	0.25
1:6	92.00	303.00	9.10	13.870	0.28
1:8	132.00	451.90	6.85	6.100	0.32
1:10	460.00	1320.00	6.40	1.890	0.35

CONCLUSION

The analysis of tests results of compressive strength of ¼ model sandcrete masonry blockwalls as a function of strength of the block units and mortar strength show that:

1. Sandcrete blockwalls exhibit a linear stress-strain relationship almost up to the maximum strength, after which, a decrease in strength was observed. The measured longitudinal and transverse strains decreased from the stronger mix of 1:4 to the weaker and mix of 1:10.
2. The maximum strains varied within narrow limits of 264.33 x 10^{-5} for 1:4 and 1:10 mixes. The compressive strength showed a reversed trend with maximum values of 9.30, 9.10, 6.85 and 6.40N/mm^2 for 1:4, 1:6, 1:8 and 1:10 mixes respectively.
3. The modulus of Elasticity ranged from 20.95N/mm^2 for 1:4 and 1:10 mixes. The corresponding value for Poison's ratio were 0.25 and 0.35.

RECOMMENDATIONS

The above conclusion has substantiated the applicability of the Code of Practice recommendation in respect of use for models for analysis and design, with reference to ¼ scale model. The unique contribution of this research is the extension of the codes recommendation to sandcrete masonry structures, thus opening the potential, scope an opportunity for research in sandcrete masonry structures especially in Nigeria and elsewhere sophisticated and heavy equipment are not available for prototype scale tests. To this end, model tests are recommended to study the strength durability and failure mechanism of the masonry structures in other stressed states including flexure, shear, dynamic loading and

their combination such that the national concern on building collapses will ultimately receive a practical solution.

REFERENCES

Abrams, D. P. and T. J. Paulson, (1991), "Modeling Concrete Masonry Building Structures at One-quarter Scale", Structural journal of the American Concrete Institute, No. 88-S50, Vol.88, No .4, pp. 475- 485.

Becica, I.J. and Harris, H.G. (1977), "Evaluation of Techniques in the direct modeling Of Concrete Masonry Structures", Structural Models laboratory Report No.M77-1, Department of Civil Engineering Drexel University, Philadelphia,

British Standard Institution (1978), "Structural Use of Masonry. Part 1. Unreinforced masonry". BS 5628 (London, BSI).

Ephraim, M.E. Chinwah J.G, Orlu I.D (1990) "Mechanism Approach to Composite Frame and Infill". Proceedings of the second international Conference on Structural Engineering Analysis and Modeling (SEAM 2), University of Science and Technology, Kumasi Ghana, Vol. 1 pp 13 -26

Kalluru.Rajasekhar, M.Praveen Kumar (2021), Stress-Strain Behaviour Of Confined Normal Grade Concrete; International Journal of Professional Engineering Studies Volume Viii /Issue 3 / Mar 2017 Ijpres

Masia, M.J., Kleeman, P.W. and Melchers, R.E., (2002) "Soil Structure Interaction Modeling of Mansonry for Reliability Studies" 17th Australasian conference on the Mechanics of Structures and Materials, Gold Coast, Queensland, Australia.

Marco Breccolotti, Antonella D'Alessandro , Francesca Roscini, Massimo Federico Bonfigli (2015) INVESTIGATION OF STRESS - STRAIN BEHAVIOUR OF RECYCLED AGGREGATE CONCRETE UNDER CYCLIC LOADS Environmental Engineering and Management Journal July 2015, Vol.14, No. 7, 1543-1552 http://omicron.ch.tuiasi.ro/EEMJ/ "Gheorghe Asachi" Technical University of Iasi, Romania

Nuruddeen Muhammad Musa (2021) "Strength Evaluation of Textile Fabric Fibre-Reinforced Sandcrete blocks using Schmidt Rebound hammer", Civil Engineering Department, Kano University of Science and Technology, Wudil , Proceedings of the 19th International Civil Engineering Conference and AGM at Asaba, 13th – 15th October 2021.

Ndubura E.E (2000), "Flexural Strength of Mortars Stabilized with vegetable fibres as low-cost materials for farm structures". Journal of Agricultural Engineering and Technology.

Nigerian Industrial Standard NIS 74; (1976) "Specification for burnt clay building units".

Osunade J. A., and Fajobi (2000) "Some Engineering Properties of laterite/Cement Masonry blocks made with hand-operated moulding machine granite fine and admixtures as factors" Journal of Agric. Engineering and Tech., pp. 44-50.

Proceedings of the 8th conference of the National Council on Housing, Federal Ministry of Works and Housing, Calabar, 17th September 1997.

Proceedings of the 8th conference of the National Council on Housing, Federal Ministry of Works and Housing, Kwara State, July 1997.

Stroven P. (2002) "Damage in Compressed Masonry due to Stress Release". Proceedings of the Fourth International Conference on Structural Engineering Analysis and Modeling (SEAM 4), University of Science and Technology, Kumasi, Ghana, Vol. 1, pp. 162-17.

Journal of Engineering, Emerging Technologies and Applied Sciences -– Volume 1 Issue 2, Nov. 2023

Available at ***https://www.ndu.edu.ng/journalofengineering/***

RESEARCH ARTICLE OPEN ACCESS

Microgrid Congestion Management Using Swarm Intelligence Algorithm

Amasa Ukwuoma Emmanuel, Ayebatorudigite Friend James

Department of Electrical and Electronic Engineering, Federal University Otuoke, Nigeria

Email: amasaeu@fuotuoke.edu.ng

----------**********----------

Abstract:

Microgrids have emerged as promising solution to address the challenges of modern power systems, offering increased reliability, efficiency, and integration of renewable energy sources. However, the efficient management of power flow within microgrids is crucial to maintain stability and prevent congestion issues. This study focuses on employing a Swarm Intelligence Algorithm, specifically Particle Swarm Optimization (PSO), for optimizing power flow and managing congestion within a microgrid in Cape Formoso Island in Brass Local Government Area, Bayelsa State, Nigeria. The research investigates the application of PSO in optimizing power flow by dynamically reconfiguring the distribution of power among various distributed energy resources (DERs) within the microgrid. The PSO algorithm is utilized to find the optimal settings for power generation, load distribution, and energy storage allocation to alleviate congestion and improve the overall performance of the microgrid. PSO's ability to iteratively search for optimal solutions is leveraged to minimize power losses, maintain voltage stability, and mitigate congestion while considering the variability of renewable energy sources and fluctuating demand. Simulation results demonstrate the effectiveness of the PSO-based optimization approach in managing congestion within the microgrid. This research contributes to the advancement of optimization techniques for microgrid management, offering insights into the practical application of PSO algorithms for congestion management, paving the way for more resilient and sustainable energy systems.

Keywords - **Microgrid, Congestion management, Swarm intelligence, Particle swarm optimization (PSO), Distributed energy resources (DERs).**

----------**********----------

I. INTRODUCTION

The strategies and processes employed in microgrids to ensure dependable and efficient power flow, particularly in times of high demand or constrained capacity, are known as congestion management .Curtailment, energy storage systems (ESS), demand response (DR), and reactive power management are among the congestion management strategies that have been put forth and examined in a number of studies (Nadali et al., 2017).

Curtailment is a fast but ineffective way to match the energy demand by restricting or lowering the output of distributed energy resources (DERs). Meanwhile, energy storage systems (ESS) increases the dependability and adaptability of a microgrid by storing extra energy produced during off-peak hours for use during peak hours. Demand response (DR) entails modifying patterns of energy consumption to correspond with supply, raising demand during off-peak hours and decreasing it during peak hours.

Numerous studies on congestion management have been carried out to date. For instance, generator rescheduling and actual power loss reduction are two strategies for managing congestion that Raja et al. (2011) suggested. FACTS devices are recommended by Joorabian and Saniei (2011), as a means of controlling transmission-level congestion.

Li et al. (2020), conducted a study which suggests that the integration of DR and ESS can effectively mitigate congestion in microgrids. Additionally, the study demonstrated that utilising ESS and DR together was more successful in reducing congestion than utilising ESS alone. Also, a different study by Wang et al. (2020), suggested a dynamic pricing-based distributed resistance technique that can lower microgrids peak demand and increase the microgrids viability economically.

Equally, Sarwar and Siddiqui (2015), claimed that optimization techniques play a pivotal role in enhancing the efficiency and stability of microgrids, particularly in addressing congestion issues within power networks. For them, swarm intelligence algorithms, such as Particle Swarm Optimization (PSO), have emerged as powerful tools for managing congestion in microgrid power flow. These algorithms mimic the collective behavior of social organisms and have demonstrated remarkable success in solving complex optimization problems.

The optimization of power flow in microgrids using PSO has garnered significant attention due to its ability to efficiently manage congestion while maintaining grid stability. As put forth by Kennedy and Eberhart (1995), PSO is inspired by the social behaviour of bird flocking and fish schooling, where individuals (particles) collaborate by iteratively adjusting their positions to find the optimal solution to a given problem.

In the context of microgrid power flow optimization, PSO algorithm's adaptability, simplicity, and capability to handle nonlinear and non-convex problems makes it a promising approach. Studies by researchers like Mogaka et al. (2020), Yeongho et al. (2017), Sayed and Kamel (2017), have shown that PSO effectively addresses power flow optimization challenges by minimizing transmission line losses, voltage deviations, and alleviating congestion issues in microgrid networks.

The essence of PSO lies in its iterative optimization process, where particles in the solution space dynamically adjust their positions based on their individual and neighborhood best solutions, guided by a set of predefined parameters. This collective intelligence allows the algorithm to efficiently explore the solution space and converge towards an optimal or near-optimal solution for power flow optimization in microgrids.

This paper seeks to delve deeper into the application of PSO for optimizing power flow and mitigating congestion in microgrids, providing insight into the underlying principles of PSO, its implementation strategies, and highlight case study and simulation results illustrating its effectiveness in managing congestion and optimizing power flow.

II. MATERIALS AND METHOD

A. Particle Swarm Optimisation (PSO)

PSO is a population-based optimisation algorithm that draws inspiration from the social behaviour of fish schooling and flocks of birds (Kennedy & Eberhart, 1995).

Accoding to Kumar and Subbaraj (2016), particle swarm optimisation (PSO) relies on particles working together to find optimal solutions by exchanging information about the positions that the entire swarm has found. Particles are able to efficiently explore different regions in the search space thanks to this social information exchange.

PSO has been successfully used to solve a variety of optimisation issues, such as image processing, engineering design, function optimisation, and training artificial neural networks. PSO has several benefits, such as ease of use, quick convergence, and suitability for high-dimensional issues. If not adjusted appropriately, it could experience premature convergence and become trapped in local optima.

In all, PSO offers a practical and efficient method for resolving optimisation issues by modelling the

group behaviour of particles within a search space. According to Tan (2016);

$$V_{ik}^{+1} = V_i^k + c_1 r_1(X_{pbest} - X_i^k) + c_2 r_2(X_{pbest} - X_i^k) \quad [1]$$

Where
$V_i^{k+1} = particle\ velocity\ at\ current\ iteration\ (k+1)$
$V_i^k = particle\ velocity\ at\ iteration\ k$
r_1, r_2: $random\ number$ between [0, 1]
c_1, c_2: $acceleration\ constant$
Particles new position:

$$X_i^{k+1} = X_i^k + V_i^{k+1} \quad [2]$$

Where;
X_i^{k+1} : $particle\ position\ at\ current\ iteration\ k+1$
X_i^k : $particle\ position\ at\ iteration\ k$
V_i^{k+1} : $particle\ velocity\ at\ iteration\ k+1$

B. PSO-Based System for Load Shedding

There are multiple steps involved in using Particle Swarm Optimisation (PSO) for microgrid congestion management according to Tan (2016) and Xu et al. (2023). The Particle Swarm Optimisation algorithm used for this work is shown in Fig. 1. The summary of the procedure is as follows:

1) ***Formulation of the problem:*** Power imbalance that is when the microgrid's total power generated is less than its load demand. This was given as:
Total power generated = 1.1MW
Load demand = 1.5MW.

2) ***Design of the objective function:*** An objective function is developed to quantify the microgrid's level of congestion. Its goal is to minimize the amount of loads shed while maximising power supply reliability and maintaining power balance.

3) ***PSO parameter setup:*** Particle size, maximum number of iterations, inertia weight, cognitive coefficient, and social coefficient are the parameters that are set. These parameters govern the algorithm's ability to explore and exploit.

4) ***Initialization:*** Generation of the initial population of particles at random to start the PSO algorithm. Every particle ought to have a position and velocity that indicate a possible way to handle traffic congestion.

5) ***Fitness evaluation:*** Using the objective function as a basis, each particle's fitness value is assessed. This demonstrated how successfully the specific solution handled the microgrid's congestion problem.

6) ***Update particle positions and velocities:*** In an effort to find better answers, the particle positions and velocities are modified. The particle's current position, the optimal location the particle found on its own (cognitive component), and the optimal location the swarm discovered (social component) serve as the basis for these updates.

7) ***Termination criteria:*** The algorithm's termination criteria, such as completing a predetermined number of iterations or reaching a target fitness value are established. The algorithm's end of iteration is determined by these criteria.

8) **Extract optimal solution:** The best solution is taken from the positions of the particles as soon as the PSO algorithm converged. In order to control congestion in the microgrid, the optimal distribution of power and resources is indicated by the solution.

C. Data Analysis

The research data utilised for this study are listed in Table I and Table II.

TABLE I
LOAD DATA OF THE MICROGRID

Load Bus	Power	Criticality
Bus 1	120	3
Bus 2	210	2
Bus 3	200	3
Bus 4	100	3
Bus 5	50	2
Bus 6	193	1
Bus 7	170	2
Bus 8	107	2
Bus 9	130	3
Bus 10	170	1
Total Load	1.5MW	

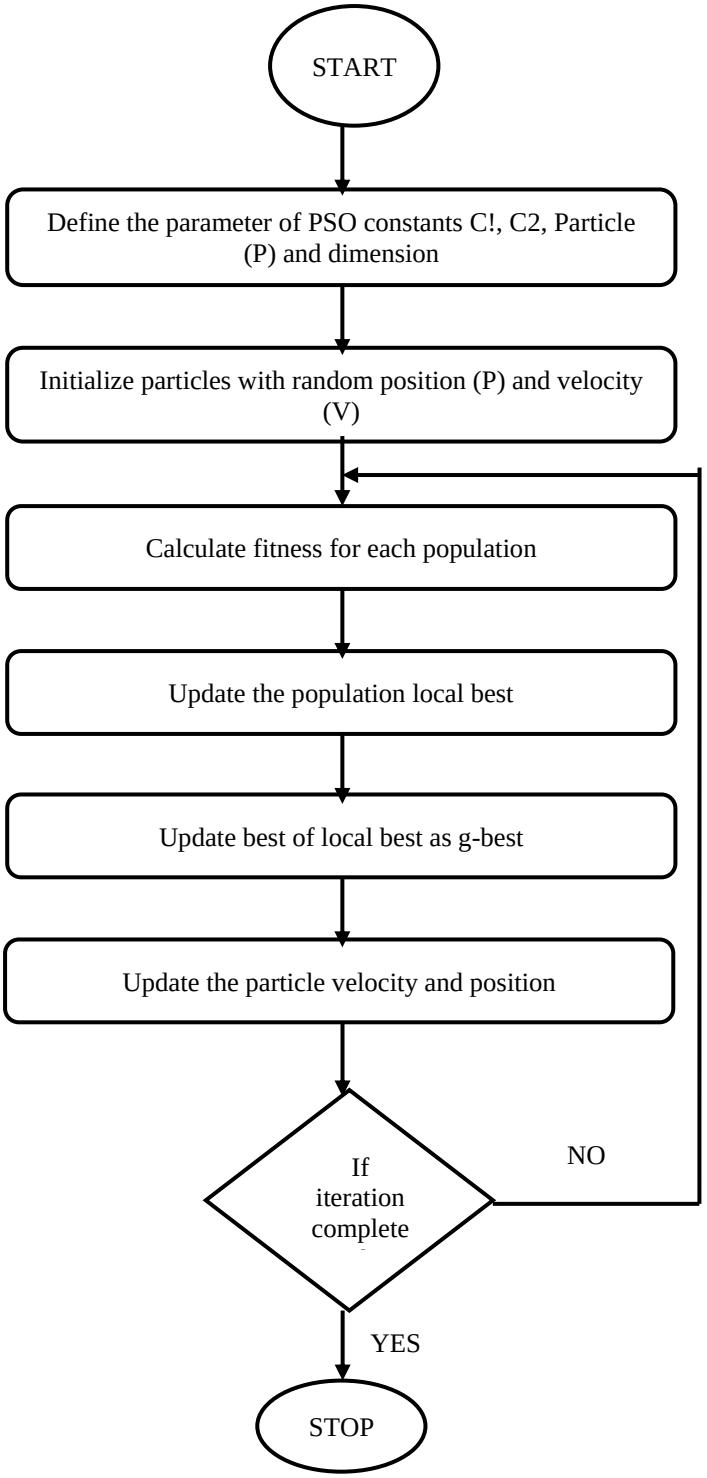

Fig. 1 Flowchart of particle swarm optimization algorithm.

TABLE II
GENERATION DATA

Source Type	Capacity	Duration
Wind	600KVA	16 hrs
PV System	500KVA	8 hours
Battery	500KVAR	12 hours
Total Power	1.1MVA	

Source of Data: Technical Department of Naval Base, Cape Formoso Island in Brass Local Government Area, Bayelsa State, Nigeria

Using the particle Swarm Optimisation algorithm and the Python programming language, the following data (conditions) were analysed taking into account the power balance equality. The power balance equality is such that;

$$\sum_{i=1}^{n} P_{gi} = P_D \quad [3]$$

Where,

P_{gi} = active power output of the ith generator,
P_D = Load demand,
n = total number of generators

The following loads are considered:

1) ***Critical load***: Because these loads cannot be shedded, they are given the highest priority. It was always anticipated that these loads will have power.
2) ***Semi-critical load***: These loads are prioritised over non-critical loads even though they are not as important as critical loads.
3) ***Non-critical loads:*** These are the loads that are shedded the most. It was anticipated that there will be more blackouts.

D. Power World Model of the Microgrid

The microgrid was modelled using the Power World Simulator software package. Three generation sources were used in the system: a micro-turbine (which replaces the battery storage system), a solar PV array, and a wind turbine. As seen below, the loads were divided into critical, semi-critical and non-critical loads.

By utilizing the PSO algorithm in the Python programming language to implement the optimized load shedding scheme for the aforementioned microgrid, which consists of critical loads, semi-critical loads, and non-critical loads as shown in Fig. 2, the following outcomes were attained.

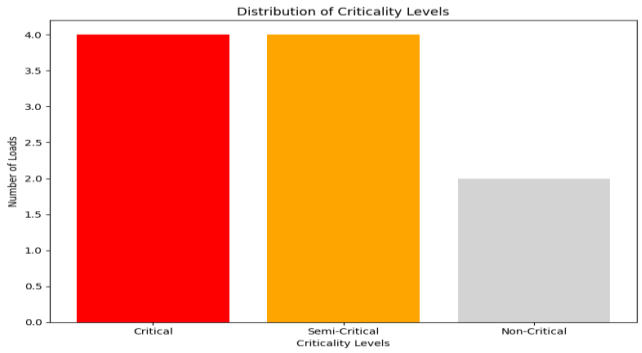

Fig.2 Critical, semi-critical and not-critical load buses plot

E. Optimized Load shedding Scheme

A plot of the microgrid's load shedding strategy for each of the ten buses is displayed in Fig.3 below. The number of buses in the microgrid is represented by the x-axis, and the y-axis shows the system's percentage levels of shedded load

The optimized load shedding scheme in Fig. 3 illustrates how other buses in the microgrid were shedded according to their critical level and the microgrid's power availability.

Fig. 3 Optimized load shedding scheme of the microgrid for the ten buses

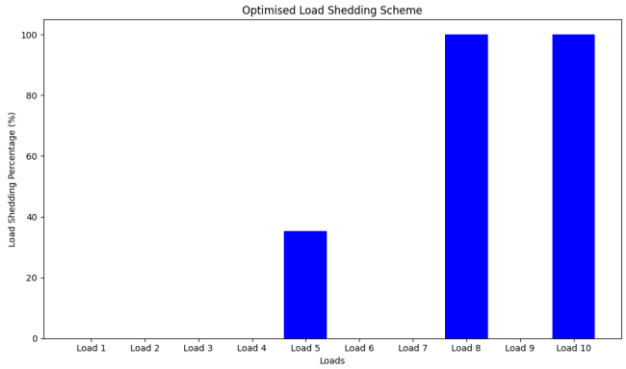

III. RESULTS AND DISCUSSION

The microgrid was modelled using the Power World Simulator tool. Three generation sources were used in the system: a micro-turbine (which replaces the battery storage system), a solar PV

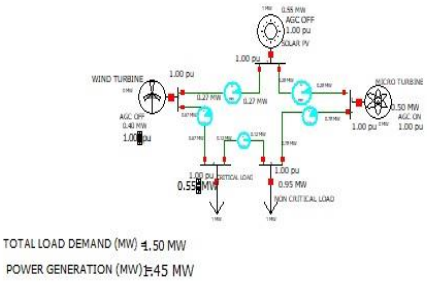

array, and a wind turbine. As seen in Fig. 4 and Fig. 5, the loads are divided into critical, semi-critical and non-critical loads.

Fig. 4 Power flow Of Cape Formoso microdgrid model showing the flow of power from the generation sources to the loads.

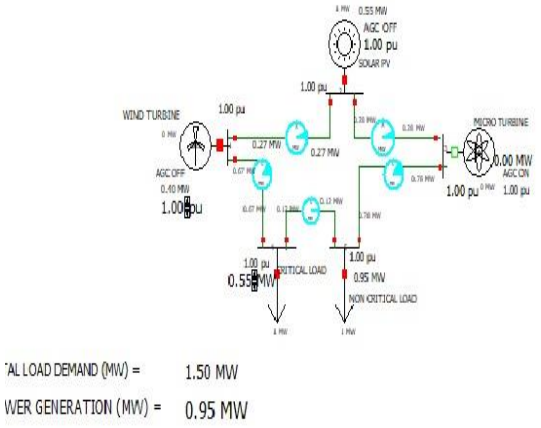

Fig. 5 Power flow of the microgrid during the day (wind turbine and solar pv sources).

Fig. 6 through Fig. 8 depict the system's transient performance when only the critical loads were powered ON and the other load buses were completely deactivated. Since only the critical loads, which accounted for 550kW of the 1.1MW of generated power were being served, it was evident that the power generated was not being used efficiently. Also, there were significant real power losses, nearly equal to the power consumed. Since all non-critical loads were shedded, there was a significant amount of load shedding.

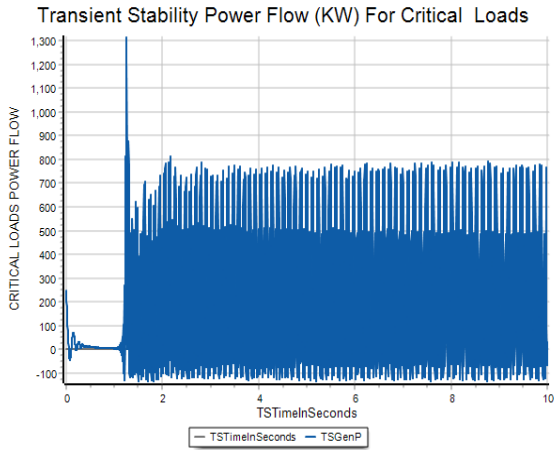

Fig. .6 Power flow from generators to the microgrid before the optimised load shedding scheme

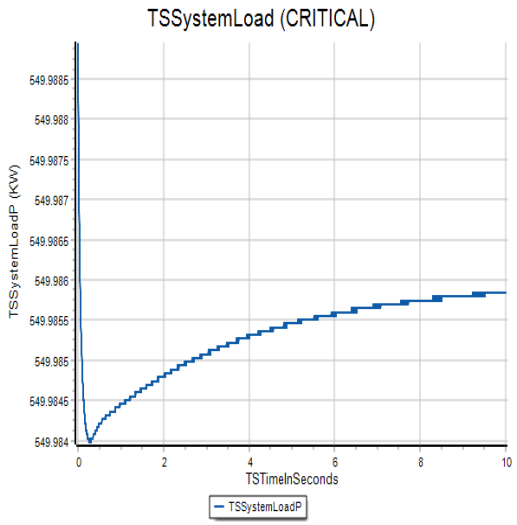

Fig. 7 Transient stability of load profile of the critical loads.

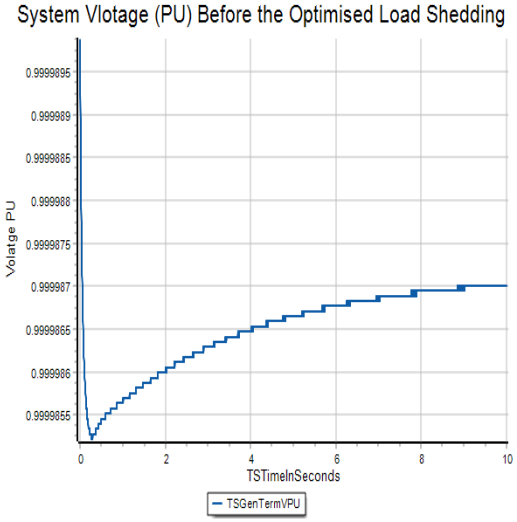

Fig. 8 System voltage before the optimised load shedding scheme

The microgrid's transient performance results following the optimised load shedding scheme are shown in Fig. 9 through Fig. 11. Upon examination, it was evident that the 1.1MW of generated power was utilised to its best advantage by minimizing the number of loads shedded (just three buses were shedded), which did not impact the critical load buses, and by minimizing real power losses, which resulted in a reduction of power losses to approximately 50KW. It was also seen that there was percentage performance improvement of the microgrid system from 40% to 70% after the optimization process.

According to the system's transient stability analysis, the PSO algorithm's optimal load shedding plan appeared to be successful in maintaining and securing the system's stability, which supported the system's efficient operation.

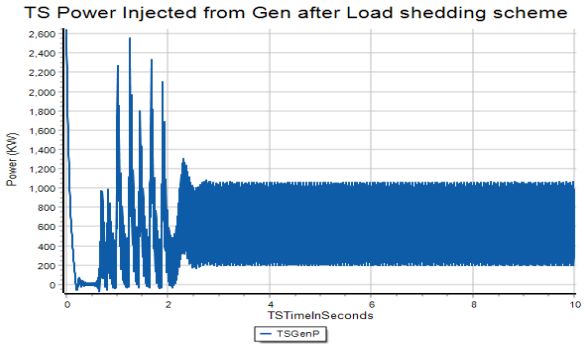

Fig. 9 Power flow from generators to the microgrid after the optimised load shedding scheme.

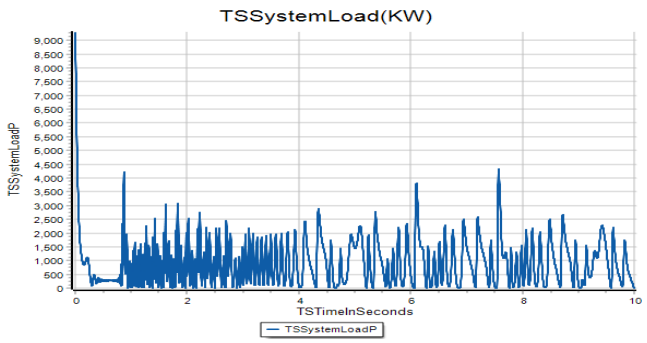

Fig. 10 Load signal of the optimised load shedding in the microgrid system

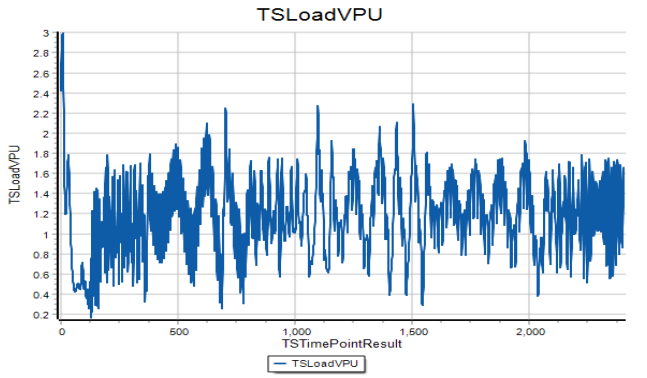

Fig. 11 Voltage profile (Pu) of the microgrid after the optimised load shedding scheme

Fig. 12 illustrates what happens when a system blackout occurred because the load demand exceeded the maximum capacity of the power sources.

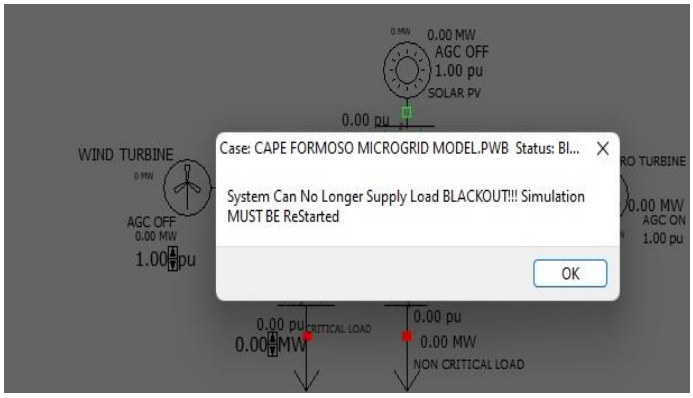

Fig. 12 System blackout as a result of trying to give power to all load

IV.CONCLUSION

The application of swarm intelligence algorithms, notably particle swarm optimization (PSO), for optimizing power flow in microgrids has shown remarkable promise in addressing congestion management challenges. Through the utilization of PSO, the complex task of balancing power generation and consumption within microgrids has been effectively tackled, mitigating congestion issues and enhancing overall system efficiency.

The implementation of PSO algorithms has demonstrated their ability to efficiently search and identify optimal solutions in real-time, thereby aiding in the minimization of power losses, voltage deviations, and alleviation of congestion hotspots. The adaptability and self-organizing nature of swarm intelligence techniques have provided robustness in managing varying load demands and integrating renewable energy sources seamlessly.

Moreover, the utilization of PSO for power flow optimization in microgrids has showcased its potential to enhance the reliability and stability of the grid, facilitating the integration of diverse energy resources, while ensuring a consistent and uninterrupted power supply.

REFERENCES

Joorabian, M., & Saniei, M. (2011). *Optimal locating and sizing of TCPST for Congestion management in Deregulated Electricity markets.* Paper presented at the UPEC, 46th International Universities' Power Engineering Conference. .

Kennedy, J., & Eberhart, R. (1995). *Particle swarm optimization.* Paper presented at the Proceedings of ICNN'95

Kumar, S. S., & Subbaraj, S. (2016). A hybrid particle swarm optimization-ant colony optimization algorithm for microgrid power management. *Energy, 117*, 669-678.

Li, W., Mu, X., Yang, Y., & Li, Y. (2020). Combined energy storage and demand response management for congestion alleviation in microgrids. *Applied Energy, 263*(114640).

Mogaka, L. O., Nyakoe, G. N., & Saulo, M. J. (2020). Islanded microgrid congestion control by load prioritization and shedding using ABC algorithm.

International Journal of Electrical and Computer Engineering (IJECE), 10(5), 4552-4561.

Nadali, N., Ehsan, H. F., Miadreza, S., Tapan, S., Golshan, H., Esmail, M., & Pierluigi, S. (2017). A bottom-up approach for demand response aggregators' participation in electricity markets. *Electric Power Systems Research, 143*, 121-129.

Raja, S. C., Venkatesh , P., & Manikandan, B. V. (2011). *Transmission Congestion Management in restructured power systems*. Paper presented at the 2011 International Conference on Emerging Trends in Electrical and Computer Technology, Nagercoil, India, India.

Sarwar, M. D., & Siddiqui, A. S. (2015). An efficient particle swarm optimizer for congestion management in deregulated electricity market. . *Journal of Electrical System and Information Technology, 2*, 269-282.

Sayed, F., & Kamel, S. (2017). *Optimal load shedding for voltage collapse prevention using improved harmony search algorithm*. Paper presented at the 2017 Nineteenth International Middle East Power Systems Conference (MEPCON), Cairo, Egypt: , Egypt.

Tan, Y. (2016). *GPU-based Parallel Implementation of Swarm Intelligence Algorithms*. Amsterdam: Morgan Kaufmann,.

Wang, Y., Luo, X., & Liu, X. (2020). Dynamic pricing-based demand response design for the economic benefit of microgrids with energy storage systems. . *Applied Energy, 279*(115952).

Xu, H. Q., Gu, S., Fan, Y. C., Li, X. S., Zhao, Y. F., Zhao, J., & Wang, J. J. (2023). A strategy learning framework for particle swarm optimization algorithm,. *Information Sciences, 619*, 126-152.

Yeongho, C., Yujin, L., & Hak-Man, K. (2017). Optimal load shedding for maximizing satisfaction in an islanded microgrid. . *Energies, 10*(45), 1-13.

Journal of Engineering, Emerging Technologies and Applied Sciences -– Volume 1 Issue 2, Nov. 2023

Available at ***https://www.ndu.edu.ng/journalofengineering/***

RESEARCH ARTICLE OPEN ACCESS

Determination of Carbon Dioxide (CO_2) Emissions from Perkins P220-3 AGO-Based Generating Plant in Variable Temperature and Relative Humidity

Sakwe Adianimovie

Department of Chemical Engineering, Federal University Otuoke, Bayelsa State, Nigeria

sakwea@fuotuoke.edu.ng

----------**********----------

Abstract:

The main aim of this research is for the determination of Carbon-dioxide (CO_2) concentration level emitted from PERKINS P220-3 AGO-based generating plant using Series 500 Portable Air Quality Monitor with varying temperature and relative humidity. The generating plant services the facilities in the Faculty of Engineering, Federal University Otuoke (FUO), Bayelsa State. The air sampling was done for a consecutive period of twenty-one working days in the month of July, 2023. This was to ascertain the health risk that could possibly emanate from the emissions of CO_2 into the environment on the safety of personnel exposed daily to those facilities. The results were compared to "The American Society of Heating, Refrigeration and Air Conditioning Engineers (ASHRAE)" and "Occupational Safety and Health Administration (OSHA)" as <1,000 ppm limit or no severe health effect. The results showed that CO_2 have total average concentration of 898.23 ppm, total average temperature at 29.7^oC and total average relative humidity at 85.81%. The overall average results showed that the CO_2 concentration emissions level were below the WHO ambient allowable limits of not more than 1000 ppm in 8 hours average.

Keywords — **Environment, CO2 concentration, Emissions Level, AGO-Based, Sampling and Monitoring, Generating Plants, Facilities, Faculty of Engineering, Temperature, Relative Humidity, Air Quality**

----------**********----------

I. INTRODUCTION

The necessity for an efficient, clean and environmentally friendly condition of an improved ambient air quality (AAQ) can never be over emphasized, owing to various methods of wasteful discharges that generate from human activities that pollute the environment, which produces particulate matter and greenhouse gases that causes global climate change (Pachauri et al., 2007, IPCC, 2013). These particulate matter and gases in excess are poisonous to human health. Some of their sources are from human nonferrous activities such as gas flaring (Etienne Romsom and Kathryn McPhail 2021), part of transportation sector (Farooq et al., (2021), wood fire (Sakwe Adianimovie and Gbeinzi Ebinimi, 2023) and others which includes electricity power generation especially on gas turbines (Olugboji and Adepoju in 2018) as gas-base fuel, power plants (Smith et al,. 2018) as well as from diesel fuel commonly called automotive gas oil (AGO). However, the effect of carbon-dioxide (CO2) emissions is from various fuel blends of AGO-based (Hossain et al., 2020).

Gaseous pollutants thrive better with respect to humidity and temperature, as all living things survive effectively in the presence of humidity in air (Peter, 2005). Naturally, pollutant concentrations depend on the temperature and humidity of the environment, this is because relative humidity contributes to the absorption of moisture during storage of materials. Similarly, relative humidity also contributes to the regulation of the body temperature in ensuring good perspiration, it is the

total amount of water vapor present in a given volume of air at the same temperature which also relates to the emissions of CO2 in AGO-based generating plant.

AGO-based fuel employed in running power plants is on main source of carbon-dioxide (CO_2) emissions worldwide. The use of automotive gas oil (AGO) from fossil fuel-based power plants results in substantial emissions of CO_2, which are part of the contributing factors in global warming (Bilichi, 2018). An accurate determination of the amount of CO_2 emitted per unit of energy generated from these plants help to quantify the environmental impact and identify areas for improvement which can give a precise and economically viable result (Feng et al., 2019), and data-driven methodology (Zhang et al., 2019). Though, estimated CO_2 emissions from AGO-based power plants could significantly differ in different locations (Nizamuddin et al., 2020), yet there is need to increase energy efficiency and lower CO_2 emissions especially in developing nations (Yara et al., 2019), in improving air quality (Ede P.N. and Edokpa, D.O. 2015). This actually shows that high amount of CO_2 emissions is also a result of the producing facilities based on automotive gas oil AGO (Bilici, 2018). Understanding the CO_2 emissions from these power plants, which primarily burn AGO-based fuel, is very essential for efficient environmental management and energy efficiency (Smith 2021, IEA, 2016).

AGO-based fuel plants emits significant amounts of carbon-dioxide as used daily in various industries, factories, real estates, businesses and most tertiary institutions in Nigeria including the Engineering faculty of the Federal University, Otuoke, Bayelsa State. Therefore, this study focused on the PERKINS P220-3 AGO-based power plant at the Faculty of Engineering, Federal University Otuoke, where measurements and estimation of CO_2 emissions with respect to temperature and relative humidity variation was done and results compared to the outdoor CO_2 emissions with (ASHRAE)" and (OSHA)" as < 1,000 ppm limit or no severe health effect as well as WHO CO_2 allowable limits of not more than 1000 ppm in 8 hours average (WHO, 2021).

II. MATERIALS AND METHODS

A. Study Area Description

This research took place in the main/administrative premises of the Faculty of Engineering, Federal University Otuoke, West Campus. The Federal University, Otuoke, is a Nigeria Federal Government-owned University, located in Otuoke in Ogbia Local Government Area of Bayelsa State, Southern Nigeria in the Niger Delta Region as presented in Figure 1. The institution is located about 27 kilometers south of Yenagoa, the Bayelsa State Capital, which is 100 kilometers West of Port Harcourt, Rivers State. The faculty and area in view consists of three major block buildings of one story each vis-à-vis Block A, Block B and Block C and a mini lecture theatre building adjacent to Blocks B and C but directly opposite Block A. These blocks consist of the Dean's office, the central Engineering Conference room, and the Head of Department (HOD) offices for the five departments (Chemical, Civic, Electrical, Mechanical/Mechatronics and Petroleum Engineering), Staff offices, faculty's Library, the National Union of Engineering Student Association (NUESA) office, Laboratories and classrooms. The sampling and monitoring was carried out from Monday through Friday between the hours of 8:00 a.m. and 4:00 p.m. daily for a total of 7 hours per day.

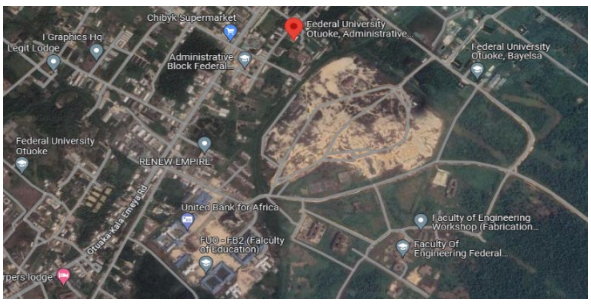

Figure 1: Sampling Location: Source (Ogunlowo O.O and Sakwe, A 2023)

B. Sampling Equipment

The main equipment used for the sampling was the Series 500 Portable Air Quality Monitor. With its special sensor head structure, the series 500 portable air quality monitor allows air quality suitable with interchangeable sensor heads that can measure up to 16 distinct pollutants appropriate for usage on a variety of applications, such as short-term fixed monitoring, personal exposure monitoring, and wide-area air quality surveys. It samples particulate matter ($PM_{2.5}$, PM_{10}, PM_1, TSP), and gaseous pollutants such as CO, CO_2, NO_2, VOC, O_3, SO_2, H_2S etc.

C. PERKINS P220-3 AGO-Based Generating Plant

Table 1: Major parameters of the Perkins P220-3 AGO-Based Generating Plant

S/No	Parameters	Specifications
1	Model	9011
2	Prime Power (kW)	160.0
3	Standby Power (kW)	176.0
4	Standby Power (kVA)	220
5	Noise	@ 7mt
6	Run Time	11 hours @ 75% load
7	Warranty	1 year
8	Dry Weight (KG)	1708
9	Phase	3
10	Fuel Type	Diesel

D. Automotive Gas Oil (AGO)/ Diesel

The diesel which was used for the running of the power plant throughout the sampling period was received from the direct distribution outlet of the Nigeria National Petroleum Cooperation (NNPC) Bayelsa State and must have met the standard requirement quality assurance product specification by the NNPC/DPR (Department of Petroleum Resources) as presented in Table 2

Table 2: NNPC/DPR standard requirement quality assurance product specification

S/No	Parameters	Units
1	Density:	8.45-8.60 g/ml
2	Viscosity (at 40°C):	4.5-4.6
3	Flash Point:	74-800C
4	Octane Number:	47-52
5	Sulphur Content:	0.0516
6	Water Content:	Nil
7	Colour:	Pale Yellow
8	Appearance:	Clear and Bright

Source: (ENX Energy and Chemicals Nig. Ltd, 2023).

E. Relative Humidity and Temperature

The measurement of relative humidity and temperature was done by taking the daily average recordings directly gotten from the results of the Bayelsa State daily weather forecast (Yenagoa, Bayelsa, Nigeria Weather 2023).

F. Methods

The Series 500 Portable Air Quality Monitor was placed on the top of the PERKINS P220-3 Generating Power Plant, closed to the exhaust/waste outlet attached with the CO2 sensor placed one meter (100 cm) away from the discharge pipe. The readings were recorded by the portable air quality monitor at 30 minutes interval for 7 hours daily for a period of 21 working days. This continues monitoring and measurement took place from 9:00 am to 4:00 pm for five days in a week (Monday to Friday) throughout the month of July, 2023. The power plant was allowed to run for a minimum of 45 minutes to enable stability at its maximum load before monitoring was done.

III. RESULTS AND DISCUSSION

The monitoring was done for 7 hours per day from 9:00 am to 4:00 pm in 30 minutes interval. Readings were taken and the average results were calculated as presented in Table 3.0 below. The computed results were compare with the ASHRAE and OSHA daily outdoor CO_2 emissions standard guidelines to ascertain the safety conditions and health risk of those daily exposed to the facilities of the Faculty of Engineering, Federal University Otuoke.

Figure 2 shows the pattern of daily carbon-dioxide release from the AGO-based power generating machine, while Figure 3 shows the daily percentage concentration of CO_2 emission respectively.

The results of the 21 days monitoring indicated that CO_2 concentration was highest on the 3rd and 16th days at 1015 ppm and 1002 ppm respectively, which occurred on the 5th and 24th of July, 2023. The temperature and relative humidity for the 3rd day were 27°C and 95.60 %, while that of the 16th day were 27°C and 94.80% respectively.

These were the only two days that the results exceeded the ASHRAE and OSHA as < 1,000 ppm limit or no severe health effect. The lowest readings of CO_2 concentration was 770 ppm and 773 ppm at temperatures of 36°C and 31°C with relative humidity of 75.90 % and 82.20 % respectively. This occurred at day 10 and day 5 been the 14th and 7th of July, 2023.

However, 19 days results showed that CO_2 concentration was below the ASHRAE and OSHA recommended limits of < 1,000 ppm limit or no severe health effect. Percentage wise, it was discovered that 90.5 % of the samples were below the recommended limits, while 9.5 % of samples were above the ASHRAE and OSHA limits.

Similarly, Figure 3 showed that 16 days out of the 21 days sampling and monitoring indicated 5 % of CO_2 emission while 5 days had 4 % equal distributions, though there were clear daily variations in figures on CO_2 concentration level as shown in Table 3 and Figure 3 respectively.

Table 3: Daily Average reading of CO2 at Varying Temperature and Relative Humidity at Constant Time Intervals

No. of Days	Dates (July, 2023)	CO_2 (Ppm)	Temp (°C)	Relative Humidity (%)	Time (Hrs)
1	3	950	30	85.30	7
2	4	988	29	83.60	7
3	5	1015	27	95.60	7
4	6	908	30	85.80	7
5	7	773	31	82.20	7
6	10	880	30	84.90	7
7	11	870	30	85.05	7
8	12	890	29	87.60	7
9	13	900	29	88.90	7
10	14	770	36	75.90	7
11	17	986	30	84.10	7
12	18	997	30	83.70	7
13	19	775	30	84.60	7
14	20	787	29	89.98	7
15	21	968	30	85.86	7
16	24	1002	27	94.80	7
17	25	898	30	85.00	7
18	26	907	29	85.85	7
19	27	909	29	82.90	7
20	18	800	29	85.20	7
21	21	890	30	85.08	7
Total Average		898.23	29.7	85.06	7

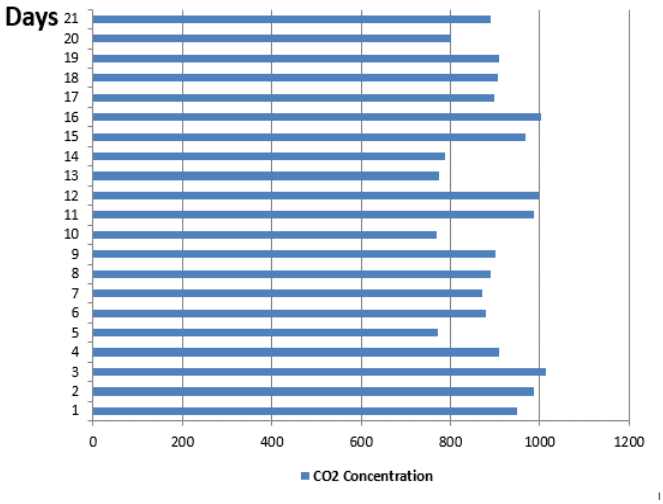

Figure 2: Daily Concentration of CO_2 Emissions

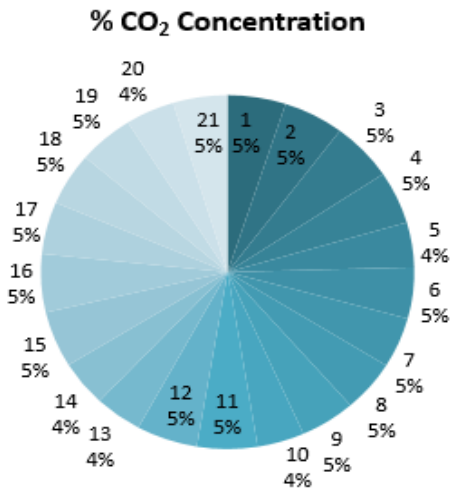

Figure 3: Daily Percentage Concentration of CO_2 Emissions

Four (4) days showed the lowest CO_2 concentration level during the sampling period which ranged between 770 ppm to 800 ppm at relatively high temperatures but low relative humidity Table 3. Furthermore, from all indications the results of the sampling showed that CO_2 concentrations vary with respect to temperature and relative humidity. That is, at higher temperature, relative humidity was low as well as CO_2 concentrations. While at lower temperature, CO_2 concentration was high as well as relative humidity (Table 3 and Figure 3).

On the overall average, CO_2 concentration level recorded was 898.23 ppm, temperature at 29.7°C and relative humidity at 85.81%. The overall average results showed that the PERKINS P220-3 AGO-based generating plant released CO_2 that was below the ASHRAE and OSHA limits of < 1,000 ppm limit or no severe health effect, indicating that personal exposure to the environment under investigation was safe and free from any health risk on the bases of CO_2 emission. However, other metrological parameters were not taken into consideration during the 21 days sampling and motoring period using the Series 500 Portable Air Quality Monitor.

.

IV. CONCLUSION

Efficient, liveable, sustainable, and environmentally friendly conditions of an improved ambient air quality (AAQ) is of serious concern. No doubts, humans are adversely contributing to the poor air quality in the environment and has really become an overbearing issue. These activities are from different sources such as bush burning, gas flaring, and the use of power generating plants etc. which have increased the release of greenhouse gases including Carbon dioxide (CO_2). The release of Carbon-dioxide into the atmosphere has led to several issues including climate change and global warming. In this study, CO_2 was sampled and monitored in the month of July, 2023 for 21 working days consecutively using the Series 500 Portable Air Quality Monitor in the facilities of the Faculty of Engineering, Federal University, Otuoke powered by PERKINS P220-3 AGO-based generating plant. The sampling was done with varying temperatures and relative humidity, though other metrological parameters were not under consideration. The investigation showed that personal exposure to the facilities are safe and free from Carbon-dioxide based health risks. This was because 90.5 % of CO_2 emissions were below the ASHRAE and OSHA limits of < 1,000 ppm limit or no severe health effect,

as compared to the 9.5% that was above the standards.

While the results in this study indicated low release of Carbon-dioxide into the atmosphere, other air pollutants like $PM_{2.5}$, PM_{10}, PM_1, TSP, and gaseous pollutants such as CO, NO_2, VOC, O_3, SO_2, H_2S etc which are also constituents of AGO-based fuel, were not analyzed. Therefore, to be certain of the overall safety of those who accesses the facility, it is recommended that further studies should be carried out to expand the scope on the power plant.

ACKNOWLEDGMENT

The author does acknowledge Otong Daniel in the Department of Chemical Engineering, Faculty of Engineering, Federal University Otuoke (FUO), Bayelsa State on his project work.

REFERENCES

Bilici, M. (2018). Environmental impacts of electricity production from fossil fuels. Renewable and Sustainable Energy Reviews, 81(1), 2148-2157. doi: 10.1016/j.rser.2017.06.031

Ede, P.N. and Edokpa, D.O. (2015) Regional Ai Quality of the Nigeria's Niger Delta. OpenJournal of Air Pollution, 4, 7-15. https://doi.org/10.4236/ojap.2015.41002.

ENXEnergy and Chemicals Nigeria Limited. Published February 16,2023

Etienne Romsom and Kathryn McPhail 2021. Capturing economic and social value from hydrocarbon gas flaring and venting: solutions and actions.

Farooq, M. A., Ali, M., & Ahmad, S. (2021). Simulation-based estimation of CO2 emissions from automobile gas oil (AGO) based power plants in Pakistan. Environmental Science and Pollution Research, 28(14), 17613-17622.

Hossain, M. A., Islam, M. A., & Al-Mamun, M. R. (2020). CO_2 emissions from automobile gas oil-based power plants in Bangladesh: Impact of fuel blends. Journal of Cleaner Production, 246, 119019.

Intergovernmental Panel on Climate Change. (2006). IPCC Guidelines for National Greenhouse Gas Inventories (Vol. 5). https://www.ipcc-nggip.iges.or.jp/public/2006gl/vol5.html

International Energy Agency 2016a Energy and Air Pollution. World Energy Outlook Special Report (Paris, France) International Energy Agency 2016b World Energy Outlook 2016 (Paris, France)

Nizamuddin, M., Soroush, A., Levresse, G., & El-Zein, A. (2020). Performance analysis and environmental impact of a diesel power plant in developing countries: Case study of Lebanon. Environmental Science and Pollution Research, 27(10), 10021-10030.

OGUNLOWO, OO and SAKWE, A. Evaluation of Lead and Iron Content in Different Stages of Water Treatment Facilities within Otuoke and Yenagoa Metropolis, Bayelsa State, Nigeria. J. Appl. Sci. Environ. Manage. Vol. 27 (11) 2415-2420 November 2023

Olugboji, O. A., & Adepoju, A. A. (2018). Economic and environmental evaluation of gas turbine power plant: The case of Nigeria. Energy Reports, 4, 690-696.

Pachauri, R K., and Babu Jallow. "Climate Change 2007: The Physical ScienceBasis." Graphics, Presentations, and Speeches. 2007.

Peter Apert 2005. Integrative and Comparative Biology, Volume 45, Issue 5, November 2005, Pages 683–684, https://doi.org/10.1093/icb/45.5.683.

Sakwe Adianimovie and Gbeinzi Ebinimi. Investigation of Particulate Matter (PM10 & PM2.5) and Gaseous Pollutants (CO2 & CO) in Houses Using Kerosene Cooking Stoves & Wood Fire in Attisa 3, Bayelsa State, Nigeria

Smith, A., Johnson, B., & Thompson, C. (2018). Assessing CO2 emissions from AGO-based generating plants: An analysis of plant efficiency, fuel composition, and operational practices. Environmental Studies, 45(3), 123-145.

Smith, A., Johnson, B., & Thompson, C. (2018). Assessing CO2 emissions from AGO-based generating plants: An analysis of plant efficiency, fuel composition, and operational practices. Environmental Studies, 45(3), 123-145.

Smith, J. (2021). The environmental impact of various businesses. Journal of Environmental Studies, 45(3), 56-78. https://doi.org/10.1080/123456789.2021.1234567

www.co2Meter.com/blogs/news/8487325.Measuring-Carbon-dioxide in-outdoor-air. October 5, 2022.. Access: 2nd December, 2023.

www.osha.gov/dts/chemicalsampling/data/CH_225400.html Access: 2nd December, 2023

www.who.int/news-room/feature-stories/detail/what-are-the-who-air-quality-guideline 2021. Access: 2nd December, 2023

Yenagoa, Bayelsa, Nigeria Monthly Weather | AccuWeather. 2023 - https://www.accuweather.com/en/ng/yenagoa/252198/july-weather/252198. Access: 5th December, 2023

Zhang, W., Li, C., Liu, X., & Wang, J. (2019). Data-driven estimation of CO2 emissions from automobile diesel oil (ADO) and automobile gas oil (AGO) based power plants in China. Journal of Cleaner Production, 229, 561-571.

Journal of Engineering, Emerging Technologies and Applied Sciences -– Volume 1 Issue 2, Nov. 2023

Available at ***https://www.ndu.edu.ng/journalofengineering/***

RESEARCH ARTICLE OPEN ACCESS

Analysis of Electromagnetic Wave Propagation in Human Tissue

Godday Biowei*, Sulaiman A. Adekola**, Ayibapreye K. Benjamin*

*Electrical and Electronic Engineering, Niger Delta University, Nigeria

Email: biogod@ndu.edu.ng

**Department of Electrical and Electronic Engineering, Federal University Otuoke, Nigeria

----------**********----------

Abstract:

This paper reports the analysis of EM wave propagation in human tissue, with specific reference to radio-frequency wave propagation. Maxwell's equation is applied to analyse and model the behaviour of the EM wave as it transits from the free-space as a source-free region into human tissue. Maxwell's equations have never been used in this manner before. The transmitted wave is theoretically followed into the human skin. Measured electric fields from GSM towers and frequencies used by the four major wireless service providers in Nigeria, coupled with the modelled equation for the transmitted wave in the skin are used to simulate the wave propagation in the tissue. MATLAB software, a versatile engineering tool is used to simulate the propagation model in human tissue. Measurement of the EM wave radiated by some sources into free-space is carried out. Results obtained from computation using the developed propagation model in human tissue are compared with standards and existing results. Results show that the EM wave radiating around our immediate environment and hitting our skin does not travel deep into our body. The frequencies used by these GSM network providers for 3G and 4G transmission are low and do not possess enough energy to cause damage to the tissue.

Keywords — **Analysis, Electromagnetic, Wave Propagation, Human Tissue**

----------**********----------

I. INTRODUCTION

One of the world's fastest-growing technologies, mobile phone technology, has become a popular and essential part of our daily lives. Significant improvements in internet data transmission speed and quality have been achieved as a result of technological advancement, as have modern communications such as Wi-Fi, UMTS (Universal Mobile Telecommunications System), EDGE (Enhanced Data Rates for GSM Evolution), WiMAX (Worldwide Interoperability for Microwave Access), and 4G have been developed. It is now a common sight to see wireless base stations (BS) in residential areas radiating radio frequency (RF) waves.

RF wave is part of the electromagnetic (EM) wave spectrum which is produced by a variety of electrical systems, including mobile phones, microwave ovens, communication base stations, high-voltage power lines, electronic instruments and electromagnetic equipment. EM devices generate a variety of electromagnetic waves of varying frequencies, resulting in an increase in EM radiation in human living areas. This has led to increased health concerns about the RF-EM radiation emission from GSM towers by the general public who consider this as environmental pollution. The EM wave spectrum is divided into two parts, the non-ionizing and ionizing radiation. RF wave used for wireless communications belong to the non-ionizing radiation, which radiates with

frequencies that have low photon energy. Photon energy of this magnitude is incapable of causing any permanent damage to the human tissue. The energy is too low any form of ionization, that is break chemical bonds.

(Gabriel et al, 1986) studied the effect of various frequencies on the permittivity (ε) and conductivity (σ) of the human tissue and results showed that the permittivity decreases and the conductivity increases when the frequency of a wave hitting the skin increases.

The four major GSM providers in Nigeria, which are Glo Ng., MTN Ng., Airtel Ng., and 9Mobile, use the same frequency band 1(2100MHz), which has bandwidth of between (2110-2170) MHz for 3G network transmissions. For 4G network transmissions, Glo Ng. uses the band 28(700MHz), which has a bandwidth of between (758-803) MHz and band 3(1800MHz) having a bandwidth of between (1805-1880) MHz. MTN Ng., uses band 7(2600MHz) having a bandwidth of between (2620-2690) MHz, band 20(800MHz) having a bandwidth of between (721-821) MHz and band 42(3500MHz) having a bandwidth of between (3400-3600) MHz for the 4G network transmissions. Airtel NG. and 9Mobile NG. both use band B3(1800MHz) for 4G network transmissions. The lower or higher frequencies of these frequency bands may be use to simulate the EM propagation in human tissue.

II. BACKGROUND THEORY

The electrical characteristics of the tissue must be understood in order to investigate how EM field radiation affects biological tissue (A. Lewandovski, A. Szyplowska, M. Kafarski A. Wilczek, P. Barmuta and W. Skierucha, 2017) (W. Skierucha and A. Wilczek, 2010). The biological effects that are created when biological tissue is exposed to EM wave radiation rely on the electrical characteristics of the tissue (Alabaster, 2003). Relative permittivity (ε_r), conductivity (σ) and charge density (ρ) are three electrical properties that are typically used to describe electrical materials. Most living organisms are made up of huge number of cells of varying electromagnetic properties (J. Chung and J. Shim, 2020) (J. Behari, Z. H. Zaidi and Z. C. Alex, 1994). The most important aspect of studying the biological effects of EM field radiation on biological tissues is the characteristics they possess when subjected radiation from EM wave of different frequencies.

The electrical properties of every material medium distinctly divide them into two categories: conductors and insulators (dielectrics) (R. Ramirez-Vazquez, E. Arribas. Thielens and I. Escober, A., 2020). When an electric field is applied, materials with conductive properties have charges that can move about freely (M. D. Devine and R. G. Vaughan , 2007). While in the case of insulators (dielectrics), charges are fixed, never free to move, when an electric field is applied. In some materials, however, their molecules have negative and positive charges that do not line up. As a result, the material develops an electric dipole moment. By positioning the dipoles, an applied field produces an opposite field in the dielectric. The majority of materials are distinguished by having a mixture of free charges and orientable dipoles, which reduces the induced electric field relative to applied electric field in free space (H. Nikawa, H. Yamashiro, T. Hamada, H. Kumagai,, 1999). An induced electric field in an insulator is substantially smaller than the electric field applied, whereas in the instance of a good conductor, it is practically non-existent. The relative permittivity ε of these materials is what causes their induced electric field to be reduced.

The human tissue possesses characteristics of both an insulator and a conductor. This is because it possesses charges with restricted movement as well as dipoles. The heterogeneous nature of the human tissue may cause charges to be trapped at an interface. Whenever an electric field is applied to human tissue, negative and positive ions tend to travel in opposite directions. This causes a charge separation that behaves like a large dipole because internal polarization is produced. Thus, the human tissue may be described as a material having relative permittivity ε_r and conductivity σ . Electrical permittivity of a material characterizes its ability to store charge particles and/ or rotate

molecular dipole while its ability to transport charge particles is conductivity.

The relative permittivity governs how fast a wave propagates in human tissue. For a homogeneous medium such as free-space, the relative permittivity is unity, giving the value of permittivity as $\varepsilon_0\,(8.85\times10^{-12}F/m)$. Whilst conduction current doesn't change at all in free space the displacement current does increase with frequency due to the constant electrical characteristics (ε_r and σ). Homogeneous medium like free-space behaves like a conductor to a low frequency EM field but appears capacitive at high frequencies. Inhomogeneous or non-homogenous material like the human tissue, however, does not have constant electrical properties. An inhomogeneous material's electrical properties depend on the frequency of the induced EM field (M. Ziane, R. Sauleau, and M. Zhadobov.). This dependency of electrical properties of the human tissue on frequency of propagating field makes it dispersive (B. Julian, D. Andrea, F. Iman, F. Lourdes, C. V. Sammut, 2020). Therefore, conductivity σ^* and permittivity ε^* are dependent on the applied electric field's frequency and this dependency is referred to as dispersion. The human tissue displays several different dispersions over a wide frequency range (D. Yinliang, E. A. Rashed and A. Hirata., 2020). Thus, dispersion phenomenon characterizes the movement of charge carriers and dipole orientation in an inhomogeneous material.

A. Modelling of Transmitted Wave Propagation in the Human Tissue

This section concerns itself with the transmitted EM wave into the human tissue. It is therefore, imperative to investigate the properties of the human tissue in order to ascertain how the transmitted EM wave behaves inside the human tissue. It is now appropriate to consider the dynamic internal structure of Maxwell's equations in the human tissue. Having established that fields transmitted (E-and H-fields) into the human tissue are merely component parts of the EM wave that is incident on the skin from the empty-space, it is necessary to investigate how those fields propagate in the human tissue. For one thing, it is instructive to realize that the human tissue has a non-zero coefficient of conduction $(\sigma\neq0)$, although the net charge density denoted by ρ is zero as earlier pointed out in section 3.1.1. With this in mind, one can see at once that the situation of EM wave propagation in the human tissue.

B Dynamic Internal Structure of Maxwell's equations inside the Human Tissue

If the charge and current densities are non-existent, the right-hand sides of all four Maxwell's equations become zeros as described by (6) – (9), which led to oscillating wave defined by (20). Once the oscillating wave is incident on the skin, the transmitted or refracted wave enters the human tissue. Since conductivity (σ) exists inside the human tissue, the transmitted electric field $(\mathbf{E}_t)$ component of the incident EM wave engages the conductivity and couples with it. As far as the charge density ρ is concerned, the human flesh is charge-neutral. Based on the foregoing discussion, Maxwell's equations in the human tissue assume forms characterized by,

$$\nabla\cdot\mathbf{E}_t=0 \tag{1}$$

$$\nabla\times\mathbf{B}_t-\mu\varepsilon\frac{\partial\mathbf{D}_t}{\partial t}=\mu\mathbf{J} \tag{2}$$

$$\nabla\cdot\mathbf{B}_t=0 \tag{3}$$

$$\nabla\times\mathbf{E}_t+\frac{\partial\mathbf{B}_t}{\partial t}=0 \tag{4}$$

provided

$$\mathbf{J}_t=\sigma\mathbf{E}_t \tag{5}$$

where the subscript 't' stands for transmitted quantities for example, $\mathbf{E}_t$ is the electric field transmitted across the boundary.

From wave propagation viewpoint, propagation in a lossy medium is characterized by two parameters, the propagation constant β (which propels and drives the wave) and the attenuation

constant α (which acts as damper). These two parameters need to be determined for human tissue in order to accurately describe the behaviour of the transmitted wave in the human skin. This is realized as follows.

Let us re-write (2), (4) – (5) in terms of appropriate constitutive relations as

$$\nabla \times \mathbf{H}_t = \sigma \mathbf{E}_t + j\omega\varepsilon \mathbf{E}_t \quad (6)$$

$$\nabla \times \mathbf{E}_t = -j\omega\mu \mathbf{H}_t \quad (7)$$

$$\mathbf{J}_t = \sigma \mathbf{E}_t \quad (8)$$

where $e^{j\omega t}$ time variation is assumed in arriving at (6) and (7). Taking the curls of (6) and (7), one obtains

$$\nabla \times \nabla \times \mathbf{H}_t = \sigma \nabla \times \mathbf{E}_t + j\omega\varepsilon \nabla \times \mathbf{E}_t \quad (9)$$

and,

$$\nabla \times \nabla \times \mathbf{E}_t = -j\omega\mu \nabla \times \mathbf{H}_t \quad (10)$$

respectively. In Cartesian coordinates, the Laplacian of a vector $\mathbf{A}$ assumes a form given as

$$\nabla^2 \mathbf{A} = \mathbf{x}\nabla^2 A_x + \mathbf{y}\nabla^2 A_y + \mathbf{z}\nabla^2 A_z \quad (11)$$

Using the vector theorem stated in (11) concerning the curl of the curl of an arbitrary vector in (9) and (10), one arrives at the vector wave equation for the electric field as

$$\nabla^2 \mathbf{E}_t = j\omega\mu\left(\sigma + j\omega\varepsilon\right)\mathbf{E}_t = \gamma^2 \mathbf{E}_t \quad (12)$$

and the magnetic field as

$$\nabla^2 \mathbf{H}_t = j\omega\mu\left(\sigma + j\omega\varepsilon\right)\mathbf{H}_t = \gamma^2 \mathbf{H}_t \quad (13)$$

provided

$$\gamma^2 = j\omega\mu\left(\sigma + j\omega\varepsilon\right) = \left(j\omega\right)^2 \mu\left(\varepsilon + \frac{\sigma}{j\omega}\right) \quad (14)$$

is defined as the complex propagation constant, from which, one obtains

$$\gamma = j\omega\sqrt{\mu\left(\varepsilon + \frac{\sigma}{j\omega}\right)} \quad (15)$$

In terms of its real and imaginary part, γ is given as

$$\gamma = \alpha + j\beta \quad (16)$$

Equating (15) and (16) leads to

$$\alpha + j\beta = j\omega\sqrt{\mu\left(\varepsilon + \frac{\sigma}{j\omega}\right)}$$

which upon mathematical manipulations yield

$$\alpha^2 - \beta^2 + j2\alpha\beta = -\omega^2\mu\varepsilon + j\omega\mu\sigma \quad (17)$$

Equating real and imaginary parts on both sides of (17), one arrives at

$$\alpha^2 - \beta^2 = -\omega^2\mu\varepsilon \quad (18)$$

$$2\alpha\beta = \omega\mu\sigma \quad (19)$$

Equations (18) and (19) constitute two non-linear equations that are solved simultaneously for α and β to yield

$$\alpha = \frac{\omega\sqrt{\mu\varepsilon}}{2}\sqrt{\left[1 + \left(\frac{\sigma}{\omega\varepsilon}\right)^2 - 1\right]} \text{ Np/m} \quad (20)$$

as the attenuation constant while the propagation constant is determined to be

$$\beta = \frac{\omega\sqrt{\mu\varepsilon}}{2}\sqrt{\left[1 + \left(\frac{\sigma}{\omega\varepsilon}\right)^2 + 1\right]} \text{ rad/m} \quad (21)$$

Equations (20) and (21) define the attenuation and propagation constant, respectively, in terms of the conductivity, when human tissue is assumed to be lossy medium.

However, when the human tissue is considered to be conductive, meaning that the value of the loss tangent $\left(\sigma/\omega\varepsilon\right)$ in each of (20) and (21) is far greater than unity $\left(\sigma/\omega\varepsilon >> 1\right)$. Under this condition, expressions given in (20) and (21) for α and β are approximated as

$$\beta \approx \omega\sqrt{\frac{\mu\varepsilon}{2}\left(\frac{\sigma}{\omega\varepsilon} + 1\right)} = \omega\sqrt{\frac{\mu\varepsilon}{2}\left(\frac{\sigma}{\omega\varepsilon}\right)} = \omega\sqrt{\frac{\mu\sigma}{2\omega}} = \sqrt{\frac{\omega^2\mu\sigma}{2\omega}} = \sqrt{\frac{\omega\mu\sigma}{2}} \quad (22)$$

$$\alpha \approx \omega\sqrt{\frac{\mu\varepsilon}{2}\left(\frac{\sigma}{\omega\varepsilon} + 1\right)} = \omega\sqrt{\frac{\mu\varepsilon}{2}\left(\frac{\sigma}{\omega\varepsilon}\right)} = \omega\sqrt{\frac{\mu\sigma}{2\omega}} = \sqrt{\frac{\omega^2\mu\sigma}{2\omega}} = \sqrt{\frac{\omega\mu\sigma}{2}} \quad (23)$$

Therefore,

$$\alpha = \beta = \sqrt{\frac{\omega\mu\sigma}{2}} = \sqrt{\frac{2\pi f\,\mu\sigma}{2}} = \sqrt{\pi f\,\mu\sigma} \qquad (24)$$

Using the results obtained for attenuation and propagation constant along with that of the transmitted wave at the free space-skin boundary, the propagating wave in the human skin assumes this form

$$E_i(z,t) = E_0 e^{-\alpha z} e^{j(\omega t - \beta z)} = Re\{E_0 e^{-\alpha z} e^{j(\omega t - \beta z)}\}$$

$$E_i(z,t) = E_0 e^{-\alpha z} Cos(\omega t - \beta z) \qquad (25)$$

The transmitted electric field into the human skin is given as the form

$$\mathbf{E}_t(z,t) = \tau \mathrm{E}_0 e^{-\alpha z} \cos(\omega t - \beta z) \qquad (26)$$

where, τ is the transmission coefficient of the wave propagating into the medium.

where α and β are defined by (20) and (21) when human tissue is considered lossy and by (24) if the tissue is treated as a good conducting medium.

III. THE HUMAN SKIN AND ITS PROPERTIES

To determine the actual position of the tran smitted wave when it completely attenuates to zero in the human body, it is important to know the skin properties and its dimensions. This is due to the fact that the wave penetration into the human body does not go beyond the skin.

A. Electrical Properties of the Human Skin

The behaviour of a wave in a medium is determine by the electrical properties. For an inhomogeneous medium like the human tissue, wave penetration is affected by attenuation due to the presence of conductivity (σ). The human skin which is the first line of defense against external elements have three distinct electrical properties; namely: relative permittivity (ε_r), permeability (μ), and conductivity (σ), that determines if

B. Structure of the Human Skin

The skin is the largest organ of the human body, covering the whole exterior and protecting the body's internal organs from external elements. The structure of the skin is illustrated in Fig.1. This shows the three major layers of the human skin; namely: Epidermis, Dermis and Subcutaneous Fat. The epidermis is the top layer, it has a thickness band depending on the location of the body of between (0.06 – 0.1) mm. This followed by the dermis which has a thickness band of between (1.2 – 2.8) mm and finally the subcutaneous fat layer with a thickness band of between (1.1 – 5.6) mm.

The diagram of the skin here presented is used to illustrate the point with which the propagating wave will completely attenuate to zero. Thus, comparing the dimensions of the skin to the distance travelled by the EM wave when it penetrates the skin, will give a clear indication of layer of the skin the wave will completely stop travelling.

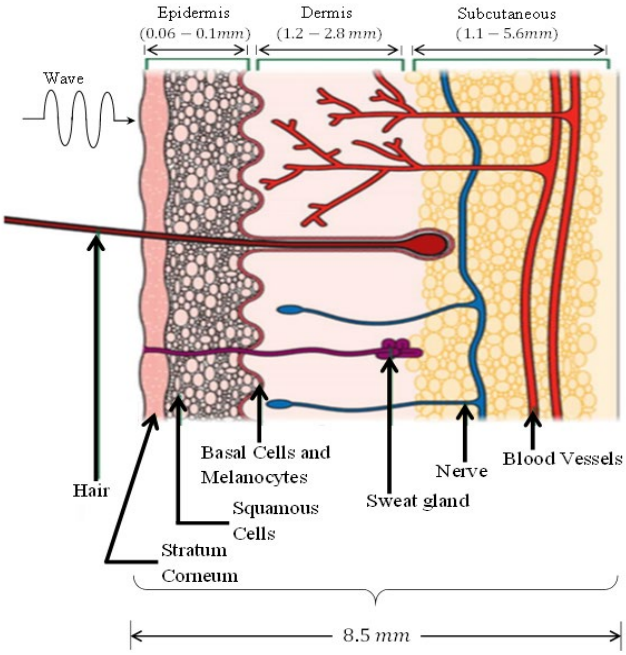

Fig. 1 Structure of the human skin

IV. RESULTS AND DISCUSSION

A. Measured Data

The field meter is pointed in the direction of the telecommunication tower, towards the source antenna. The device measures the electric field emitted by the antenna and also obtains the magnetic field and power density. It does not

capture the frequency with which the signal is transmitted.

Fig. 2 Electrosmog Meter

In Fig. 2 is the Electrosmog meter used to carry out field measurements.

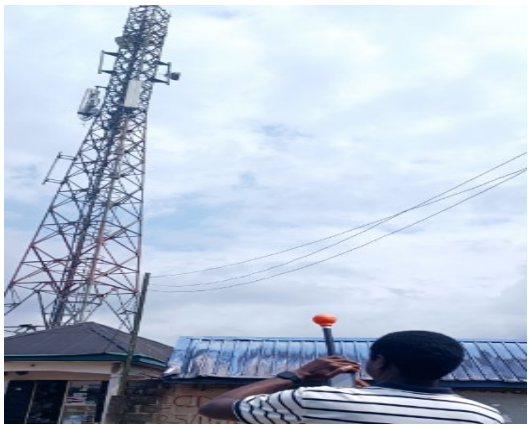

Fig. 3 Use of field meter

Fig. 3 shows a demonstration of the devices being used for the measurements carried out in this work. The meter is held out with the probe pointing in the direction of the communication tower holding the transmitting antenna. The meter receives the EM signal just like a GSM phone does and process the data, it then provides values for the electric and magnetic fields.

values for the electric fields used for simulations of the RF wave propagating into the human skin. The maximum values for network provider were used in the simulations. 7.759 V/m was used for MTN, 4.096 V/m was used for Glo, 10.68 V/m was used for Airtel and 6.847 V/m was used for 9Mobile. The time limit for each measurement was sixty seconds (60s).

B. Wave Penetration Depth in the Human Skin

Figs. 2 to 5 are the curve patterns of the EM wave propagating in the human skin. This is done for the four major network providers in Nigeria; namely: MTN, Glo, Airtel and 9Mobile. These were carried out for the frequency band between 2110MHz to 2170MHz used for downlink wireless telephony by all the network providers for 3G transmissions. In Fig.4 (a) the penetration depth of the MTN RF wave radiating into human skin is approximately 0.103 mm at a frequency 2110MHz. This is approximately 100% penetration into the epidermis of the skin and this is the same for Fig.5 (a) for Glo, Fig.4 (a) for Airtel and Fig.5 (a) for 9Mobile. Fig.1 (b) at a frequency of 2170MHz the penetration depth of MTN is approximately 0.099 mm, which is about 99% penetration into the epidermis of a maximum thickness 0.1 mm as seen in Fig.1. There is a slight difference in the penetration depths between the wave at 2110NHz and 2170MHz. This is not much due to the fact that both frequencies are close.

When the frequency of the propagating wave is increased to 30GHz, one can see a marked difference in the penetration depth into the skin. The penetration depth is vastly reduced in this case as seen in Fig.6. The increased frequency has caused a reduction of the wave penetration to a value very close to the surface of the skin as compared with curves of Figs. 2 to Fig.5. What is also observed here is that the magnitude of the electric field ($\boldsymbol{E}$) does not alter the penetration as can be seen in Fig.6. In Fig.6 (a) the electric field value used is 7.759 V/m while in (b) the value used is 20 V/m and both curves the penetration depth is clearly seen to be the same. This is an indication that the frequency alone determines the depth at which a particular wave attenuates to zero in human tissue.

When the frequency of the propagating wave is increased to 30GHz, one can see a marked difference in the penetration depth into the skin. The penetration depth is vastly reduced in this case as seen in Fig.6. The increased frequency has caused a reduction of the wave penetration to a value very close to the surface of the skin as

compared with curves of Figs. 2 to Fig.5. What is also observed here is that the magnitude of the electric field (***E***) does not alter the penetration as can be seen in Fig.6. In Fig.6 (a) the electric field value used is 7.759 V/m while in (b) the value used is 20 V/m and both curves the penetration depth is clearly seen to be the same. This is an indication that the frequency alone determines the depth at which a particular wave attenuates to zero in human tissue.

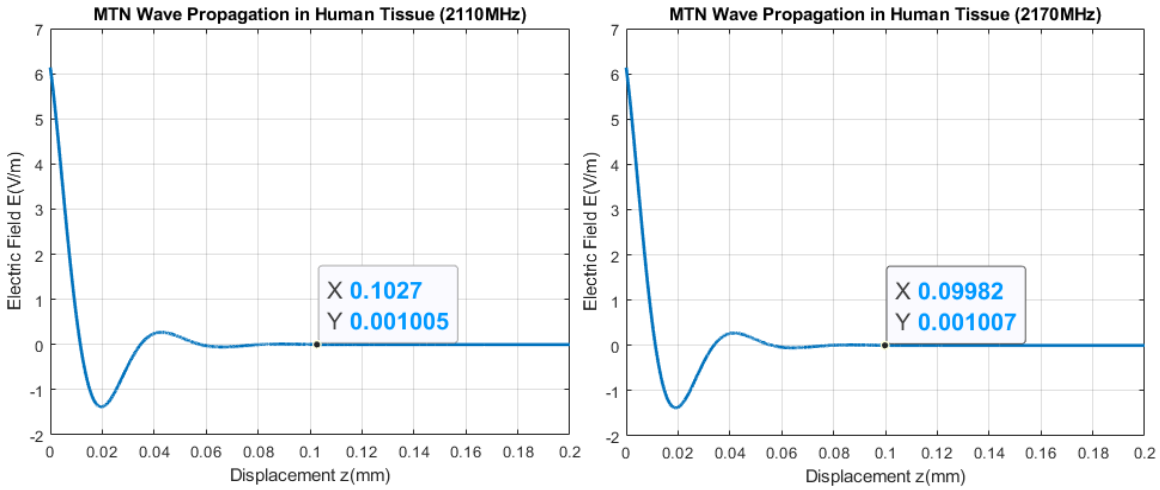

Fig. 4 Wave propagation in human tissue from MTN tower (a) 2110MHz (b) 2170MHz

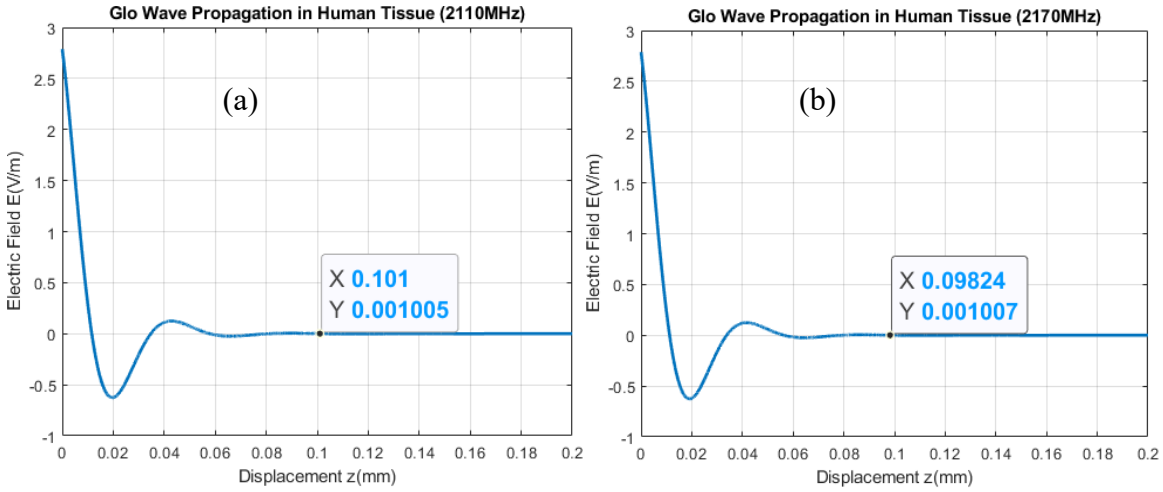

Fig. 5 Wave propagation in human tissue from Glo tower (a) 2110MHz (b) 2170MHz

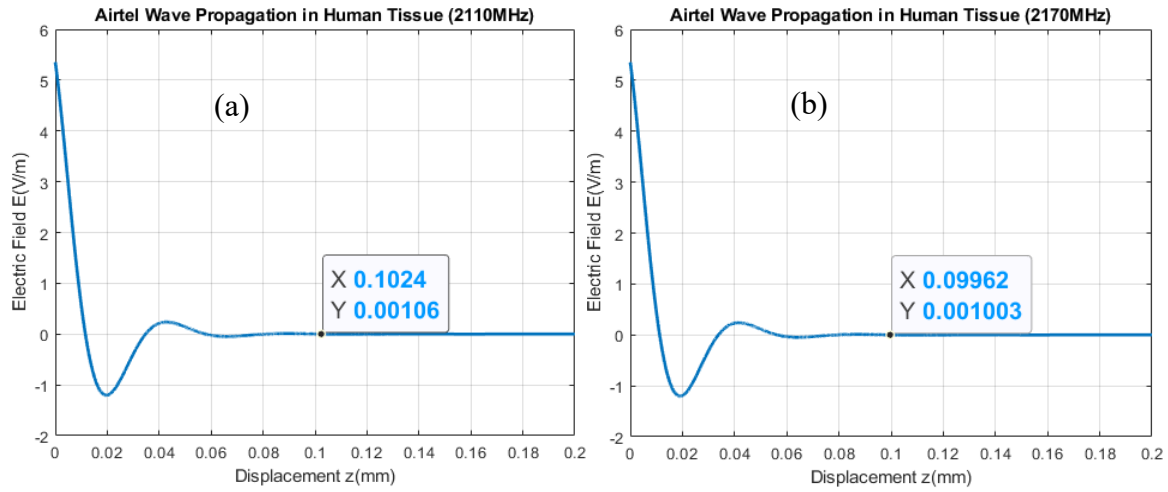

Fig. 6 Wave propagation in human tissue from Airtel tower (a) 2110MHz (b) 2170MHz

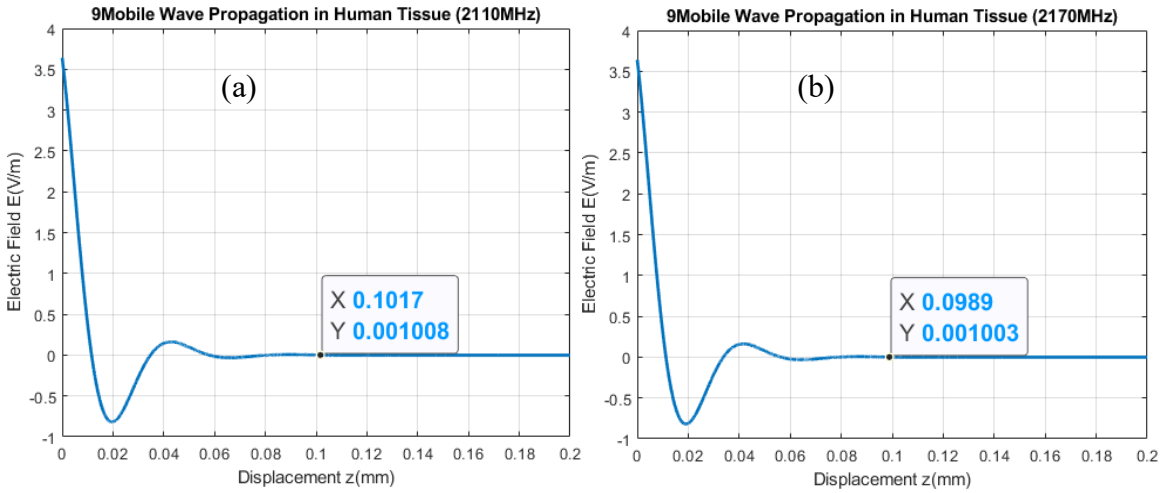

Fig. 7 Wave propagation in human tissue from 9Mobile (a) 2110MHz (b) 2170MHz

When the frequency of the propagating wave is increased to 30GHz, one can see a marked difference in the penetration depth into the skin. The penetration depth is vastly reduced in this case as seen in Fig.8. The increased frequency has caused a reduction of the wave penetration to a value very close to the surface of the skin as compared with curves of Figs. 2 to Fig.5. What is also observed here is that the magnitude of the electric field (***E***) does not alter the penetration as can be seen in Fig.6. In Fig.6 (a) the electric field which a particular wave attenuates to zero in human tissue.

Displayed in Table 1 are the lower and upper frequencies for the frequency bands used by the four major GSM service providers in Nigeria. This shows the network providers, frequency bands, wavelengths, penetration depths and percentage penetration. This table is very important because it shows clearly the layer of the skin, where the wave propagating in the skin tissue at a particular frequency, will completely attenuate to zero. Take for instance if the EM wave is transmitted at a frequency 2110 MHz, the wave travels through the first layer; the epidermis having a thickness band of (0.06 – 0.1) mm and in the second layer; the dermis at a 0.11% penetration.

TABLE 1 FREQUENCY BANDS USED FOR GSM WIRELESS TRANSMISSION

Network Providers	Frequency Bands (MHz)	Wavelength (m)	Penetration Depth (mm)	% Penetration (Layer of skin)
All Networks	2110	0.142	0.103	100 (Epidermis)
	2170	0.138	0.099	99 (Epidermis)
Glo Ng	758	0.396	0.279	6.4 (Dermis)
	803	0.374	0.263	5.8 (Dermis)
MTN Ng	2620	0.114	0.081	81 (Epidermis)
	2690	0.112	0.079	79 (Epidermis)
MTN Ng	791	0.379	0.267	5.9 (Dermis)
	821	0.365	0.257	5.6 (Dermis)
MTN Ng	3400	0.088	0.062	62 (Epidermis)
	3600	0.083	0.059	59 (Epidermis)
Airtel and	1805	0.166	0.119	0.68 (Dermis)
9Mobile Ng	1880	0.160	0.115	0.54 (Dermis)

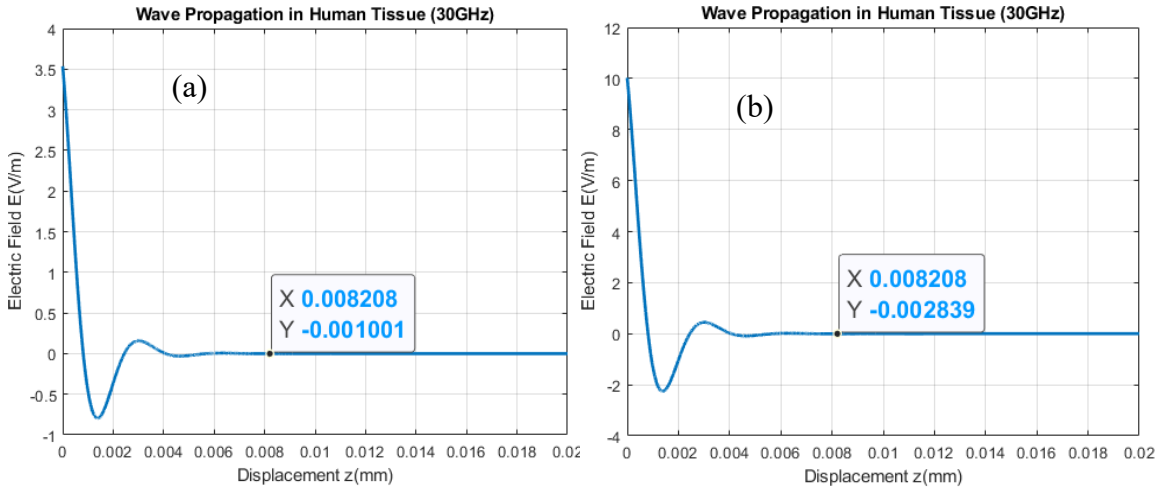

Fig. 8 Wave propagation in human tissue at 30GHz (a) 7.759 V/m (b) 20 V/m

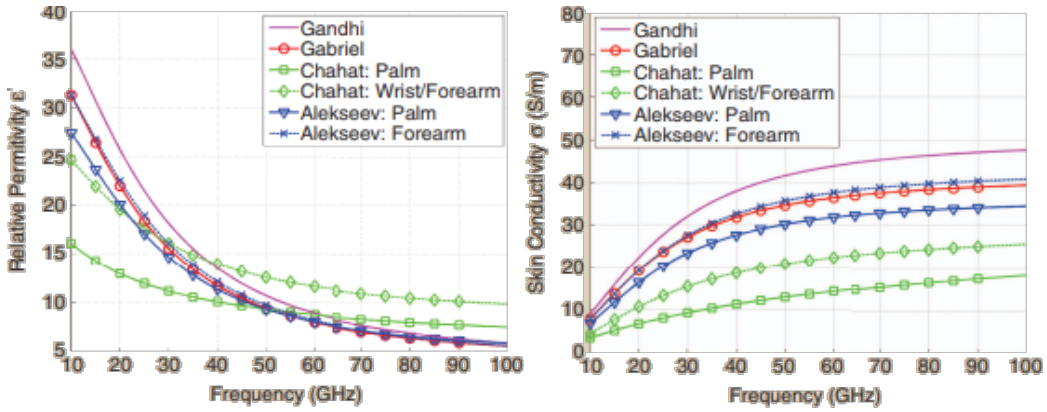

Fig. 9 Relative permittivity obtained by several researchers at frequency from 10 to 100GHz

For validation a comparative analysis of the relative permittivity, skin conductivity obtained by other investigators and oscillating wave pattern computed in this work was done. Referring to Fig. 9, measurements conducted on the skin of various researchers whose names are identified in the legends of the diagrams of Fig. 9 that show the profiles of (a) relative permittivity and (b) skin conductivity. It can be observed that the relative permittivity exhibits high values at the lower frequency and taper asymptotically as the frequency increases as seen in (a). The lower frequency indicated in Fig. 9 is 10 GHz. Similarly, (b) portrays how the conductivity increases rapidly from the lowest frequency of 10 GHz to higher frequency. Electric field pattern computed at 10 GHz in this work is depicted in Fig. 10(a). It can be seen that the field strength is considerably higher at 10 GHz where the relative permittivity is highest and rapidly attenuates to zero at a distance 0.0171 mm. As the frequency of the wave moves further upward to 40 GHz in Fig. 10(b), it is clearly seen that the penetration depth has reduced to 0.06668 mm. In fig.10(c), the frequency has gone up to 70 GHz, further reducing the penetration depth to 0.00387 mm and finally increasing the frequency to 100 GHz will further push the towards the surface of the skin at a depth of 0.002708 mm, when compared to the dimension of the skin in Fig. 1, the relative permittivity tapers to zero. Identically, conductivity profiles rapidly increase from the lowest frequency of 10 GHz to higher frequencies leading to a higher absorption of the electric field oscillations. Hence, the damping oscillations of the electric field occurs. This lends credence to the validity of the electric filed patterns computed in this work.

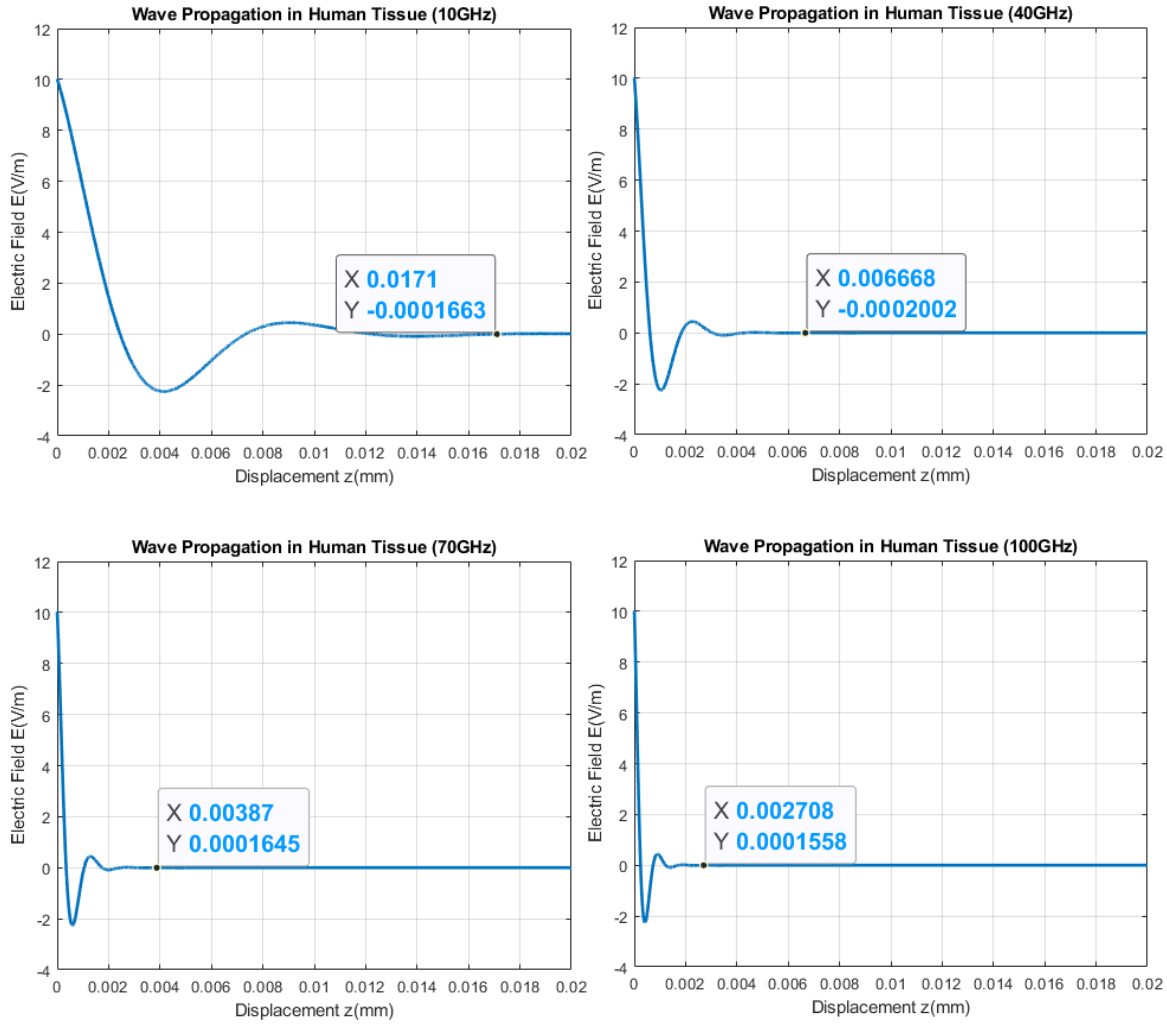

Fig. 10 Penetration depths of varying frequencies, 10 Ghz, 40 Ghz, 70 GHz and 100 GHz

V. CONCLUSION

Based to the analysis conducted for this study, the operating frequency rather than the electric field strength influences how deeply an EM wave penetrates human skin. This is proven by the fact that there is no difference in the penetration depth between the measured electric field values and the theoretical data used to plot for a specific frequency. These validate the fact that frequency alone is responsible for the penetration depth of EM waves into the human tissue**.**

One can therefore realize from the foregoing that at frequencies lower than the microwave bands, such as the radio frequencies, the waves would penetrate deeper into the human tissue, well above the values observed for the microwave bands. Thus, radiofrequency EM waves penetrate deeper than microwaves while the depth of penetration of microwaves is longer than those of mmWave and THz waves. In other words, EM waves at lower frequencies penetrate the epidermis deeper than those at higher frequencies. This allays the fear that licensing and roll out of 5G telecommunication services as being planned by the government portends grave danger to the citizenry.

The results also showed that the wave, depending on the frequency of the wave, attenuates within the first layer, the epidermis having a maximum thickness of 0.1 mm and the second layer which is the dermis which has a maximum thickness of 2.8 mm in the human skin. This is an indication that those people bleaching their skins could be removing the top layer, the epidermis of their skin, thereby allowing a further penetration of the wave into their skin.

REFERENCES

Akpolat, V. Akdag, M. Z. Dasdag, S. Alkis, M. E. Biglin, H. M. Yegin, K. and Yavas, M. C. (2019). Effect of 900-, 1800-, and 2100-MHz Radiofrequency Radiation on DNA and Oxidation Stress in Brain. *Electromagnetic Biology and Medicine*.

Batool, S. Bibi, A. and Mangini, F. (2019). Benefits and Hazards of Electromagnetic Waves, Telecommunication, Physical and Biomedical: A Review. *European Review for Medical and Phamacological Science, 23*, 3121-3128.

Brown, T. W. C. Jamshed, M. A. and Heliot, F. (2020). A Survey on Electromagnetic Risk Assessment and Evaluation Mechanism for Future Wireless Communication Systgems. *in IEEE Journal of Electromagnnetics, RF and Microwaves in Medicine and Biology, 4*(1), 24-36.

Dave, S. Dubey, A. Macwan, S. and Modi, H. (2015). 5G Cellular Communication System with Millimeter Waves: Study of Requirements, Hardware and Biological Effects. *2015 IEEE International Conference on Research in Computational Intelligence and Communication Networks (ICRCICN)*, 285-289.

Gabriel, C. Gabriel, S. and Corthout, E. (1996). The Dielectric Properties of Biological Tissues: I. Literature Survey. *Physics in Medicine & Biology, 41*(11).

Gandhi, O. P. and Riazi, A. (1986). Absorption of Millimeter Wave bby Human Beings and its Biological Implications. *IEEE Transactions on Microwave Theory and Techniques, 34*(2), 228-235.

Hu, C. Zuo, H. and Li, Y. (2021). Effects of Radiofrequency Electromagnetic Radiation on Neurotransmitters in the Brain. *Frontiers in Public Health , 9*, 1-15.

Jeong, N. S. Ou, Y. Tassoudji, A. Dunworth, J. Koymen, O. and Raghavan, V. (2018). A Recent Development of Antenna-in-package for 5G Millimeter Wave Application (Invited paper). *2018 IEEE 19th Wireless and Microwave Technology Conference (WAMICON)*, 1-3.

Julian, B. Andrea, D. Iman, F. Lourdes, F. Sammut, C. V. (2020). Application Artificial Neural Networks for Accurate Determination of the Complex Permittivity of Biological Tissue. *Sensors Basel, 20*(16).

Lewandovski, A. Szyplowska, A. Kafarski, M. Wilczek, A. Barmuta, P. and Skierucha, W. (2017). 0.05-3 GHz VNA Characterization of Soil Dielectric Properties Based on the Multiline TRL Calibration. *Meas. Sci. Technol, 28*(2).

Lopez-Djeda, W. Pandey, A. Alhajj, M. and Oaklay, A. M. (2021). Anatomy, Skin (Integument). *StatPearls Publishing LLC*.

Ma, L. Shen, H. B. and Liu, L. (2013). Analysis of Wave Propagation on Human Body Based on Stratified Media Model. *Journal of Central South University, 20*, 3545-3551.

Miklavcic, D. Pavselj, N. and Hart, F. X. (2006). Electrical Properties of Tissues. *Wiley Encyclopedia of Biomedical Engineering*.

Odemer, R. and Odemer, F. . (2019). Effects of radiofrequency electromagnetic radiation (RF-EMF) on honey. *Science of the Total Environment, 661*, 553-562.

Sehrai, D. A. Altaf, A. Abdullah, M. Tufail, M. Irfan, M. Kiani, S. H. Glowacz, A. Rahman, S. Muhammad, F. (2020). A Novel, High Gain Wideband MIMO Antenna for 5G Millimeter Wave Application. *Electronics, 9*(6).

Simko, M. and Mattsson, M. O. (2019). 5G Wireless Communication and Health Effects - A Pragmatic Review Based on Available Studies Regarding 6 to 100GHz. *Int. J. Environ. Res. Public Health*.

Yinliang, D. Rashed, E. A. and Hirata, A. (2020). Assessment of Absorbed Power Density and Temperature Rise for Nonplanar Body Model Under Electromagnetic Exposure Above 6 GHz. *Physics in Medicine and Biology, 65*(22).

Journal of Engineering, Emerging Technologies and Applied Sciences -– Volume 1 Issue 2, Nov. 2023

Available at ***https://www.ndu.edu.ng/journalofengineering/***

RESEARCH ARTICLE OPEN ACCESS

Model Development for Prediction of Concrete Compressive Strength: Advancing Construction Industry Practices and Quality Control Standards

John A. Trust God, Dio. A. Wenapere, Odudu Joshua, and Appi A. Stephen

Department of Civil Engineering, Niger Delta University, Bayelsa State, Nigeria

johteskconzults@gmail.com

----------**********----------

Abstract:

In construction, the selection of concrete mix grades centres on the specified strength outlined in the design. However, achieving the desired strength necessitates laborious and costly experimental investigations. This inspires the current study, which seeks to establish an equation to predict concrete compressive strength (CS) based on water to cement ratio (WCR), reducing the need for costly experimental investigations. 90 concrete cube samples were made using Portland limestone cement of 42.5 N grades, with WCR ranging from 0.45 to 0.65 and two different mix ratios. Strength was tested at 7, 14, and 28 days, with statistical analysis focusing on the 28-day CS. Models developed using Design Expert software exhibited over 94% accuracy in predicting 28-day compressive strength, indicating strong alignment with experimental data. Fit Statistics indicated a satisfactory fit with adjusted R^2 of 0.9932 and predicted R^2 of 0.9715. Adequacy precision, signalling the signal-to-noise ratio, exceeded 4, indicating a robust model. P-value was significant (<0.05), and the F-value (583.28) suggested the model's significance in predicting CS. The findings imply the model's potential for guiding design decisions effectively.

Keywords — **Model, Water, Cement, Strength, Concrete, Statistical**

----------**********----------

I. INTRODUCTION

Water is the most widely used natural resource on our planet, followed closely by concrete, which ranks as the second most commonly employed building material worldwide (Alhaji, 2016: John et al 2019). Concrete, a composite construction material, is constituted of sand, cement, water and, gravel in precise proportions. To produce concrete that possesses qualities of robustness, durability, and cost-effectiveness, it is imperative that the aggregates, constituting 75 percent of an ideal concrete mix, conform to established criteria (Alhaji, 2016). The strength of concrete stems from cement's capacity to retain water (John et al 2019a). As a result of its early retention of moisture, the cement particles are bonded together inside an unstable framework surrounded by a moisture-saturated region. An increase in the water-to-cement ratio (WRC) will further increase the average spacing between the cement grains (Harrison, 1992). Concrete hardens as a result of an action known as hydration caused by water. According to Fayaz and Chidiac (2015), the WCR should be referenced when studying the compressive strength (CS) of concrete. The water-to-cement ratio is contingent on the concrete's grade and is crucial for upholding its durability (Nduka at al., 2018; Basheer et al., 2017). To enhance strength, high-grade concrete may incorporate plasticizers to lower the WCR (Xiao 2017; Gupta et al., 2021).

II. REVIEW OF EXISTING MODELS

The CS of concrete is the main mechanical property that may be assessed by studying a 7 to 28-day-cured concrete cylindrical or cube specimen. As noted by Noorzaei et al. (2007), factors such as WCR, aggregate quality, and the strength of the cement significantly influence the overall strength of concrete. There has been a great deal of research into developing a model for predicting the CS of concrete. In 1892, Feret was the first to propose a formula as shown in equation (1) for predicting the CS of concrete (Popovics 1985). The author anticipated that the cement-to-paste-to-air ratio governed the CS of concrete; nevertheless, experimental evidence revealed that these predicted CS values were not substantiated by facts.

$$CS = A\left(\frac{V_{oc}}{V_{oc} + V_{oa} + V_{ow}}\right)^{B} \quad (1)$$

where,
V_{ow} = volume of water
V_{oa} = volume of air
CS = concrete compressive strength
A, B = calibration constants
V_{oc} = volume of cement.

Abrams (1919) proposed a ground breaking method for assessing concrete strength by introducing the concept of the WCR in the prediction of CS. This innovative approach marked Abrams as one of the pioneering figures to recognize and emphasize the paramount importance of this ratio in determining concrete's structural integrity and durability. His forward-thinking insight revolutionized the field of concrete technology and laid the foundation for modern concrete mix design methodologies, profoundly influencing the construction industry's approach to achieving optimal concrete performance. Based on this ratio, he developed a model as presented in Equation 2, that was thought to be simpler and had better agreement with the strength data for non-air embedded concrete. Nevertheless, Fayez and Chidiac (2015) pointed out that the calibration coefficients A and B of this model presented challenges.

$$CS = \frac{A}{B^{w/c}} \quad (2)$$

where,
CS = concrete compressive strength
A, B = calibration constants
w = quantity of water
c = quantity of cement

Popovics (2008), modified Abrams (1919) empirical model by introducing cement parameter into Equation (2.0). The modified model according to Fayez and Chidiac, (2015) takes into consideration cement content and air parameters. The modified equation is presented in Equation 3.

$$CS = \frac{A}{B^{[(w/c)+mc]}} \times 10^{-0.038V_a} \quad (3)$$

where,
CS = compressive strength of concrete
A, B, m = calibration constants
c, w = quantity of cement and water
V_a = volume fractions of air

Pann et al. (2003) studied Abrams' equation and developed a model which contains WCR as presented in Equation (3) by integrating through empirical observation the binder pastes capillary porosity (CP). According to authors, CP depend the level of hydration.

$$CS = \frac{A}{B^{w/c}} + \frac{C}{D^{CP}} \quad (4)$$

CS = concrete compressive strength
A, B, C, D = calibration constants
W/C = Water to Cement Ratio
CP = Capillary porosity

Fayez and Chidiac (2015) investigated compressive strength prediction models and reported that almost all the models give a satisfactory prediction since strength is typically influenced by WCR compared to gradation and properties of aggregates.

In construction, the selection of concrete mix grades centres on the specified strength outlined in the design (Wilby,2013). However, achieving the desired strength necessitates laborious and costly experimental investigations (Shi, et al 2015). This motivates the current study, which seeks to establish an empirical model for predicting the CS of concrete based on its WCR. This endeavour holds significant

promise, as an accurate empirical model for determining concrete strength could alleviate the immediate need for extensive and resource-intensive experimentation in subsequent projects.

By formulating a reliable predictive model, this research aims to streamline the process of ascertaining concrete strength, offering an effective tool for engineers and construction professionals. Such a model would not only expedite decision-making in material selection and mixture design but also enhance the overall efficiency and cost-effectiveness of construction projects (Mehta, 2002). Additionally, it could pave the way for more innovative and sustainable approaches to concrete utilization, ultimately contributing to advancements in construction technology and the broader field of civil engineering. This study thus represents a fundamental step towards optimizing concrete performance and ushering in a new era of efficiency in construction practices.

III. . MATERIALS AND METHODS

A. Materials

The study employed Portland limestone cement of grade 42.5 N, which adheres to the standards set forth in BS EN 197-1 (2011) and, both coarse and fine aggregates, in accordance with EN 932, were used. These aggregates were procured from sources within the Niger Delta University Campus, situated in Bayelsa State. The physical properties of the aggregates were examined to determine their suitability. It's noteworthy that the water utilized for the concrete mixture was devoid of any impurities, ensuring the integrity of the mixture. This meticulous selection of materials and stringent quality control measures underscores the precision and reliability of the experimental setup.

B. Method

1) Preparation of the test specimen

Portland limestone cement of 42.5 N grades was used to produce a total of ninety (90) concrete cube samples of 150 mm x 150 mm x 150 mm, with WCRs of 0.45, 0.50, 0.55, 0.60, to 0.65. A 1:1.5:3 and 1:2:4 by weight were chosen for this investigation. The cubes were then put through a curing process and examined for the effect of WCR on the CS at 7, 14, and 28 days.

2) Statistical Data Analysis, Model Development, Optimization and Test Results Application

Having considered five WRCs of 0.45, 0.50, 0.55, 0.60 and 0.65 experimentally, only CS at 28 days' response was statistically analysed using Design Expert. A number of models were chosen from the Design Expert software and examined for their appropriateness in modelling the CS equation. Cubic, special cubic, quadratic, and linear models are among those available as shown equations (5), (6), and (7). These types of models are clearly distinguishable from response surface approaches by the absence of an intercept term.

$$Y = b + \beta_1 x_1 + \beta_2 x_2 + \beta_3 x_3 + \cdots + \beta_n x_n \quad (5)$$

$$Y = b + \beta_1 x_1^2 + \beta_2 x_2^2 + \beta_3 x_3^2 + \cdots + \beta_n \quad (6)$$

$$Y = b + \beta_1 x_1^3 + \beta_2 x_2^3 + \beta_3 x_3^3 + \ldots + \beta_n x_n^3 \quad (7)$$

Generally, the software's built-in algorithm uses each model to choose design points. By default, higher-order models, for example, will normally necessitate more points. Experimental results obtained were analysed statistical with Design Expert software. Analysis of variance (ANOVA) was considered to evaluate the implication of the equations. The ANOVA values were examined in terms of standard deviation, p value, sum of squares, F value, coefficient of variation, adjusted (R^2), coefficient of determination (R^2), and adequate precision.

IV. . RESULTS AND DISCUSSION

The findings of this investigation are elaborated upon and analysed in section A to **3.4**. This segment provides a comprehensive overview of the results, offering a detailed examination and interpretation of the data gathered during the course of the study. Through thorough presentation and discussion, this section aims to shed light on the key insights and implications derived from the experimental outcomes, contributing to a deeper understanding of the relationship between WCR and concrete CS, and also the developed empirical model.

A. Results for Physical Properties of Aggregates

The results of the physical properties examination carried out on the aggregates are illustrated in Table 1 and Figures. 2 and 3. The results of specific gravity and water absorption are within the stated limits of ASTM. Also, the particle distribution as illustrated in Figures 1 and 2 confirm that the coarse and fine aggregates, respectively, are well-graded.

TABLE 1. PHYSICAL PROPERTIES

Test conducted	Results	Code referenced	Code
Coarse Aggregate			
Specific gravity	2.58	ASTM C128, (2001)	2.55 -2.75
Water absorption (%)	0.6	BS 812 part 2, (1995)	< 3.5%
Fine Aggregate			
Specific gravity	2.72	ASTM C128, (2001)	2.55 - 2.75
Water absorption (%)	0.80	BS 812 part 2, (1995)	< 15%

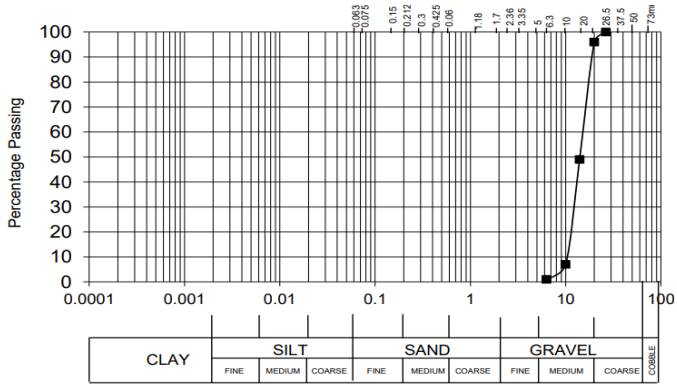

Fig. 1 Sieve analysis graph for coarse aggregate

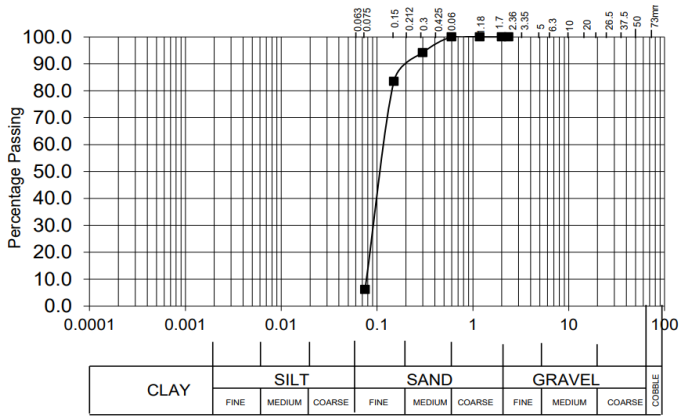

Fig. 2 Sieve analysis graph for fine aggregate

B. Concrete strength results

Table 2, Fig. 3 and Fig.4 present the CS results for mix ratios of 1:2:4 and 1:1.5:3, encompassing a range of WCR ranging from 0.45 to 0.65. Notably, Fig. 3 and Fig.4 and Table 2 both demonstrate a remarkable trend. The CS experiences a steady ascent up to a WCR of 0.55, where it reaches its maximum. However, once the WCR surpasses 0.55, the CS begins to decline. Specifically, for concrete with a mix ratio of 1:2.4, the CS values stand at 22.67 MPa, 23.33 MPa, 28.30 MPa, 24.78 MPa, and 23.48 MPa corresponding to WCRs of 0.45, 0.50, 0.55, 0.60, and 0.65, respectively. Meanwhile, for concrete with a mix ratio of 1:1.5:3, the CS figures are 16.30 MPa, 32.30 MPa, 33.41 MPa, 28.89 MPa, and 22.07 MPa with matching WCRs of 0.45, 0.50, 0.55, 0.60, and 0.65, respectively. Referring to Table 2, the reduction in CS observed beyond the 0.55 WCR ratio can be attributed to the phenomenon of concrete bleeding and the subsequent separation of aggregates. This insightful data illuminates the critical role that the WCR plays in determining the compressive strength of the concrete mixes, offering significant understandings for optimizing concrete preparations in future construction endeavours.

TABLE 2: CS OF CONCRETE FOR A 1:2:4 AND 1:1.5: 3 MIXES WITH VARIOUS WCR

Water/cement Ratio	7 days CS (MPa)	14 days CS (MPa)	28 days CS (MPa)
1:2:4 mix			
0.45	14.30	20.44	22.67
0.50	15.85	22.33	23.33
0.55	21.48	28.22	28.30
0.60	16.11	20.37	24.78
0.65	15.48	19.78	23.48
1:1.5:3 mix			
0.45	14.83	25.89	16.30
0.50	24.44	29.67	32.30
0.55	25.33	28.52	33.41
0.60	19.48	23.00	28.89
0.65	17.44	17.11	22.07

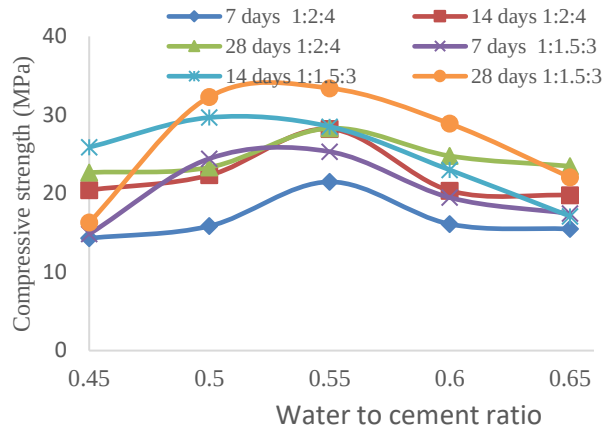

Fig. 3 CS vs water-to-cement ratio

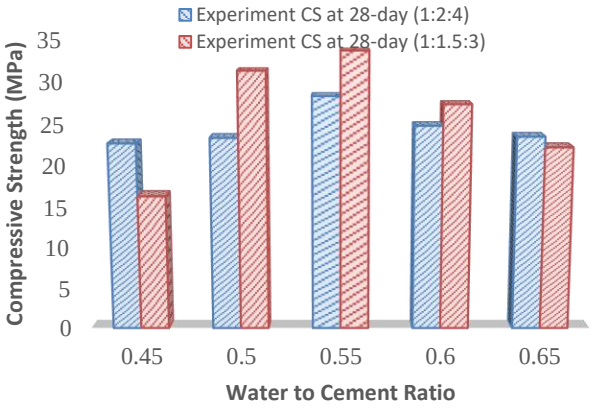

Fig. 4 Bar Chart Showing Strength Variation

C. Model Results and ANOVA

The transform used was Logit, with 22.66 and 181 as lower and upper bounds, respectively, for a 1:2:4 mix and 16.29 and 35 as lower and upper bounds, respectively, for a 1:1.5:3 mix. When the P-value is lower than 0.0500 and the F-value is higher than 0.1000, model terms are deemed substantial. Otherwise, they are deemed inconsequential. Table 3 shows that the P-value is less than 0.0500, which is significant. The F-value of the statistical model (583.28) shows that it could be significant. An F-value this high could have been caused by noise only 0.01% of the time.

Referring to Table 4, it is clear that the difference between the adjusted R^2 (0.9932) and the predicted R^2 (0.9715) the is absolutely below 0.2, it is satisfactory to conclude that these two values are in good alignment. When the adequacy precision, which measures the signal-to-noise ratio, surpasses 4, it is desirable. In this scenario, the signal is more than adequate, with a ratio of 50.340. As a result, this model may successfully guide design decisions within the confines of the available area. The empirical models for CS as a response and WCR as a factor from the ANOVA study is of the form Equations (8) and (9). Equations (8) and (9) were developed to predict the CS of concrete produced from 1:2:4 and 1:1.5:3, respectively.

TABLE 3: ANNOVA SUMMARY FOR THE CS

Source	Sum of Squares	df	Mean Square	F-value	p-value	
Model	87.42	3	29.14	583.28	< 0.0001	significant
A-WCR	0.1857	1	0.1857	3.72	0.0860	
A^2	45.24	1	45.24	905.58	< 0.0001	
A^3	0.5045	1	0.5045	10.10	0.0112	
Residual	0.4496	9	0.0500			
Lack of Fit	0.4496	1	0.4496			
Pure Error	0.0000	8	0.0000			
Cor Total	87.87	12				

TABLE 4: FIT STATISTICS

Std. Dev.	0.2235	R^2	0.9949
Mean	-5.95	Adjusted R^2	0.9932
C.V. %	3.75	Predicted R^2	0.9715
		Adeq Precision	50.3403

Referring to Table 4, it is clear that the difference between the adjusted R^2 (0.9932) and the predicted R^2 (0.9715) the is absolutely below 0.2, it is satisfactory to conclude that these two values are in good alignment. When the adequacy precision, which measures the signal-to-noise ratio, surpasses 4, it is desirable. In this scenario, the signal is more than adequate, with a ratio of 50.340. As a result, this model may successfully guide design decisions within the confines of the available area. The empirical models for CS as a response and WCR as a factor from the ANOVA study is of the form

Equations (8) and (9). Equations (8) and (9) were developed to predict the CS of concrete produced from 1:2:4 and 1:1.5:3, respectively.

$$CS = \frac{181e^{\beta_0+\beta_1+\beta_2+\beta_3} + 22.66}{1 + e^{\beta_0+\beta_1+\beta_2+\beta_3}} \quad (8)$$

where,
CS = compressive strength (MPa)
β_0 = -360.94055,
β_1 = 1711.45466WCR,
β_2 = -2692.96169WCR2.
β_3 = 1387.26871WCR3
WCR = water-to-cement ratio

$$CS = \frac{35e^{\alpha_0+\alpha_1+\alpha_2+\alpha_3} + 16.29}{1 + e^{\alpha_0+\alpha_1+\alpha_2+\alpha_3}} \quad (9)$$

where,
CS = compressive strength
α_0 = -1167.17269
α_1 = 6063.35668WCR
α_2 = -10402.08959WCR2
α_3 = 5899.31862WCR3
WCR = water-to-cement ratio

1) Model Validity

By contrasting the compressive strength of concrete produced from the experiment with that anticipated by the model, the developed model was proven to be accurate. Numerous analytical techniques, including mathematical and pictorial analysis, were used to validate the model. Table 5 reveals that the CS prediction made by the empirical model is significant.

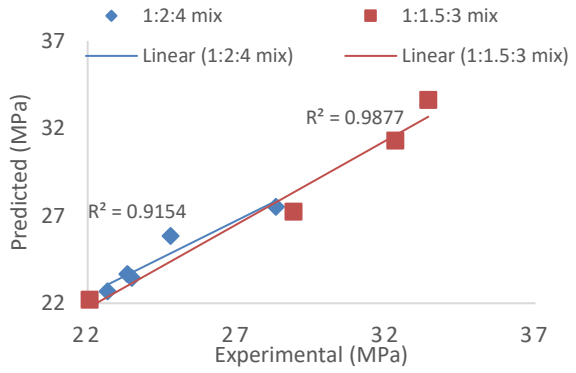

Fig. 5 Predicted v experimental

The values shown in Table 5 demonstrate how conservatively Equations (8) and (9) predicts the CS of 1:2:4 and 1:1.5:3 concrete mixes.

TABLE 5: ANALYTICAL MODEL FOR COMPRESSIVE STRENGTH

Water/cement Ratio	Experimental CS at 28 days (MPa)	Predicted CS at 28-day Equations (MPa)
	1:2:4 mix	
0.45	22.67	22.67
0.50	23.33	23.67
0.55	28.30	27.51
0.60	24.78	25.85
0.65	23.48	23.45
	1:1.5:3 mix	
0.45	16.30	16.30
0.50	32.30	31.29
0.55	33.41	33.63
0.60	28.89	27.23
0.65	22.07	22.20

2) Statistical Analysis

Correlation: Design Expert provided the correlation factor relating to the WRC and the CS of concrete. For the corrected and projected models, these findings are 0.9932 and 0.9715, respectfully. It is acceptable to state that the projected R2 of 0.9715 and the corrected R2 of 0.9932 are reasonably in conformity since the variation between the two is less than 0.2. Less than 2 MPa of standard error was recorded while predicting the model-based CS over a 28-day period. Excel from Microsoft 2019 was used to assess the standard error.

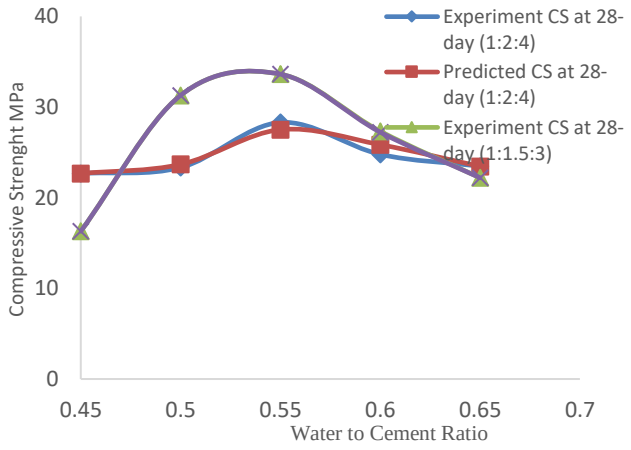

Fig. 6 Strength vs Water-to-Cement Ratio

The model's validity was further confirmed by plotting values of the experimental CS and the predicted CS against the different water-to-cement ratios. Fig. 5 shows the predicted strength of Eq. (8) and ((9). The coefficient of regressions was found to be 0.9154 for 1:2:4 mix and 0.9877 for 1:1.5:3 mix. Fig. 6 illustrates a strong trend in the curves and patterns, indicating a notably similar trend in the distribution of data points for both the experimentally measured and predicted CS. This trend in the graphical representation confirms the agreement observed in Table 5 between the two sets of results.

V. CONCLUSION

Empirical models to predict the 28-day compressive strength in relation to its water-to-cement ratio for 1:2:4 and 1:1.5:3 mixes were developed. The idea of using water-to-cement ratio as the only variable in developing the empirical model as seen in this investigation was conducted because water has a significant effect on the strength.

From the finding, the following conclusions were established:

i. the developed models exhibit an impressive accuracy of over 94% in predicting the 28-days compressive strength. This high level of precision is attributed to their exceptional fit with the experimental data, affirming their reliability and robustness in estimating concrete strength over an extended period;

ii. for the predicted for 28-day compressive strength, the standard error is less than 2 MPa, underscoring the remarkable precision and reliability of the predictive models;

iii. the models are developed to only predict 28-days compressive strength; Unfortunately, they lack the capability to provide accurate predictions for compressive strengths at 7 or 14 days, highlighting their limited applicability in those contexts; and

iv. Both the models and experimental findings clearly indicate that the optimal mix attains its maximum strength at a water-cement ratio (WCR) of 0.55. This ratio proves to be the most conducive for achieving peak strength.

REFERENCES

Abrams, L. D., (1919). Properties of concrete, 3rd edition, Pitman Publishing LTD, London.

Alhaji, B., (2016), Statistical Modelling of Mechanical properties of Concrete made from Natural Coarse Aggregates from Bida Environ. Doctor of Philosophy (PhD) Thesis, Department of Civil Engineering, Federal University of Technology, Minna, Niger State, Nigeria.

ASTM C128: 2001. Standard Test Method for Density, Relative Density (Specific gravity), and Absorption of Fine Aggregate, ASTM International, West Conshohocken, PA, USA. DOI: 10.1520/C0128-22. https://www.astm.org/standards/c128

British Standard Institution. Composition, specification and conformity criteria for common cements, BS EN 197: Part 1, 2011, BSI, London.

British Standard Institution. Tests for general properties of aggregates, BS EN 932, BSI, London. 1999.

BS 812 2: 1995. Methods for Determination of Density, Water Absorption, British Standard Institution, London, United Kingdom.

BS EN 196-6 (2018). Methods of testing cement: Determination of fineness. British Standards Institution, 389 Chiswick High Road, London, www.bsigroup.com

BS EN 933-1 2012. Tests for Geometrical Properties of Aggregates. Determination of Particle Size Distribution, Sieving Method, British Standard Institution, London, UK.

Fayaz, S., Rashid, S., and Reddy, K. Y. (2017). Behavior of Concrete with Quarry Dust as Partial Replacement of Fine Aggregate. International Journal for Modern Trends in Science and Technology.3(7). pp 105-112

Fayez M., and Samir E. C., (2015) Assessment of Concrete Compressive Strength Prediction Models, KSCE Journal of Civil Engineering. 20(1). pp 1-15.

Gupta, D. S., Islam, T., Chakma, P., Palash N. MD., and Shohan, A. S. (2021). Experimental Study of Concrete with Sugarcane Bagasse Ash (SCBA) at Elevated Temperature. Malaysian Journal of Civil Engineering. 33(3), pp 59-67.

John, A. T., Akosubo, I. S., and Ann D, M., (2019). The Use of Calcined Waste Glass Powder as a Pozzolanic Material. EJERS, European Journal of Engineering Research and Science. 4(12), pp 53 -56,

John, A. T., Orumu, S. T., and Nelson, T. A., (2019). The Effect of the Presence of Ferric Iron in Water Used for the Production of Concrete on its Compressive Strength. EJERS, European Journal of Engineering Research and Science. 4(8), pp 95 -98.

Nduka, D. O., Fagbenle, O. I., Joshua, O., Ogunde, A. O., and Omuh, I. O. (2018). Comparative Analysis of

Concrete Strength Utilizing Quarry-crushed and Locally sourced Coarse Aggregates, International Journal of Mechanical Engineering and Technology (IJMET). 9(1), pp 609-617.

Mehta, P. K. (2002). Greening of the concrete industry for sustainable development. Concrete international, 24(7), 23-28.

Noorzaei, J., Hakim, S. J. S., Jaafar, M. S., and Thanoon, W. A. M., (2007). Development of artificial neural networks for predicting concrete compressive strength. International Journal of Engineering and Technology. 4(2). pp 141-153

Popovics, S., (2008) History of a mathematical model for strength development of Portland cement concrete. ACI Materials Journal 95(5): pp 593–600.

Popovics, S., and Ujhelyi, J., (2008) Contribution to the concrete strength versus water-cement ratio relationship. Journal Material Civil Engineering 20(7): pp 459-463.

Popovics. S., (1985) New formulas for the prediction of the effect of porosity on concrete strength. ACI Materials Journal 82(2): pp 136–146.

Shi, C., Wu, Z., Xiao, J., Wang, D., Huang, Z., and Fang, Z. (2015). A review on ultra high-performance concrete: Part I. Raw materials and mixture design. Construction and Building Materials, 101, 741-751.

Wilby, C. B. (2013). Structural Concrete: Materials; Mix Design; Plain, Reinforced and Prestressed Concrete; Design Tables. Elsevier.

Xiao-Yong., W., 2017. Modeling of Hydration, compressive strength and carbonation of Portland Limestone Cement (PLC), Materials, 10(115): pp.1-6.

Journal of Engineering, Emerging Technologies and Applied Sciences -– Volume 1 Issue 2, Nov. 2023

Available at ***https://www.ndu.edu.ng/journalofengineering/***

RESEARCH ARTICLE OPEN ACCESS

Strength Properties of Paving Stone Composites with Polyethylene Terephthalate (PET) as Total Cement Replacement

Kiridi, E. A*, Mac-Eteli, H. D**, Alagba, M. B*

*Department of Agricultural Engineering, Niger Delta University, Bayelsa State, Nigeria

Email: ebizimor.kiridi@ndu.edu.ng

** Department of Civil Engineering, Niger Delta University, Bayelsa State, Nigeria

----------**********----------

Abstract:

This study is on the strength properties of paving stone composites with polyethylene terephthalate (PET) waste as total cement replacement. The PET wastes were melted and mixed with river sand to form paving stone composites (PSCs) of PET-sand mix ratio of 1:3, labelled (PET: 10%, 20%, 30%, 40%, and 50%); and sand-cement mix of 1:3 labelled PET 0% as the control. Three replicates of PSCs of each mix ratio and control, were casted in a mold measuring 50mm × 100mm × 200mm, cured for 28 days. Each sample were then tested for density and compressive strength and their mean values were determined. The results showed that the control had highest mean value of 2160 kg/m^3 and the mean densities of the PSCs range from 1860 kg/m^3 to 1670 kg/m^3. All the PSCs samples showed impressive compressive strengths with PET 30 % having highest mean value of 20.59 N/mm^2 while the control had the least mean compressive strength of 8.63 N/mm^2. Analysis of variance shows that the inequality observed between PSCs mean values for density and compressive strength and the control were significant at 95 percent confidence level. It can therefore be concluded that PET waste can be used as total cement replacement in the production of paving stones for pedestrian path and residential parking lot.

Keywords — **Polyethylene terephthalate, paving stone composites, density, compressive strength**

----------**********----------

I. INTRODUCTION

Polyethylene terephthalate (PET) materials are used for packaging globally and end up as waste after use. With the remarkable increase in population (urbanization and commercial activities), the waste generation streams have also increased and has become a major challenge to municipal waste managers and other relevant authorities. These bio-nondegradable PET materials like empty plastic bottles, packaged water sachets, empty food packaging packs etc which are discarded by humans, are swept by rain, clogging up drainages and canals. In most cases, these clogged waterways cause flash flooding at the blink of a light downpour (Emeka and Lesley, 2020). Although, PET materials such as water and soft drinks plastic bottles are currently being reused mostly by small and medium-sized enterprises (SME's) owners to package varying local products such as liquid soap, kerosene, zobo drink, palm oil, vegetable oil, etc in developing countries. This practice only offers a temporary solution by taking some of these waste materials off the streets but large volumes are still seen all over the places.

II. RELATED LITERATURES

Puttarajs et al. (2018) manufactured plastic soil-bricks with bitumen, polyethylene terephthalate (PET), polypropylene (PP), and earth quarry debris. In the study, 60% - 80% PET aggregate and 2% - 5% bitumen were used in the manufacturing process and PET shows good resistant properties. The bitumen enhanced the binding property of the PET. The compressive strength was 10 N/mm^2 with 5% bitumen and 70% PET mix ratio. With 2% bitumen

and 45% PET waste, the water absorption was 0.9536%. And also, polypropylene has higher compressive strength. Seghiri et al. (2017) reported that floor and roofing tiles were also made from recyclable plastics bottles. Sand and high-density polyethylene (HDPET) with 30-80% mix ratio was used to manufacture floor tiles. Testing for density, impermeability, and flexural breaking stress revealed that as the amount of plastic waste increase, flexural strength increase, and tile density decrease from 1.8 kg/m^3 to 1.379 kg/m^3.Agyeman et al., (2018) utilized plastic waste as binders for paving blocks production along with cement: quarry dust: sand with (1:1:2) mix ratio measured by weight / volume. Composite paving blocks less in plastic (LP) with 1:1:2 mix ratio and high in plastic (HP) with 1:0.5:1 mix ratio measured by weight/volume. The study revealed that paving blocks in HP and LP have compressive strengths of 8.53 N/mm^2 with 0.5% water absorption and 7.31 N/mm^2 with 2.7% water absorption respectively, higher than the control value of 6.07 N/mm^2 with 4.9% water absorption. Almeshal et al., (2020) examined the effects of utilizing recycled poly-ethylene terephthalate (PET) waste as a partial replacement for sand in concrete. They looked at how this substance affected the mechanical and physical characteristics of concrete. Six samples (0%, 10%, 20%, 30%, 40% and 50%) of PET concrete mix were prepared, partially replacing sand. Concrete was cast to determine the behaviour of fresh and hardened concrete in terms of workability, unit weight, compressive strength, flexural strength, tensile strength and pulse velocity. The findings reveal a decrease in unit weight, the concrete's mechanical properties were adversely affected by the replacement of the sand. Youcef et al. (2014) explores the possibility of recycling plastic bags waste to concrete where the variable percent of sand is substituted. The work reveals that plastic bag waste can replace conventional aggregates in concrete without any long-term detrimental effects and with acceptable strength development properties. Zainab and Al-Hashmi (2008) showed the idea of employing various plastic wastes as fine aggregates up to 4.75 mm in concrete, containing roughly 80% polyethylene and 20% polystyrene. The compressive tests revealed that as the plastic waste content in the concrete increased, the compressive strength values of the plastic waste concrete decreased below the reference concrete at each curing age. At 28 days after curing, the concrete containing 10% plastic trash had the lowest compressive strength, nearly 30% lower than the reference concrete mixture. The study also discovered that concrete mixes containing 10%, 15%, and 20% plastic aggregates had densities that were 5%, 7%, and 8.7% lower, respectively. Alaloul et al., (2020) replaces clay and cement with polyethylene terephthalate (PET) and polyurethane (PU) binders while making interlocking bricks. Before mixing the plastic bottles with polyurethane (PU) and polymer, the bottles were finely chopped and grated to a size of 0.75 mm. The interlocking brick machine mold was used to condense the mixer. The highest compressive strength attained using polyethylene terephthalate (PET) and polyurethane (PU) in the ratio of 60:40 was 84.54% (less than the control group), the highest tensile strength was 1.3 MPa, and the maximum impact value was 23.343 J/m. There was a thermal conductivity of 0.15 to 0.3W/m K. These bricks were recommended for usage as a partition wall and were determined to be suitable as non-load-bearing masonry bricks. According to Gharif et al., (2010) paving stone must be able to withstand vehicle loads and have aggravation or resistance to slip, especially at crossroads where traction force due to vehicle wheels, either by braking force or acceleration, so the paving block condition will quickly damage or worn out. Standard Nasional Indonesia (SNI 03-0691-1996), classified paving stone based on the class of use as follows: Concrete brick of quality A: used for road; Concrete brick of quality B: used for parking lot; Concrete brick C: used for pedestrians; Concrete brick D: used for parks and other users. This research aims to develop a sustainable, practical approach to managing the pollution potentials of polyethylene terephthalate waste by utilizing it in the production of pavement stones, a practice that will likely help in managing PET waste since it will now serve as a resource in the construction industry. The

objectives of this research were to produce paving stone composites of sand and PET wastes as binder in different mix ratios, determine the compressive strengths of the composites and statistically compare results with conventional cement-sand paving stone.

III. MATERIALS AND METHOD

A. Materials

The materials used in the production process were;

1. Personal Protective Equipment: These are hand gloves, facemasks, cover all, safety boot, These PPEs are to protect various parts of the body from potential hazards
2. Melting Bowl: The melting bowl used was head pan and is needed to melt the PET waste to liquid form before adding sand and stirring to mix
3. Mixing Spatula: A wooden spatula for mixing the molten PET waste and sand during the heating process until desired mix is achieved.
4. Firewood: The source of energy needed to break down the polyethylene terephthalate wastes (PW's) aggregate into molten form before the fine aggregates (sand) are introduced.
5. PET Wastes: Plastic waste of varying sizes collected from dumpsites within the city of Yenagoa was cut into smaller sizes to aid the measurement
6. Fine Aggregates: This is one of the primary constituents involved in the production process. The sand was properly sieved to obtain the same particle as specified by ASTM C33.
7. Spent Engine Oil: This was used to grease the mold to avoid the mixture sticking.

B. Equipment

The equipment used were:

1. Weighing Scale: The scale was used to weigh the quantity of sand, the crushed polyethylene terephthalate waste and the composite paving stones.
2. Rebound Hammer Tester: The rebound hammer tester is a non-destructive concrete testing technique that offers a practical and quick estimate of the concrete's compressive strength. It is a concrete testing technique that adheres to ASTM C805 standards.
3. Mold: The mold was locally fabricated with wood for the purpose of this study. The dimension of the mold is 50 x 100 x 200 mm.

C. Paving Stone Composites Production Process

PET wastes (PWs) were manually harvested from dumpsites while a river sand collected from the sand dump in Swali, a community in Bayelsa State, Nigeria on the bank of River Nun. The PET wastes were thoroughly washed then shredded into smaller pieces to hasten the melting process. These composite materials were all transported to the Structure Laboratory in Civil Engineering Department, Niger Delta University.

The PET wastes were melted and mixed with river sand to form paving stone composites (PSCs) of PET-sand mix ratio of 1:3, labelled (PET: 10, 20, 30, 40 and 50%); and sand-cement mix of 1:3 labelled PET 0% as the control. The composite mix was transferred to an oiled mold and allowed to set. Six samples in three (3) replicates, were produced for this study. The control paving stones production were guided by ASTM C902 class MX specification for bricks intended to use as pavers for light vehicles, bikes and pedestrians. Each sample was well tampered during the casting stage and allowed to cure for a period of 28 days.

D. Laboratory Testing

The paving stone composites and control were taken to the laboratory for testing. The densities and their compressive strengths of the replicates of each sample were determined at 28 days. The mean values were then recorded.

E. Density

The weight and volume of samples measuring 50 x 100 x 200 mm used to determine the densities of each paving stone composites

Mathematically, the bulk density is calculated by the mass paving stone divided by the dimensional volume.

$$\text{Bulk Density} = \frac{\text{Mass (kg)}}{\text{Volum}(m^3)} \quad (1)$$

where:
M = Mass of paving stone
V = Dimensional volume of the paving stone (length breadth and thickness) in m^3.

F. Compressive Strength

The compressive test is described as the unit's capacity to sustain an axial load that is applied to the bed face, its edge, and/or the proportion of a sample's net area to the crushing load it can withstand and were carried out in accordance with ASTM C109. The rebound hammer test was used for the compressive strength test. It is a quick and efficient method of non-destructively determining the compressive strength of concrete. It is a method of evaluating concrete that complies with ASTM C805 requirements.

IV. RESULTS AND DISCUSSION

A. Density

The results of mean value for density of the paving stone composites at 28 days is shown in Figure 1. The cement-sand (PET 0) had the highest mean value of 2160 kg/m^3, while the mean values of PET-sand mix paving stone composites range from 1860 kg/m^3 to 1670 kg/m^3. The result shows a decreasing trend in the density of PET-sand mix paving stone composites mean values as the percentage of PET increases, and this can be attributed to the fact that cement is denser than PET. The result of the ANOVA test between the cement-sand and PET-sand samples, the mean densities were statistically analyzed using MS Excel and are shown in Table 1. Since the F(cal) is greater than the F(crit), and the P-value is lower than 0.05. It can be concluded that the difference in density between the cement-sand and PET-sand was significant. The implication is that the PET-sand are lighter and can be easily transported and have better workability, compared to the conventional paving stones.

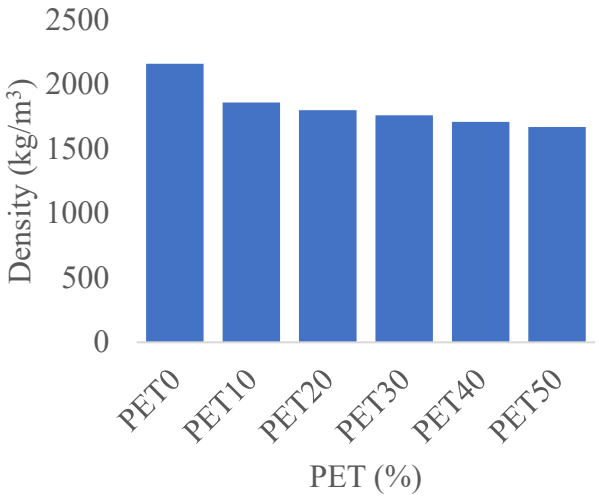

Figure 1: Comparison of PSCs mean densities and control

B. Compressive Strength

Figure 2 shows comparison of mean compressive strength of the paving stone composites (PSCs) and control at 28 days. Surprisingly, all the PSCs showed impressive compressive strengths with PET 30 % having highest mean value of 20.59 N/mm^2 while the control had the least mean compressive strength of 8.63 N/mm^2. This result means that the bond between PET and sand may be stronger than that of cement with regards to compressive strength.

Table 2 shows the results of Anova test between the control and PSCs mean compressive strength using MS Excel. Again, the F(cal) is greater than the F(crit), and the P-value is less than 0.05 it can be concluded that the difference in mean compressive strength between the control and PSCs were significant. Figure 1 shows a comparison of the mean compressive strengths of the control and the PSCs which indicates that the optimum PET-sand mix is 30 %. Hence, the utilization of PET waste as binders in the production of paving stones is feasible in terms of compressive strength.

Table 1: Analysis of variance (Anova) between the mean densities and control

Source of Variation	SS	df	MS	F	P-value	F crit
Between Groups	400000	1	400000	144.1441	2.136E-06	5.317655
Within Groups	22200	8	2775			
Total	**422200**	**9**				

Table 2: Analysis of variance (Anova) between the control and paving stone composites compressive strength.

Source of Variation	SS	df	MS	F	P-value	F crit
Between Groups	137.5668	1	137.5668	30.4137	0.000564	5.317655
Within Groups	36.1855	8	4.5232			
Total	173.7523	9				

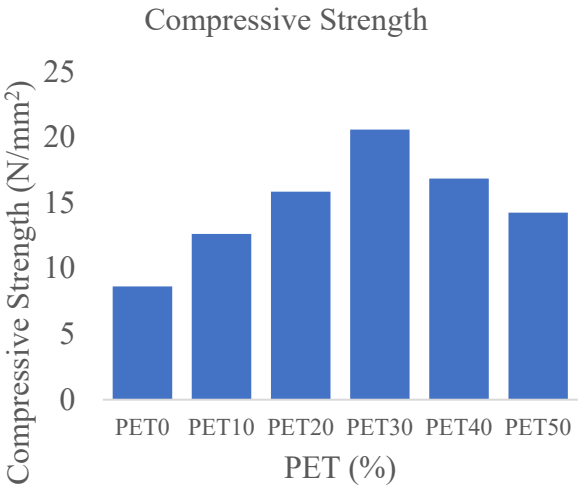

Figure 2**:** Comparison of the mean compressive strengths of the control and the

V. CONCLUSION

A. Conclusions

The conclusions from this study are that:

(1) The density of the control was higher than that of the PSCs and the higher the percentage of PET, the lighter the weight

(2) The PSCs recorded a higher value that the control for the compressive strength test.

(3) It is therefore established that PET waste can be best used as total cement replacement in the production of pavers.

B. Recommendations

The recommendations of this study are that:

1. the PSCs produced at 20 – 40 % PET are suitable for the construction of pedestrian paths, landscapes, and residential parking areas because it meets the minimum strength requirement for "class 4", for use of pedestrian walkways of 15N/mm^2.
2. Further study should be conducted on the chemical properties to help determine the performance of pavers when exposed to attacks from chemicals such as sulphate and chloride.

3. Furthermore, tests such as split tensile, flexural, impact resistant, abrasive, and soundness or durability should be conducted.
4. Tamping should be done properly, or a vibrating compressive machine should be used during production, especially when the sample is been discharged into the mold, to avoid the formation of air voids that might lower strength characteristics

REFERENCES

Agyeman, S., Obeng-Ahenkora, N.K., Assiamah, S., Twumasi, G. (2018) Exploiting recycled plastic waste as an alternative binder for paving blocks production. Case Study: Construction Material. Retri. From https://doi.org/10.1016/j.cscm.2019.e00246

Almeshal, I., Tayeh. B.A., Alyousef, R., Alabduljabbar, H., Mohamed, A.M. (2020) Eco-friendly concrete containing recycled plastic as partial replacement for sand. J Market Res 9(3):4631–4643. https://doi.org/10.1016/j.jmrt.2020.02.090

Alaloul, W.S., John, V.O., and Musarat, M.A. (2020). Mechanical and thermal properties of interlocking bricks utilizing wasted polyethylene terephthalate. International journal of concrete structures and materials. 14:24

ASTM C902. Standard Specification for Pedestrian and Light Traffic Paving Brick

ASTM C33. Standard Specification for Concrete Aggregates

ASTM C805 Standard Test Method for Rebound Number of Hardened Concrete.

ASTM C109. Standard Test Method for Compressive Strength.

Emeka, D and Lesley, H (2020). The Challenge of Plastic Pollution in Nigeria. Plastic Waste Recycling: Environmental Impact, Social Issues, Prevention, and Solutions. (pp. 569-583). Edition: 1st. Chapter: 22. Publisher: Elsevier.

Gharif, H.A., El, S. and Dan D.S. (2010). The effect of using various polyethylene fiber length concentrations of 1.6% on the properties of paving blocks with stone and silica fume. University of Gadjah Mada.

Gharif H.A, El, Sudarmoko, dan Djoko Suityo. Pengaruh Penggunaan Berbagai

Variasi Panjang Serat Polyethylene Konsentrasi 1,6% Pada Sifat-Sifat Paving Block

Dengan Batu dan Silica Fume. Universitas Gadjah Mada. (2010)

Gharif H.A, El, Sudarmoko, dan Djoko Suityo. Pengaruh Penggunaan Berbagai

Variasi Panjang Serat Polyethylene Konsentrasi 1,6% Pada Sifat-Sifat Paving Block

Dengan Batu dan Silica Fume. Universitas Gadjah Mada. (2010)

Gharif H.A, El, Sudarmoko, dan Djoko Suityo. Pengaruh Penggunaan Berbagai

Variasi Panjang Serat Polyethylene Konsentrasi 1,6% Pada Sifat-Sifat Paving Block

Dengan Batu dan Silica Fume. Universitas Gadjah Mada. (2010)

Puttaraj, M.H., Shanmukha, S., Navaneeth, R.P.G., and Prathima, T.B. (2018) Utilization of waste plastic in manufacturing of plastic-soil bricks. *International Journal of Technology Enhancements and Emerging Engineering Research,* 2(4):102–108.

Seghiri, M., Boutoutaou, D., Kriker, A., Hachani, M. (2017). The possibility of making a composite material from waste plastic. Energy Procedia 119:163–169.

Standar Nasional Indonesia (SNI) 03-0691-1996. Bata Beton (Paving Block). Badan Standardisasi Nasional. (1996).

Youcef, G., Bahia, R., Brahim S. and Rabah, C. **(**2014**)** "Use of sRecycled Plastic Bag Waste in the Concrete." *Journal of International Scientific Publications*: Materials, Methods and Technologies Volume 8, ISSN 1314-7269 (Online).

Zainab. Z.I., and Enas A.A. (2008) "Use of waste plastic in concrete mixture as aggregate replacement". Waste Management 28 (2008) 2041–2047.

Journal of Engineering, Emerging Technologies and Applied Sciences -– Volume 1 Issue 2, 2023

Available at ***https://www.ndu.edu.ng/journalofengineering/***

RESEARCH ARTICLE OPEN ACCESS

Soxhlet Extraction of Oil from Monkey Sugarcane (*Costus afer*) Leaves

B. E. Yabefa, W. Burubai, B. J. Jonathan

Department of Agricultural and Environmental Engineering,
Niger Delta University, Bayelsa State, Nigeria
branlyyabefa@yahoo.com

----------**********----------

Abstract:

Bio-oil is a mixture of organic components obtained from biomass components such as esters and amongst others, Soxhlet extraction is the most common method of bio-oil production from various feedstock. The aim of this study is to extract the bio-oil of monkey sugarcane leaves by a soxhlet extractor and examine the physicochemical properties. The average percentage of oil yield was 5.2% and a total weight of 26.09g of bio oil was extracted from 500g of dried Costus afer leaves. The physicochemical properties studied and results obtained using ASTM and other standards are; boiling point (125ºC), acid value (0.9mgKOH/g), FFA (0.49mgKOH/g), water content (0.53%), saponification value (146.3mgKOH/g), flash point 187ºC and pour point (5ºC). The bio-oil produced has comparable properties with that produced from other agricultural products and so could serve as a good feedstock for biodiesel production.

Keywords — **Monkey sugarcane, agbodou, soxhlet apparatus, oil extraction, methanol**

----------**********----------

I. INTRODUCTION

Bio-oil can be extracted from oleaginous plants, algae, municipal wastes or other organisms via different methods such as pyrolysis, soxhlet extraction method etc. which can be further used as feedstock for biodiesel production. Bio-oil is a complex mixture of organic components obtained from biomass components such as esters, alcohols, organic acids etc. The process of bio-oil extraction by the use of a soxhlet apparatus is one of the most conventional methods for vegetable oil extraction from materials that are oleaginous in nature (Ratna et al., 2015). Dried and particle size reduced samples which are weighed into a thimble in contact with the solvent for the oil to be moved from the solid matrix to the fluid medium. The solvent selection is based on the ultimate leaching properties of the sample. Oliveira et al., (2013) presented a report on the analysis of the mass transfer that takes place during solvent extraction in a packed column in a related study.

Franz von Soxhlet in 1879 invented the soxhlet extraction apparatus. Originally, it was designed to extract lipids from solid materials. This apparatus is normally used in situations where the solubility of the compound is limited in a particular solvent. Unmonitored operations while recycling a small amount of solvent to dissolve a larger amount of material is possible in this method. This apparatus has a percolator for solvent circulation, thimble that retains the solid to be extracted, siphon mechanism, which periodically empties the thimble. Much work has been done by different researchers on the use of soxhlet apparatus for the extraction of bio oil from different feedsocks. However, the main objective of this study is to examine the extraction process of bio oil from monkey sugarcane (Costus afer) leaves using the soxhlet extraction method to obtain the rate of oil yield and investigate the physicochemical properties of the bio-oil.

II. MATERIALS AND METHODS

A. Methods

The materials used in this study include; Fresh monkey sugarcane leaves, stopwatch, attrition mill, sieve shaker, sieves, soxhlet extraction apparatus, rotary evaporator, beakers, funnel, weight balance, plastic, distilled water, measuring cylinders, conical flask, spatula and, oven, methanol etc.

1. **Monkey Sugarcane Leaves (Costus afer)**: The leaves of monkey sugarcane were harvested from a nearby bush at Tantua in Amassoma community in Southern Ijaw Local Government Area, Bayelsa State, Nigeria. Amassoma is an Ijaw speaking community situated in Lat. 4.97oN, Long 6.11oE, and 79 meters above sea level. The samples were taken to the Processing Laboratory of Agricultural and Environmental Engineering, cleaned and oven dried at an average relative humidity of 65% and an average temperature of 60°C for a period of six (6) hour in the Processing Laboratory of the Agricultural and Environmental Engineering Department, Niger Delta University, Wilberforce Island Bayelsa State. The crispy leaves were then grinded and stored in air tight polyethene bags to prevent the absorption of moisture. Plate 1 presents the fresh monkey sugarcanes, Plate 2 and 3 present the grinding process and sieved monkey sugarcane leaves respectively.

Figure 1: Monkey sugarcane

Figure 2: Dry sieved monkey sugarcane leaves

2. **Extraction of Bio-Oil**: In this work, the extraction of the bio-oil was done with the soxhlet extraction apparatus from the monkey sugarcane (Costus afer) leaves, using methanol as solvent. In a soxhlet apparatus, the extractor thimble is fitted in between a round bottom flask at the bottom and a bulb condenser at the top. The monkey sugarcane leaves were properly dried and ground with the attrition mill and sieved with the 75-micron British Standard sieve size and kept at air tight environment (i.e. inside a nylon paper) to avoid moisture absorption before used for the study. The properly processed costus afer samples were used for the extraction. A dried thimble that was free from any form of visible impurities was weighed and then, 100 g of the sample was added into the thimble and weighed again. The 500 ml round bottomed flask which was also free from any form of visible impurities was also weighed and then, methanol was used to fill the 500 ml round bottomed flask up to 250ml of the flask, thereby making the feed to solvent ratio to be in line with the method used by Nibe et al., (2023).

The soxhlet extractor with a reflux condenser was fitted up and the heat source was adjusted to about 80oC so that the solvent boils gently and, this was allowed to siphon and left for about 30 minutes to 1 hour. The condenser was detached and the thimble was removed. The methanol was also allowed to siphon over the barrel before the condenser was detached. Then, a rotary evaporator was used to dry the flask that contains the oil at 80oC for a period of 30 seconds and cooled in a desiccator and then weighed. The thimble was placed in a beaker in an oven at 50oC and dried to constant weight with the sample (i.e. monkey sugarcane leaves powder), it was then cooled in a desiccator and weighed as was applied by Adegbe et al., (2016). The extraction was performed in triplicate using the soxhlet extraction apparatus, and the mean values and standard deviations were calculated based on equation (1) as presented by Ratna et al., (2015) to obtain the percentage oil extracted after the process of extraction.

$$\text{Percentage oil yield} = \frac{w_2}{w_1} \text{x } 100 \qquad (1)$$

where,
w_1 = weight of monkey sugarcane leave powder in grams
w_2 = weight of the oil produced in grams

Figure 3: Setting up Soxhlet extraction apparatus

Figure 4: Bio-oil extraction

Figure 5: Rotary evaporator for oil separation

Figure 6: Extracted monkey sugarcane bio-oil

III. RESULTS AND DISCUSSION

A. Bio Oil Extraction

Based on the experimentation for the bio oil extraction using the soxhlet apparatus as was also adopted by Nibe et al., (2023), the calculations of the oil yield from the monkey sugarcane leaves is presented in Table 4.1, where the mass of the sample collected par run, the mass of the dry sample after extraction, and the oil yield from each run of the sample denoted with M1 – M5. An average of 5.22g was obtained as mass of the oil yield and the average percentage of oil yield was 5.2%. Also, the average mass of the oven dried waste of the sample after extraction was 94.74g. A total volume of 26.09g of the bio oil was extracted from 500g of dried monkey sugarcane leaves as shown in Table 4.1. However, a total volume of 1000ml of the bio oil was extracted from the study.

Table 1: Bio-oil extraction result from monkey sugarcane (Costus afer) leaves

Sample ID	Weight of sample (g)	Weight of dry waste (g)	Weight of oil yield (g)	Percentage oil yield (%)
M_1	100	94.58	5.23	5.2
M_2	100	94.89	5.11	5.1
M_3	100	94.44	5.54	5.5
M_4	100	94.68	5.32	5.3
M_5	100	95.11	4.89	4.9
Total	500	473.7	26.09	26.0
Mean	100	94.74	5.22	5.2

B. Physiochemical Properties of Monkey Sugarcane (Costus Afer) Bio Oil

The quality of the bio-oil produced from the monkey sugarcane leaves was analyzed by evaluating physical and chemical properties of the bio oil are discussed and presented in Table 2. The boiling point which is an important property of a bio oil selection for biodiesel production was investigated in this study. The boiling point for the production of the monkey sugarcane leaves bio oil was 125°C as presented in Table 2. This value of the boiling point is lower than the boiling points obtained by Zahir et al., (2014) for corn oil and mustard oil which were reported as 140 and 170oC respectively. Due to the fact that oils are denser than water, it is therefore expected that the boiling point of monkey sugarcane is higher than that of water (100oC) which is in line with the reports presented by Zahir et al., (2014) in a similar study on corn oil.

Acid value as a property of bio oil for biodiesel production cannot be overemphasized. The volume of catalyst used in the transesterification reaction is dependent on the acid value of the bio oil. Hence, higher acid value will require more catalyst which will also increase the cost of biodiesel production process. The presence of high acid values in bio oil can lead to production of biodiesel with undesirable properties. The acidic impurities may affect the combination characteristics of biodiesel, which can contribute to engine deposit and enhance the corrosion of fuel system components. The acid value of the of the monkey sugarcane bio oil as presented in Table 2 is 0.9mgKOH/g which is lower, compared to bio oil from other agro-products such palm oil (4.217mgKOH/g) and tallow oil (1.113mgKOH/g).

Free fatty acid (FFA) value obtained for the monkey sugarcane leaves bio oil was 0.49mgKOH/g. Oils with high levels of FFA are more susceptible to oxidative aging, they become rancid more quickly. Patrick, (2013) reported that, base catalysed transesterification reaction requires low percentage of FFA of less than 1% for materials to be used as feedstock for biodiesel production.

Also the result of average percentage moisture content of the monkey sugarcane bio oil was 0.53%. This is also in conformity with the result obtained by other researchers in literature. High content of moisture in the bio oil can contribute to lower density, combustion reaction rate and corrosion tendencies. The result of the density test on the monkey sugarcane bio oil is 0.918 g/cm3. The density is a property that is normally used together with other physical properties to characterize the bio oil of a particular feedstock.

Saponification value describes the average molecular weight of the fatty acids present in specimen as triglycerides. Higher saponification value depicts lower average length of fatty acids, the higher the mean molecular weight of triglycerides and vice-versa. This study showed to have a saponification value of 146.3mgKOH/g. This value was lower compared to corn oil (153.8mgKOH/g) but higher than mustard oil (125.6mgKOH/g) as reported by Zahir et al., (2014).

Iodine numbers are often used to determine the amount of unsaturation in fats, oils and waxes. The iodine value obtained in this study was 11.4g. This value is lower than the value for corn oil (15.96g) but higher than that of mustard oil (8.10g) obtained by Zahir et al., (2014). Peroxide value gives the initial evidence of rancidity in unsaturated fats and oils. This study obtained a peroxide value of 0.35meq/kg. This value is seen to be higher than the peroxide value obtained by Zahir et al., (2014) for corn oil (0.162meq/kg) but lesser than the value for mustard oil (0.83meq/kg).

Also, the information on the ash content of a bio oil used for biodiesel production is very important because, the high ash content of the bio oil can contribute to the corrosion of the processing equipment used in biodiesel production. In this study, the ash content of the monkey sugarcane bio oil was obtained as 0.003%.

The flash point of the monkey sugarcane bio oil was 187oC and this result is lower compared to the result obtained by Demirbas, (2008) who used vegetable cooking oil as a feedstock and got a flash point of 212oC for the bio oil. This means that, the bio oil is less flammable, at lower temperature and is good and safe for handling operations.

The pour point of the monkey sugarcane bio oil was also investigated and the result was 5oC. The pour point of this study was also lower than that obtained by Demirbas, (2008) for waste cooking oil which was 10oC. Since, the pour point is the temperature below which a liquid loses its flow characteristics, the bio oils obtained in this study can therefore be suitable for use even in cold countries.

Table 2: Physcochemical Properties of the Bio-oil

S/No	Oil Properties	Value	ASTM
1.	Boiling point (°C)	125	
2.	Density (g/cm^3)	0.918	---
3.	Ash content (%)	0.003	D482
4.	Acid value (mgKOH/g)	0.90	D664
5.	Water content (%)	0.53	
6.	FFA (mg KOH/g)	0.49	
7	Saponification value (mgKOH/g)	146.3	
8.	Iodine value (g)	11.4	
8.	Peroxide value (meq/kg)	0.35	
9.	Flash point (°C)	187	D93
10.	Pour point	5	D97
11.	Kinematic Viscosity @ 40°C (mm^2/s)	41.5	D445
12	Ph	7.3	

C. Viscosity of Monkey Sugarcane Bio Oil

Viscosity is one of the fundamental qualities that characterize flow behavior of a fluid (Burubai and Amber, 2013). It is a measure of a fluid's ability to resist motion when a shearing stress is applied. The viscosity of the bio oil at ambient temperature, was tested using a rotary viscometer (BLS-8S model) at different spinning; 6, 12, 30, and 60 rpm, and the result is presented in milli-Pascal seconds as shown in Figure 7. It was observed that, the viscosity of the oil reduced with the increase in r.p.m of the spindle of the rotary viscometer. Hence, the oil contained can be described as a Non-Newtonian fluid (Burubai and Amber, 2013), specifically a shear-thinning fluid otherwise called a dilatant. They obey the power law model. Also, Figure 7 shows a curve for predicting the viscosity of the oil using power equation from the relationship between rpm and viscosity; the power equation on the graph can be used to predict the viscosity of the oil in mPa.s unit.

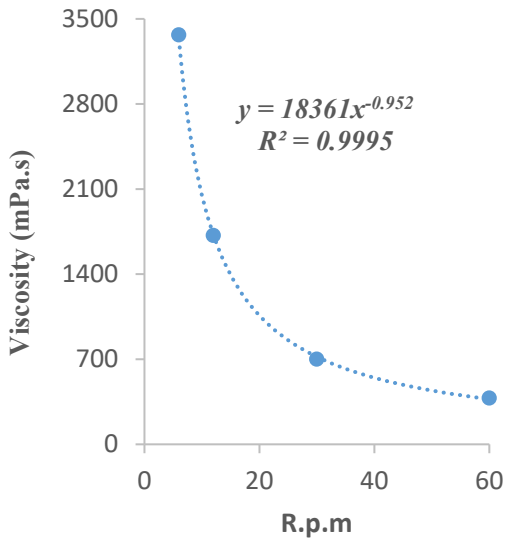

Figure 7: Relationship between rpm and viscosity

IV. CONCLUSION

The soxhlet extractor is a common laboratory device for the extraction of bio-oils from oleaginous materials. Application of this method for oil extraction from Costus afer showed an average mass of oil yield as 5.22g and the average percentage of oil yield was 5.2%. Also, the average mass of the oven dried waste of the sample after extraction was 94.74g. A total weight of 26.09g of the bio oil was extracted from 500g of dried monkey sugarcane leaves. The physicochemical properties obtained were; boiling point (125oC), acid value (0.9mgKOH/g), FFA (0.49mgKOH/g), water content (0.53%), saponification value (146.3mgKOH/g), flash point 187oC, pour point (5oC) and the pH value was 7.3.

REFERENCES

Nibe, R. L., Santosh, S., and Hinge, R. V. (2023). Extraction of Oil from Watermelon Seed using Soxhlet Extractor. *International Journal of Innovative Research in Technology (IJIRT).* Vol. 9, Issue 9, ISSN: 2349-6002, pp. 33-36.

Ratna, D., Ujjaini S., and Alakananda M. (2015). Soxhlet Extraction of Crotalaria Juncea Oil Using Cylindrical and Annular Packed Beds. *International Journal of Chemical Engineering and Applications.* Vol. 6, No. 2, Pp. 130-133.

Adegbe A. A., Larayetan R. A., and Omojuwa T. J. (2016). Proximate Analysis, Physicochemical Properties and Chemical Constituents Characterization of Moringa Oleifera (Moringaceae) Seed Oil Using GC-MS Analysis. *American Journal of Chemistry* 2016, 6(2): 23-28

Demirbas A. (2008): *Biodiesel: A realistic fuel alternative for diesel engines,* London, Great Britain: Springer. ISBN: 978-1-84628-994-1.

Patrick, B. (2013). Biodiesel Production from Selected Non Edible Feedstocks Using Unsupported Potassium Carbonate. M.Sc Thesis in the Department of Chemical Engineering, College of Engineering, Kwame Nkrumah University of Science and Technology. Page 1-228.

Burubai, W. and Ambah, B. (2013) Effects of Oven- Drying on the viscosity of okra (Abelmoschus esculentus). *Journal of Food Processing and Technology*, 4(11):287.

Zahir, E., Saeed, R., Hameed, M.A. and Yousuf, A. (2014). Study of physicochemical properties of edible oil and evaluation of frying oil quality by Fourier Transform-Infrared (FT-IR) Spectroscopy. *Arabian J. Chem.* DOI: 10.1016/j.arabjc.2014.05.025

Journal of Engineering, Emerging Technologies and Applied Sciences -– Volume 1 Issue 2, Nov. 2023

Available at ***https://www.ndu.edu.ng/journalofengineering/***

RESEARCH ARTICLE OPEN ACCESS

Application of Artificial Intelligence (AI) Model to Mitigate Security threats of Internet of Things (IoT): A Review

*Solomon Malcolm Ekolama, **David Ebregbe

*Department of Agricultural and Environmental Engineering, Niger Delta University, Bayelsa State, Nigeria

**Department of Electrical and Electronic Engineering, Niger Delta University, Bayelsa State, Nigeria

solomon.ekolama@ndu.edu.ng

----------**********----------

Abstract:

The convergence of the Internet of Things (IoT) and Artificial Intelligence (AI) is transforming data and technology exchange across a number of industries, including smart cities, transportation, healthcare, and agriculture. Adoption of IoT has transformed many industries, but it has also sparked worries about security flaws in network integrity, authentication, and data privacy. AI models have proven to be a pro-active and successful means to deal with these security issues in IoT networks. AI-based solutions are essential to mitigate security risks in Internet of Things settings because they include advanced features like behaviour analysis, anomaly identification, and threat prediction. This artificial intelligence (AI)-driven solutions improve behaviour analysis, anomaly detection, and real-time threat detection, protecting networks against cyberattacks and guaranteeing data security, privacy, and confidentiality. To maximise the benefits of AI in mitigating IoT security issues and fostering confidence in IoT technology, future efforts should concentrate on overcoming current limitations and challenges in AI for IoT security, exploring potential developments and research directions, and addressing ethical and regulatory considerations.

Keywords **— Internet of Things (IoT), Cyberattack, Artificial Intelligence (AI), Security threats, Authentication, Data privacy, Network integrity, Anomaly Detection, Predictive Analytics, Machine Learning Algorithms, Intrusion Detection Systems (IDS).**

----------**********----------

I. INTRODUCTION

The integration of Artificial Intelligence (AI) and the Internet of Things (IoT) is fundamentally changing the way we interact with data and technology, transforming sectors like healthcare, transportation, agriculture, and smart cities (Alahi et al., 2023). However, the widespread adoption of IoT has raised security concerns, including vulnerabilities in authentication, data privacy, and network integrity (Chanal & Kakkasageri, 2020). The use of AI models to mitigate these issues has gained prominence as a proactive and effective approach to addressing these security issues in IoT ecosystems (Malhotra et al., 2012).

A network of interconnected devices, sensors, and systems that exchange information and communicate via the internet constitutes the Internet of Things (IoT). For the purposes of real-time monitoring, predictive analytics, and automated decision-making, it has produced enormous quantities of data. Nevertheless, IoT devices are susceptible to cyber threats such as denial-of-service attacks, unauthorised access, and data intrusions due to their interconnectedness.

Models based on artificial intelligence (AI) are indispensable for mitigating security threats in IoT environments (Zaman et al., 2021). They provide sophisticated functionalities such as the ability to detect anomalies, analyse behaviour, and predict threats. Machine learning algorithms are capable of

analysing immense amounts of data, detecting anomalous patterns, and mitigating cyber threats in real time (Inuwa & Das, 2024). In addition to bolstering the resilience of IoT ecosystems, authentication mechanisms, access control policies, and encryption techniques powered by AI ensure the integrity of data and the reliability of systems.

II. ROLE OF ARTIFICIAL INTELLIGENCE IN CYBERSECURITY

Artificial intelligence (AI) is playing a crucial role in the Internet of Things (IoT) by improving threat identification, anomaly detection, and predictive analytics as shown in Figure 1.

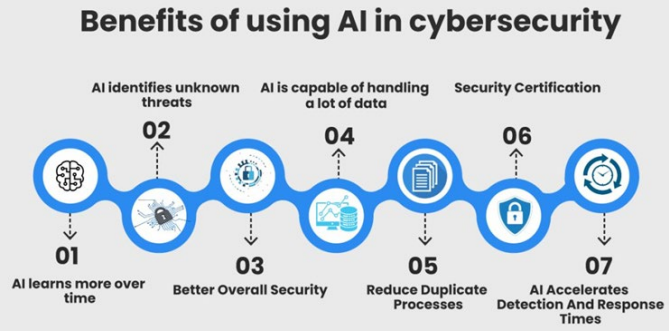

Figure 1: AI in Cyber Security and IoT. (Source: Augmented AI, 2023)

As shown in Figure 1, AI systems use machine learning methods like reinforcement learning, supervised learning, and unsupervised learning to analyse large data volumes, identify security risks, monitor network traffic, flag suspicious activity, and trigger automatic responses to combat cyberattacks. AI-driven authentication and encryption systems ensure the confidentiality, availability, and integrity of sensitive information.

Artificial intelligence (AI) is increasingly crucial in protecting data on the Internet of Things (IoT). AI uses behaviour analysis, threat detection, and automatic response mechanisms to enhance cybersecurity. Machine learning algorithms help identify patterns, outliers, and security breaches in large amounts of data. AI also enhances privacy, secrecy, and security through authentication systems, encryption technologies, and access control rules.

Artificial intelligence (AI) is playing a crucial role in cybersecurity in IoT settings by providing real-time threat detection, anomaly detection, and behaviour analysis. Intrusion detection systems (IDS) protect networks from cyberattacks by monitoring traffic and identifying suspicious behaviors. AI-driven authentication methods, encryption techniques, and access control rules enhance data security, privacy, and confidentiality. AI-powered predictive analytics and threat intelligence help firms anticipate potential dangers and strengthen their security in the evolving IoT environment.

III. SECURITY THREATS OF IOT DEVICES: CHALLENGES AND AI SOLUTIONS

Enhancing security resilience of IoT ecosystems can be achieved through the implementation of Artificial Intelligence (AI) models that perform proactive threat detection, anomaly identification, and automated response mechanisms. This can effectively mitigate the security risks associated with IoT devices, such as unauthorised access and data breaches as shown in Figure 2.

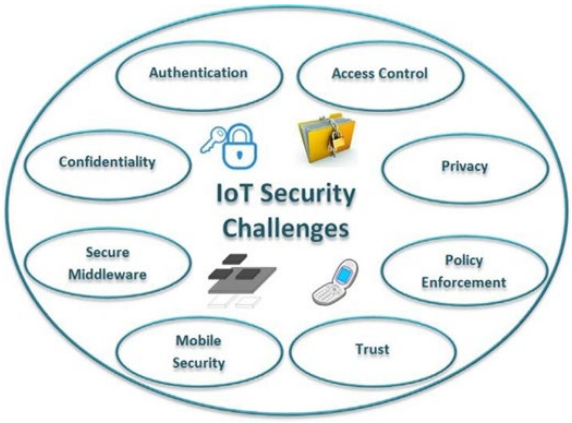

Figure 2: Security Challenges of IoT (Source: Torğul et al., 2016)

The following are some areas of security concerns shown in Figure 2 and suggested solutions using artificial intelligence:

A. Weak Authentication and Authorization

Challenges: IoT devices pose security risks due to flaws in authorization and authentication protocols, allowing unauthorised access and credential theft (Tawalbeh et al., 2020). Insufficient authorization mechanisms can lead to breaches and data compromises. The fragmented and decentralised structure of IoT ecosystems complicates these issues.

Solution: AI-based access control and authentication can be employed to improve security on IoT devices by reducing flaws in traditional systems. AI algorithms also minimise unauthorised access and credential theft, enabling authentic permission management based on user behaviour and risk assessment scores (Wu et al., 2020). AI also ensures Real-time monitoring of suspicious activity and potential breaches improves security. Integrating AI increases resilience and protects IoT ecosystems from evolving cyber threats.

B. Insecure Network Connections

Challenges: IoT devices with insecure network connections run the risk of serious security breaches due to data interception, man-in-the-middle attacks, and eavesdropping (Hasan et al., 2022). Because of shoddy authentication procedures, poor encryption techniques, or incorrectly configured network settings, these vulnerabilities are susceptible to malevolent actors' exploits. Strong encryption standards, safe communication protocols, frequent security audits, and network traffic monitoring are required for IoT device protection.

Solution: AI-driven network security solutions protect IoT devices from security threats, especially insecure connections. By continuously monitoring and analysing network traffic patterns, AI algorithms detect anomalies, potential threats, and data breaches (Abed & Anupam, 2023). Real-time intrusion detection systems respond to suspicious activities, while encryption and authentication mechanisms ensure data confidentiality. Machine learning algorithms adapt to evolving attack vectors.

C. Lack of Firmware Updates

Challenges: IoT devices without firmware upgrades pose security and operational risks due to potential vulnerabilities that can allow hackers to steal data or conduct cyberattacks (Djenna et al., 2021). Frequent updates deprive devices of crucial security patches, bug fixes, and performance improvements, making it challenging to adapt to changing threats and maintain peak efficiency. Proactive measures like secure update systems, vendor cooperation, and user education are necessary.

Solution: By examining firmware code, finding vulnerabilities, and ranking security fixes, AI-powered firmware security and vulnerability management may assist IoT devices in addressing security threats. Firmware integrity is ensured by machine learning techniques that can identify unusual behaviour in firmware upgrades. Predictive analytics powered by AI is able to foresee new risks and provide countermeasures (Shrivastwa, 2023). By incorporating AI into firmware security procedures, security resilience is increased, risks related to obsolete firmware are reduced, and ongoing defence against prospective attacks is guaranteed.

D. Data Privacy Concerns

Challenges: The Internet of Things (IoT) faces a significant challenge in terms of data privacy due to inadequate security measures. IoT devices collect vast amounts of sensitive data, such as user behaviour and health information, without safeguards, putting user security and privacy at risk. Comprehensive solutions, including robust encryption protocols, data anonymization methods, access control mechanisms, and privacy-first design principles, can help protect user data.

Solution: Encryption and data privacy strategies powered by artificial intelligence can assist

organisations in addressing privacy concerns in Internet of Things installations. These solutions implement strong encryption methods using AI algorithms, thereby thwarting unauthorised access and data breaches. By analysing user behaviour and data trends, machine learning algorithms can detect privacy issues, allowing for preventative measures such as data anonymisation and differential privacy strategies. Implementing AI-driven strategies improves the resilience of security and data protection measures (Kavitha et al., 2021).

E. Physical Security Risks

Challenges*:* IoT device physical security vulnerabilities present a substantial risk to the integrity of network infrastructure and the protection of data. Physical theft, inadequate device hardening, and the absence of intrusion detection measures are a few examples. These vulnerabilities can be exploited by cybercriminals to acquire sensitive data, compromise the functionality of devices, or obtain unauthorised access (Garagad et al., 2020).

Solution: IoT device security may be greatly improved by using AI-powered physical security measures. AI algorithms are used by sophisticated surveillance systems to instantly identify abnormalities and assess dangers. While machine learning algorithms find new dangers and vulnerabilities in security data, video analytics set off automatic responses and alerts. Authorised personnel may access vital sites and Internet of Things equipment with the help of technologies like biometric identification and AI-driven access control (Awad et al., 2024).

F. Botnets and DDoS Attacks

Challenges*:* The rise of botnets and DDoS attacks on IoT devices poses a significant security challenge due to their numerous vulnerabilities and lack of security measures. These attacks can overload networks and disrupt services. Identifying and preventing botnet attacks is challenging due to the complexity of IoT installations (Salim et al., 2020).

Solution: To mitigate these threats, AI can help organisations mitigate security risks associated with IoT devices, such as botnets and DDoS attacks. AI-driven threat detection systems monitor network traffic and device activity, triggering real-time warnings and automatic reactions. Machine learning algorithms can adapt to changing attack vectors, reducing botnet and DDoS attacks' impact on IoT ecosystems. Integrating AI-driven capabilities strengthens security measures, increases threat visibility, and proactively protects against advanced cyber threats (Chakraborty et al., 2023).

G. Supply Chain Vulnerabilities

Challenges: The security of IoT devices is a complex issue due to the interconnected nature of supply chains, which involve stakeholders like device makers, component suppliers, software developers, and third-party vendors. Vulnerabilities can arise from supply chain attacks, corrupted components, or malicious firmware changes. The global supply chain environment complicates ensuring resilience against cyber-attacks and assessing component security posture (Sobb et al., 2020).

Solution: Artificial intelligence (AI) can improve the security of Internet of Things devices by addressing supply chain vulnerabilities. AI-powered algorithms can evaluate component safety, identify irregularities, and identify potential threats. Real-time monitoring, anomaly detection, and automated reaction mechanisms minimise security risks. Machine learning algorithms can improve cyber resilience by learning from past data and suggesting preventative measures. AI-driven security systems enhance integrity, protect devices from breaches, and improve visibility and accountability, ultimately enhancing trustworthiness in connected ecosystems (Nagaty, 2023).

H. Integration Challenges

Challenges*:* The integration of IoT devices poses significant security risks due to the variety of

devices, protocols, platforms, and settings. Adopting complete security frameworks and consistent procedures is challenging due to compatibility issues, interoperability hurdles, and a lack of standardised protocols (Jurcut et al., 2020).

Solution: AI-powered integration solutions enhance IoT device integration, reducing complexity and human involvement. They automate device identification, setup, and administration, detecting irregularities and security breaches in real-time. These solutions enable proactive threat detection and automatic response mechanisms, centralised monitoring, and the enforcement of security regulations. They enhance interoperability and security resilience, responding to changing IoT settings and ensuring ongoing compliance with security standards (Alahi et al., 2023).

IV. CASE STUDIES AND EXAMPLES

AI-driven solutions enhance IoT ecosystem security by monitoring network traffic, analysing data trends, and triggering automatic responses. They protect sensitive information through authentication, encryption, and access rules, enabling predictive analytics and threat intelligence. This is demonstrated by following case studies:

a. "*Fraudsters Used AI to Mimic CEO's Voice in Unusual Cybercrime Case*"

Fraudsters laundered €220,000 ($243,000) in Europe in March 2019 by assuming the identity of the CEO of a United Kingdom-based energy company. The CEO believed he was discussing with the CEO of his German parent company, who instructed him to transfer the funds within an hour, as shown in figure 3. The organisation's insurance provider, Euler Hermes Group SA, concealed the identities of the victim companies. It is unknown whether this is the first occurrence of an attack of this nature, but law enforcement officials and AI researchers assert that criminals will use AI to automate cyberattacks (Stupp, 2019).

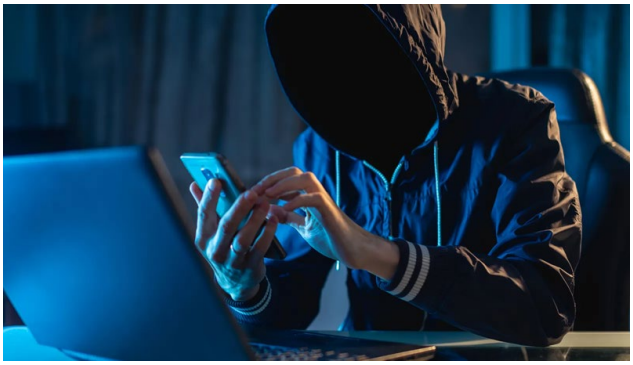

Figure 3: Vishing Attack (Source: Damiani, 2019)

b. "*IoT Vulnerabilities and Attacks: SILEX Malware Case Study*"

The Internet of Things (IoT) connects physical items to a digital environment, with 64 billion devices expected to be connected by 2025. However, this rapid growth has led to new cyber threats, particularly in Industrial IoT (IIoT), where cybercriminals exploit weaknesses to launch DDoS attacks. The SILEX virus, an asymmetric cyberthreat, targets IoT devices with default passwords. To mitigate IoT risks, strong authentication, frequent updates, security awareness, supply chain security, and incident response procedures are necessary. Future research will focus on lightweight SILEX malware mitigation and AI-based security solutions (Mukhtar et al., 2023).

V. STATISTICS OF FINANCIAL LOSSES TO IOT CYBERATTACKS

While the Internet of Things (IoT) has significantly advanced many industries, it has also raised cybersecurity threats and resulted in financial losses from cyberattacks, as seen in Figure 4.

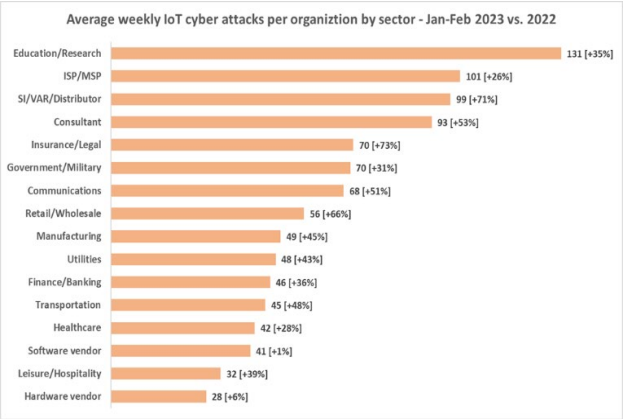

Figure 4: Statistic of IoT Cyberattacks Losses (Source: Check Point, 2023)

IoT hacks have a shocking financial effect, according to recent statistics (Hacker, 2019). Global financial damages from IoT-related cyber-attacks reached over $11.8 billion in 2020 alone. This figure illustrates the expanding risk surrounding IoT devices and shows a significant rise from previous years (Özdemir & Hekim, 2018).

The extensive use of connected devices in many businesses is one of the main causes of the significant financial losses linked to IoT hacks. The growth of IoT devices has increased the attack space for hackers, from wearables and smart homes to industrial IoT systems and smart city infrastructure. Because of this, both people and companies are susceptible to a variety of cyberthreats, such as ransomware attacks, botnet attacks, and data breaches.

IoT hacks have the potential to cause significant financial losses, especially in the healthcare industry. Healthcare organisations reported financial damages from cyber events involving medical IoT devices of an estimated $13.8 billion in 2021. These assaults not only cause financial losses but also seriously jeopardise patient safety and data privacy, underscoring the vital need for implementing strong cybersecurity safeguards in healthcare IoT installations.

Manufacturing is another area that has been severely attacked by IoT hacks. Industrial IoT (IIoT) devices are being used more and more in manufacturing facilities for automation and data analytics, making them attractive targets for hackers. Manufacturing businesses reported losses from IoT-related cyber-attacks in 2022 that exceeded $9.5 billion (Bharati & Podder, 2022). These disruptions—which highlight the need for cybersecurity resilience in industrial environments—include supply chain interruptions, manufacturing outages, and intellectual property theft.

IoT cyber risks have resulted in major financial losses for the financial services sector as well. Financial institutions suffered losses from cyberattacks that targeted Internet of Things equipment, including ATMs, payment terminals, and banking apps, in 2020, amounting to over $7.2 billion (Pomerleau & Lowery 2020). These attacks demonstrate the necessity for constant monitoring and strong security measures in financial IoT networks. They vary from credential theft and fraudulent transactions to network intrusions.

In conclusion, the data pertaining to monetary losses resulting from Internet of Things hacks presents a worrisome image of the expanding influence of cyberthreats on organisations and people around the globe. As IoT installations continue to spread across companies, preventing financial losses and protecting vital systems and data require tackling cybersecurity issues and putting proactive defence plans in place.

VI. CHALLENGES AND FUTURE DIRECTIONS

With the proliferation of internet-connected devices (IoT) and the acceleration of technological advancements (Figure 5), experts predict that the number of internet-connected devices might reach 75 billion by 2025.

This shows that the use of artificial intelligence (AI) models to address security challenges in the Internet of Things (IoT) will face challenges due to the complexity and diversity of IoT ecosystems, and the vested interest of cyber fraudsters. In the future, AI must be employed as shown in figure 6 to address

specific areas to maximise the benefits of AI in mitigating IoT security issues.

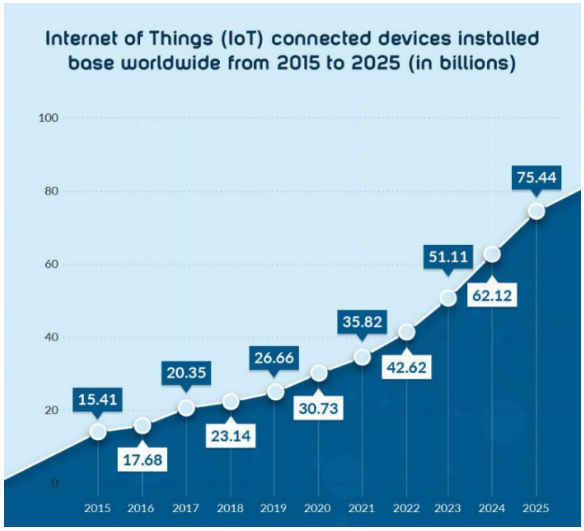

Figure 5: IoT Inter-Connected Devices by 2025 (Source: Marktechpost, 2021)

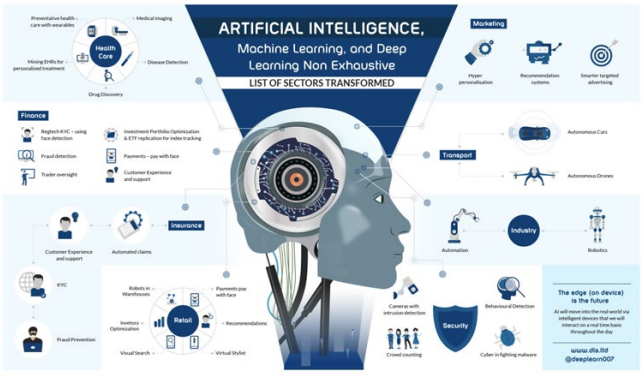

Figure 6: AI in Future of IoT (Source: Marktechpost, 2021)

Some of the areas of concern to be addressed are as follows:

1. ***Current limitations and challenges in applying AI to IoT security***: Complex IoT ecosystems, interoperable AI solutions, and standardised security frameworks are all obstacles that AI for IoT security must overcome. Challenges are encountered by real-time threat detection and AI algorithms as a result of restricted power and resource availability. AI for IoT is fostering industry collaboration on standardised security frameworks, optimising energy-efficient algorithms, and developing lightweight AI models in order to address these challenges. This could ensure a more secure future through enhanced security resilience, proactive threat detection, and dependable IoT installations.

2. ***Potential future developments and research directions:*** Scalability, interoperability, data privacy, security, and regulatory compliance are some of the obstacles that the IoT must overcome. Strong encryption to protect personal information and standardised protocols to ensure smooth communication are essential. Improvements in security may be achieved in the future by investigating new technologies such as blockchain, 6G networks, and edge computing. Algorithms for automated decision-making and predictive analytics are being created using artificial intelligence and machine learning. We are actively seeking sustainability initiatives and energy-efficient solutions to lessen the environmental effects of Internet of Things (IoT) installations.

3. ***Ethical and regulatory considerations:*** Ensuring data privacy, security, and transparency in IoT technologies while adhering to legal requirements like CCPA and GDPR is challenging. Ethical issues include addressing biases in AI systems, fair decision-making processes, and defending user rights. Future steps involve developing ethical AI frameworks, encouraging responsible data practices, and fostering cooperation between business, academia, and regulatory organizations. Improving user knowledge, permission procedures, and data security safeguards is crucial for fostering confidence in IoT technology.

VII. CONCLUSION

Artificial intelligence (AI) is being increasingly used in Internet of Things (IoT) security to improve cybersecurity by analyzing behavior, identifying

threats, and implementing automatic reactions. This technology enhances real-time vulnerability identification, mitigation, defence strengthening, and protection against evolving cyberattacks.

AI models offer advanced features like automatic reaction mechanisms, threat detection, anomaly detection, behaviour analysis, and real-time risk mitigation.

Future research should focus on AI-driven threat intelligence predictive analytics, lightweight AI models, industry-academia collaboration, and ethical and regulatory concerns related to AI security implementations.

REFERENCES

Alahi, M. E. E., Sukkuea, A., Tina, F. W., Nag, A., Kurdthongmee, W., Suwannarat, K., & Mukhopadhyay, S. C. (2023). Integration of IoT-enabled technologies and artificial intelligence (AI) for smart city scenario: recent advancements and future trends. Sensors, 23(11), 5206.

Augmented AI, (2023). The Role of Artificial Intelligence in Cybersecurity | How AI Enhances Protection. Retrieved from https://www.augmentedstartups.com/blog/the-role-of-artificial-intelligence-in-cybersecurity-how-ai-enhances-protection.

Internet of Things and artificial intelligence-driven solutions. Security and Privacy, 6(3), e285.

Alahi, M. E. E., Sukkuea, A., Tina, F. W., Nag, A., Kurdthongmee, W., Suwannarat, K., & Mukhopadhyay, S. C. (2023). Integration of IoT-enabled technologies and artificial intelligence (AI) for smart city scenario: recent advancements and future trends. Sensors, 23(11), 5206.

Awad, A. I., Babu, A., Barka, E., & Shuaib, K. (2024). AI-powered biometrics for Internet of Things security: A review and future vision. Journal of Information Security and Applications, 82, 103748.

Bharati, S., & Podder, P. (2022). Machine and deep learning for iot security and privacy: applications, challenges, and future directions. Security and communication networks, 2022, 1-41.

Chakraborty, A., Biswas, A., & Khan, A. K. (2023). Artificial intelligence for cybersecurity: Threats, attacks and mitigation. In Artificial Intelligence for Societal Issues (pp. 3-25). Cham: Springer International Publishing.

Chanal, P. M., & Kakkasageri, M. S. (2020). Security and privacy in IoT: a survey. Wireless Personal Communications, 115(2), 1667-1693.

Check Point, (2023). The Tipping Point: Exploring the Surge in IoT Cyberattacks Globally. Retrieved from https://blog.checkpoint.com/security/the-tipping-point-exploring-the-surge-in-iot-cyberattacks-plaguing-the-education-sector/

Damiani, J. (2019). A Voice Deepfake Was Used To Scam A CEO Out Of $243,000. Forbes. Retrieved from https://www.forbes.com/sites/jessedamiani/2019/09/03/a-voice-deepfake-was-used-to-scam-a-ceo-out-of-243000/?sh=573e64932241. 26 March, 2024

Djenna, A., Harous, S., & Saidouni, D. E. (2021). Internet of things meet internet of threats: New concern cyber security issues of critical cyber infrastructure. Applied Sciences, 11(10), 4580.

Garagad, V. G., Iyer, N. C., & Wali, H. G. (2020, July). Data integrity: a security threat for internet of things and cyber-physical systems. In 2020 International Conference on Computational Performance Evaluation (ComPE) (pp. 244-249). IEEE.

Hacker, J. S. (2019). The great risk shift: The new economic insecurity and the decline of the American dream. Oxford University Press.

Hasan, M. K., Ghazal, T. M., Saeed, R. A., Pandey, B., Gohel, H., Eshmawi, A. A., ... & Alkhassawneh, H. M. (2022). A review on security threats, vulnerabilities, and counter measures of 5G enabled Internet-of-Medical-Things. IET communications, 16(5), 421-432.

Inuwa, M. M., & Das, R. (2024). A comparative analysis of various machine learning methods for anomaly detection in cyber-attacks on IoT networks. Internet of Things, 101162.

Jurcut, A., Niculcea, T., Ranaweera, P., & Le-Khac, N. A. (2020). Security considerations for Internet of Things: A survey. SN Computer Science, 1, 1-19.

Kavitha, S., Bora, A., Naved, M., Raj, K. B., & Singh, B. R. N. (2021). An internet of things for data security in cloud using artificial intelligence. International Journal of Grid and Distributed Computing, 14(1), 1257-1275.

Malhotra, P., Singh, Y., Anand, P., Bangotra, D. K., Singh, P. K., & Hong, W. C. (2021). Internet of things: Evolution, concerns and security challenges. Sensors, 21(5), 1809.

Marktechpost, (2012). The Future Direction and Vision for AI. Retrieved from https://www.marktechpost.com/2021/11/05/the-future-direction-and-vision-for-ai/

Mukhtar, B. I., Elsayed, M. S., Jurcut, A. D., & Azer, M. A. (2023). IoT vulnerabilities and attacks: SILEX malware case study. Symmetry, 15(11), 1978.

Nagaty, K. A. (2023). Iot commercial and industrial applications and AI-powered IoT. In Frontiers of Quality Electronic Design (QED) AI, IoT and Hardware Security (pp. 465-500). Cham: Springer International Publishing.

Özdemir, V., & Hekim, N. (2018). Birth of industry 5.0: Making sense of big data with artificial intelligence,"the internet of things" and next-generation technology policy. Omics: a journal of integrative biology, 22(1), 65-76.

Pomerleau, P. L., & Lowery, D. L. (2020). Countering Cyber Threats to Financial Institutions. A Private and Public Partnership Approach to Critical Infrastructure Protection. Springer.

Salim, M. M., Rathore, S., & Park, J. H. (2020). Distributed denial of service attacks and its defenses in IoT: a survey. The Journal of Supercomputing, 76, 5320-5363.

Shrivastwa, R. R. (2023). Enhancements in Embedded Systems Security using Machine Learning (Doctoral dissertation, Institut Polytechnique de Paris).

Sobb, T., Turnbull, B., & Moustafa, N. (2020). Supply chain 4.0: A survey of cyber security challenges, solutions and future directions. Electronics, 9(11), 1864.

Stupp, C. (2019). Fraudsters Used AI to Mimic CEO's Voice in Unusual Cybercrime Case. Retrieved from https://www.wsj.com/articles/fraudsters-use-ai-to-mimic-ceos-voice-in-unusual-cybercrime-case-11567157402. 26 March, 2024.

Tawalbeh, L. A., Muheidat, F., Tawalbeh, M., & Quwaider, M. (2020). IoT Privacy and security: Challenges and solutions. Applied Sciences, 10(12), 4102.

Torğul, B., Şağbanşua, L., & Balo, F. B. (2016). Internet of things: a survey. International Journal of Applied Mathematics Electronics and Computers, (Special Issue-1), 104-110.

Wu, H., Han, H., Wang, X., & Sun, S. (2020). Research on artificial intelligence enhancing internet of things security: A survey. Ieee Access, 8, 153826-153848.

Zaman, S., Alhazmi, K., Aseeri, M. A., Ahmed, M. R., Khan, R. T., Kaiser, M. S., & Mahmud, M. (2021). Security threats and artificial intelligence based countermeasures for internet of things networks: a comprehensive survey. Ieee Access, 9, 94668-94690.

Journal of Engineering, Emerging Technologies and Applied Sciences -– Volume 1 Issue 2, Nov. 2023

Available at ***https://www.ndu.edu.ng/journalofengineering/***

RESEARCH ARTICLE OPEN ACCESS

Relay Coordination for Efficient Power Delivery and Equipment Protection at Station Road, Port-Harcourt

Benjamin Ayibapreye*, Nduka Watson Aguiyi **

*Department of Electrical/Electronic Engineering, Niger Delta University, Wilberforce Island, Bayelsa State, Nigeria.
Email: ayibapreyebenjamin@ndu.edu.ng

**Department of Electrical/Electronic Engineering, Federal University Otuoke, Otuoke, Bayelsa State, Nigeria.
Email: aguiyinw@fuotuoke.edu.ng

----------**********----------

Abstract:

Incorrect operation of protective devices in a power system can result in massive equipment damage, human casualties, and even power supply disruption. This research is to address the problem of wrong sequence of operation of relays and circuit breakers at the Station Road network. Short circuit analysis was performed using ETAP 19.0 to study the behavior of the network in the event of fault. Additionally, Inverse Definite Minimum Time (IDMT) is used to ensure quick response of the protective devices. In this study, the response times of the four relays are investigated when a 3-phase fault is injected into the feeder network. The findings reveal that the tripping sequence response from feeder breaker to 33kV line breaker to 33kV control panel breaker and finally to 11kV incomer control panel, are abnormal. The result of the improved scenario shows the relays tripping sequence are in the proper order from the main feeder to the 11kV incomer control panel, 33kV control panel breaker, and 33kV line breaker, with proper time grading. It is crucial to achieve the right order of relay operation for efficient protection and service delivery.

Keywords — **Relay coordination, efficient power delivery, equipment protection**

----------**********----------

I. INTRODUCTION

An electric power system is a network of electrical devices used for generation, transmission and distribution of electricity, with the objective to match customer expectations for the delivery of steady and reliable power supply free of unfavorable impacts from outages (A. Watson & A. Benjamin, 2022). This objective is constrained by the effectiveness and quality of the protections available to the various connecting networks of the power system. The security of a power network is the duty of a power system Engineer by using the right equipment for constant monitoring of the system to ensure maximum electrical supply continuity while avoiding equipment damage (M. H. Hussain, I. Musirin, S. R. Rahm, A. Abidin, A. F., & A. Azmi, 2013). Generally, relays are widely used for the protection of power systems, and are made to detect different currents during the same fault in different locations, and initiate the isolation of the faulted section.

When a fault in an electrical circuit is detected, a protective relay analyses operating conditions on the circuit and trips circuit breakers. The protection engineer evaluates the tripping characteristics of the different protective relays and design effective protective scheme (K. O. Uwho, H. N. Amadi, & P. Obire, 2022). Relays should be designed to detect abnormal or undesirable situations and deliver a tripping signal to the circuit breaker in order to separate the affected area without affecting adjacent sections. Statistics show that many relay trips are caused by wrong or poor settings rather than real failure (U. C. Ogbuefi, B. O. Anyaka, & M. J. Mbunwe, 2019). The primary devices nearest to the fault should be the first to respond, followed by backup devices further away to isolate the faulty

section only. This is necessary to meet the basic statutory objective of every electrical energy provider for the provision of continuous, acceptable and reliable service to its customers. Therefore, if there is fault in the system, fault analysis process consisting of calculation of the maximum currents that components and switching devices must sustain and interrupt, and circuit protection coordination, is carried out.

Generally, relay coordination can be said to be determination of the sequence of relay operations for each potential fault location in order to quickly isolate the faulty section and to ensure adequate coordination margins (B, Dinesh, M. Rudra, P. Gupta, & H. Om 2005). Therefore, power system relay coordination is the tendency of the power system is remaining in operation after isolation of identified potential fault. Relay coordination problems have attracted a lot of attention in recent times with emphasis on control, planning and operation of the system. The issues of the power system are raising a lot of concern with increasing demand for power and loading of the transmission system.

In this paper, the relay coordination problem of relays and circuit breakers at the Station Road network is investigated. The investigation is centered on the response time of the relays, the tripping sequence response of the breakers and the order of the relay and breaker operation.

II. OPERATION OF PROTECTIVE RELAY

Figure 1 shows the fundamental circuit breaker control network for opening action. The relay is attached to current transformer (CT) and the potential transformer (PT) to actuates and close the contacts when a fault occurs within the secured section. When the breaker trip coil is engaged, the breaker working mechanism will be on to activate opening action by allowing current to the trip circuit. The relay is responsible for the activation of the trip circuit, and the faulty section is removed by the circuit breaker.

Overcurrent relays (OCRs) which operates at a fixed fault current level are among the most used protective components in power system. To arrive at effective protection from these defensive tools, the pickup current and the time-dial setting of the relay must be regulated to ensure that the system perfectly coordinated. The relay operates when the fault current reaches a value equal to or greater than the pickup current. The overcurrent device's inverse characteristics are changed by modifying the time delay via the time dial setting.

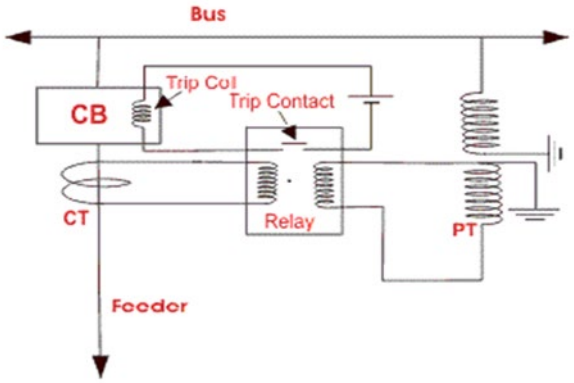

Figure 1: Basic Circuit Diagram of Protective Relay Scheme. Source: (Jayaprakash, J., Angelin, M., & Lakshmi, J. 2016).

Generally, during system design, the fault current calculation is used to determine the coordination of this protective relay (P. Obire, D. C. Idoniboyeobu, & S. L. Braide, 2022). The location and type of equipment to be secured are the most important selectivity criteria. Distance relays are usually applied for long-distance transmission lines, differential relays for transformer protection, directional overcurrent relays for meshed networks, OCRs for generators, motors, and feeders, and pilot relays for long-distance, switching in hazardous areas, cable, and power equipment protection.

A. Short Circuit Analysis

When there is difference in potential between two points in a network, a low impedance connection can be made intentionally or accidentally which is abnormal (O.N. Igbogidi, D. C. Idoniboyeobu, & S. L. Braide, 2018). Its effect causes flow of excessive current through the power system, resulting in power

outages. Even though the power system is built to defend against numerous problems, it is somehow harmed. The voltage and configuration of the power circuit, the method of neutral connections whether solidly grounded, resistance grounded, reactance grounded, and ungrounded, the presence of regulating devices such as shunt reactors, series reactors, shunt and series capacitors, and the speed with which the faulted circuit section is disconnected determine the fault current.

Short circuit analysis can be deployed to evaluate fault current in a power system for various faults. Apart from short circuit current, it can as well be used to assess the interrupting ratings of protective devices such as circuit breakers and fuses for assuring the protection of equipment installed in the power system, as well as protective device coordination (P. Obire, D. C. Idoniboyeobu, & S. L. Braide, 2022). If an electrical fault interrupts at a rate faster than the protective device's interrupting rate, the equipment will be severely damaged. As a result, no electrical equipment should be placed without first conducting a comprehensive short circuit analysis of the power distribution.

B. Grading of Over Current Relays

The duration that must be allotted between the operations of two adjacent relays to achieve the right discrimination between them is called Grade Margin (S. Saini, 2014). Relay grading is actually a procedure in which the relay settings are such that when a fault occurs at any point, only the relay closest to the fault spot should respond to provide a selective operation. Relay grading scheme could be implemented via current grading, time grading and time-current grading.

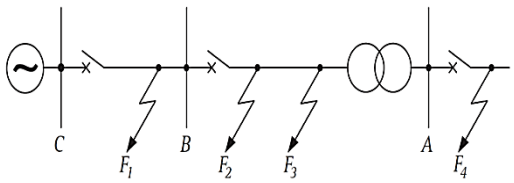

Figure 2: Discrimination by current

In current grading system, the fault current changes with the position of the fault due to variation in impedance value between the source and the fault. Thus, discrimination is achieved by reducing the current setting as we go closer to the source (E. Csanyi, 2018), therefore making the relay closest to the fault to trip the breaker.

The objectives of this study are to ensure that the right order of relay coordination is achieved and that the safety of personnel working in power system facility is secured thus, engendering efficient power delivery.

III. MATERIALS AND METHOD

A. Research Materials

Materials required for this research analysis and investigation are obtained from the Port Harcourt Electricity Distribution Company (PHEDC) and the Transmission Company of Nigeria (TCN).

TABLE I
DATA REQUIRED FOR CALCULATIONS AND SIMULATION FROM PHEDC AND TCN

S/N	Parameter	Assumptions
1	Route length of 33kV line	4.5 km
2	Maximum load on 33kV line	15.3 MW
3	T1B 30MVA Impedance at Transmission station	12.50%
4	T1 15MVA Impedance at Marine Base Injection Substation	10.52%
5	T2 15MVA Impedance at Marine Base Injection Substation	10.60%
6	Peak load on Churchill 11kV Feeder	2.8 MW (168 A)
7	Peak load on NPA 11kV Feeder	2.7 MW (162 A)
8	Peak load on Station Road 11kV Feeder	3.5 MW (210 A)
9	Peak load on Amadi North 11kV Feeder	3.3 MW (198 A)
10	Conductor Size	150 mm^2
11	Conductor type	AAC
12	Cable size	240 mm sq
13	CTRs Incomer	1250-800/1
	CTRs Outgoing	600-300/1
14	Base MVA	100
15	Relay Type	Schneider O/C and E/F Relay
16	Conductor Resistivity at 32 °C Ωm	$2.83X10^{-8}$
17	33kv line spacing	914.4 mm

B. Method of Analysis

Short circuit current analysis and relay coordination with Standard Inverse and Definite Time are applied. Relay- Circuit Breaker reaction to fault current is examined using short circuit analysis technique, which is used to evaluate the performance of the existing network.

For a known source Impedance and Base MVA, total fault impedance at Marine Base 2×15MVA, 33/11kv injection substation in p.u can be evaluated starting from the Resistance, R of a conductor to the geometric mean distance between the line conductors, the per kilometre reactance of one phase, line reactance, X, the distributed series impedance, Z_1, the equivalent admittance which is a measure of how easily a circuit or device will allow the flow of electric current, $Z_0 = Y$, then transmission line constants, Z_1P.U referred to base MVA in p.u from the data as provided in Table 1 as

$$Z_F = Z_s + Z_1 + Z_t \quad (1)$$

where $Z_t = Z_{pu} = \frac{\%\, Z \times (Base\ MVA)}{Transformer\ MVA}$ (2)

For a 3 phase 11kV line fault at the injection substation,

$$Fault\ MVA = \frac{Base\ MVA}{Total\ Fault\ Impedance\ at\ the\ sytationA} \quad (3)$$

Fault current, $\boldsymbol{I_F}$ at the station is:

$$I_F = \frac{Fault\ MVA}{\sqrt{3} \times V_{LL}} \quad (4)$$

where V_{LL} is the Line-Line Voltage

Referring to Table 1, the conductor resistance, R is 0.849 Ω and the diameter, ***d*** and radius, ***r*** 13.82mm and 6.91mm respectively. The line reactance, X_0 for a 4.5 km line is 1.4503Ω., while the distributed series impedance, $\boldsymbol{Z_1}$ becomes 1.6805 Ω , and the Admittance, Z_o = Y is 2.6971 Ω

For Source Impedance for base MVA of 100 MVA and Source % Impedance of 12.5%,

Source Impedance, $Z_{SP.U}$

$$Z_{s\,P.U} = \frac{12.5}{100} \times \frac{100}{30} = 0.417\ p.u \quad (5)$$

and

$$Z_{1P.U} = \frac{1.6805 \times 100}{(33)2} = 0.1543 \text{p.u} \quad (6)$$

i) Relay Calculation Setting:

Relay 8: Station Road Feeder Protective Relay

Maximum load of Station Road 11kV feeder = 210Amps.

TMS = 0.08 (Simulated Set Value)

Time difference between two Relays as 100ms

CT Ratio = 600/1A (7)

PS = 50%

Curve Type: Standard Inverse

Fault current (ETAP) on Station Road Feeder = 4.561kA

$$\text{PSM} = \frac{I_f}{PS \times CT\ Ratio} = \frac{4.561 \times 1000}{0.5 \times 600} = 15.2 \quad (8)$$

$$\text{T} = \frac{0.14}{PSM^{0.02} - 1} \times TMS \quad (9)$$

$$\text{T} = \frac{0.14}{15.2^{0.02} - 1} \times 0.08 = 200\text{ms} \quad (10)$$

RELAY 5: T_2 11KV Incomer Relay

Time of operation of Relay 5= 100 + 200 = 300ms

I_F = 3.397kA

$$PSM = \frac{I_F}{PS \times CT\ Ratio} = \frac{3.397 \times 1000}{0.7 \times 800} = 6.07 \quad (11)$$

$$0.300 = \frac{0.14}{6.07^{0.02} - 1} \times TMS \quad (12)$$

TMS = 0.08

RELAY 3: T_2 33KV Control Panel Relay

Time of Operation of Relay 3 = 100 + 300= 400ms

I_F = 1.168kA

$$PSM = \frac{I_F}{PS \times CT\ Ratio} = \frac{1.132 \times 1000}{0.6 \times 300} = 6.29 \quad (13)$$

$$0.400 = \frac{0.14}{6.29^{0.02} - 1} \times TMS \quad (14)$$

TMS = 0.1

IV. RESULTS AND DISCUSSION

A. Relay coordination of Station Road 15MVA, 33/11kV Substation (Existing Case)

Figure 3 depicts the order of tripping sequence for a 3-phase fault in the existing network injected on Station Road feeder. The tripping sequence is in the order of: Feeder circuit breaker (CB8) → 33kV line Breaker (CB1) → 33kV Control Panel Breaker(CB3) → 11kV Incomer Breaker(CB5). This response violates the right order of operation.

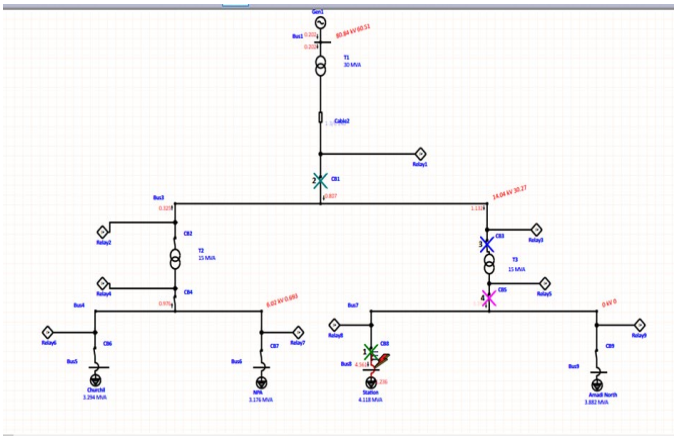

Figure 3: Circuit Breaker Tripping Sequence for Fault on Station Road Feeder (Existing case)

TABLE II
RELAY RESPONSE SEQUENCE WITH TIME OF OPERATIONS

Sequence-of-Operation Events - Output Report: Untitled

3-Phase (Symmetrical) fault on connector between CB8 & Station. Adjacent bus: Bus7

Data Rev.: Base Config: Normal Date: 08-01-2022

Time (ms)	ID	If (kA)	T1 (ms)	T2 (ms)	Condition
24.3	Relay8	4.561	24.3		Phase - OC1 - 51
30.0	Relay1	0.807	30.0		Phase - OC1 - 51
84.3	CB8		60.0		Tripped by Relay8 Phase - OC1 - 51
110	CB1		80.0		Tripped by Relay1 Phase - OC1 - 51
145	Relay3	1.132	145		Phase - OC1 - 51
165	CB3		20.0		Tripped by Relay3 Phase - OC1 - 51
224	Relay5	3.397	224		Phase - OC1 - 51
244	CB5		20.0		Tripped by Relay5 Phase - OC1 - 51

Table II represents the operation of relays with their adjoining circuit breakers and the corresponding tripping time (ms) for 3-phase fault on Station Road feeder of the existing network.

There is a clear violation of relay response to fault when compared with the proper sequence.

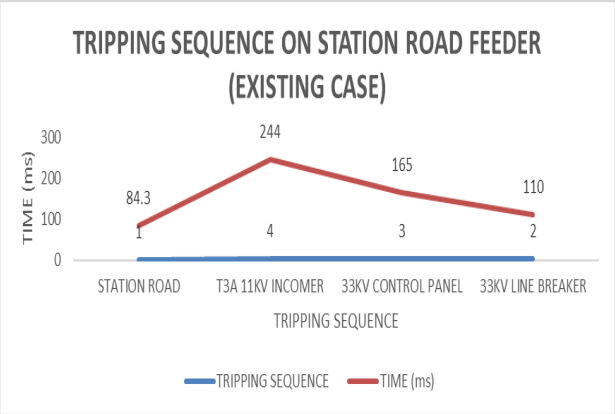

Figure 4: Breaker Operation Sequence for Fault on Station Road Feeder (Existing Case)

Figure 4 represents a graph of the various circuit breakers tripping sequence with their corresponding time of operation in response to a 3-phase fault on Station Road feeder for the existing case.

B. Relay coordination of Station Road 15MVA, 33/11kV Substation (Improved Case)

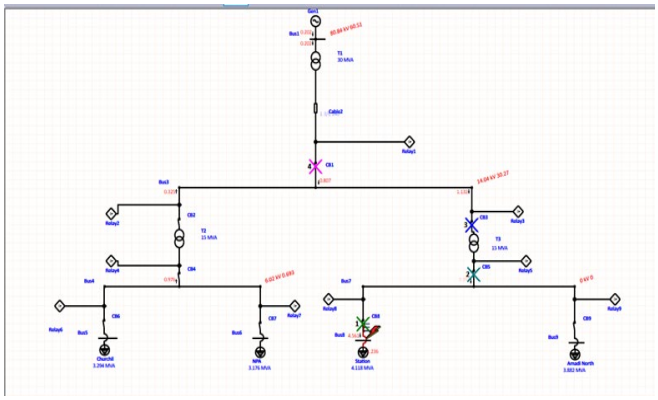

Figure 5: Circuit Breaker Tripping Sequence for Fault on Station Road Feeder

Figure 5 explains the sequence of tripping for a 3-phase fault on Station Road 11kV outgoing feeder for the improved network. This mode of operation shows the right order, which is:
Feeder Circuit Breaker (CB8) → 11kV Incomer Breaker(CB5) → 33kV Control Panel Breaker(CB3) → 33kV line Breaker(CB1).

TABLE III
RELAY RESPONSE SEQUENCE WITH TIME OF OPERATION FOR MODIFIED CASE

Sequence-of-Operation Events - Output Report: Untitled

3-Phase (Symmetrical) fault on connector between CB8 & Station. Adjacent bus: Bus7

Data Rev.: Base Config: Normal Date: 15-01-2022

Time (ms)	ID	If (kA)	T1 (ms)	T2 (ms)	Condition
200	Relay8	4.561	200		Phase - OC1 - 51
240	CB8		40.0		Tripped by Relay8 Phase - OC1 - 51
313	Relay5	3.397	313		Phase - OC1 - 51
336	Relay3	1.132	336		Phase - OC1 - 51
340	Relay1	0.807	340		Phase - OC1 - 51
373	CB5		60.0		Tripped by Relay5 Phase - OC1 - 51
407	Relay9	1.166	407		Phase - OC1 - 51
416	CB3		80.0		Tripped by Relay3 Phase - OC1 - 51
420	CB1		80.0		Tripped by Relay1 Phase - OC1 - 51

Table III represents the operation of relays with its associated circuit breakers and the corresponding tripping time (ms) for the modified case or new case for a 3-phase fault on Station Road feeder.

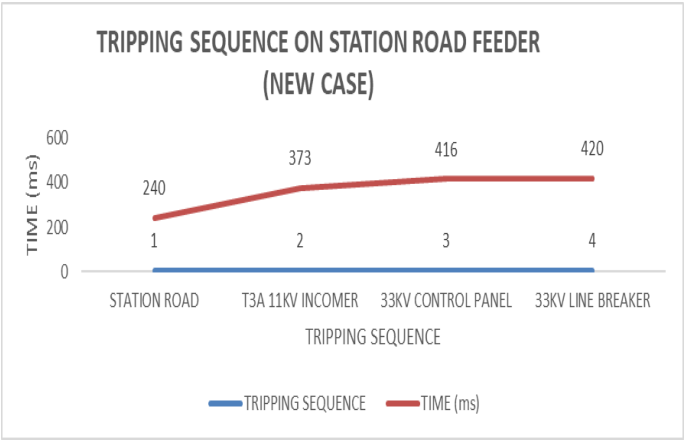

Figure 6: Sequence of Circuit Breaker operation for fault on Station Road feeder (Improved Case)

Figure 6 shows a graph representation of the various circuit breaker tripping sequence with its associated time of operation in response to a 3-phase fault on Station Road feeder for a modified case.

TABLE IV
COMPARING SEQUENCE OF OPERATION OF CIRCUIT BREAKERS

Comparison Of Existing Case With New Case On Station Road Feeder			
Feeder	Tripping Sequence	Time (ms)	
		Existing	New
Station road	1	84.5	240
T3a 11kv incomer	2	244	373
33kv control panel	3	165	416
33kv line breaker	4	110	420

Table IV clearly shows the distinctive difference between the existing and modified case regarding sequence of operation of various circuit breakers to fault on Station Road 11kv outgoing feeder.

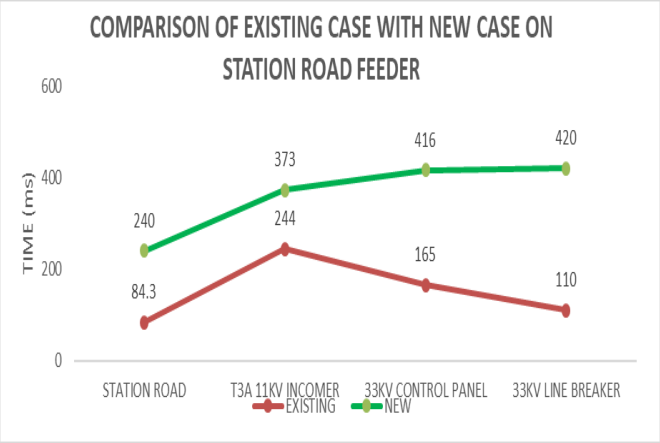

Fig 7 Comparison of Sequence of Circuit Breaker Operation for Fault on Station Road Feeder (Existing case vs New Case)

Figure 7 represents the different graphical behaviour of circuit breakers in response to a 3-phase fault on Station Road feeder when comparing existing with modified case

TABLE V
RELAY OPERATING TIME FOR FAULT ON STATION ROAD FEEDER

Relay Time Operations (Sec)							
Relay	Theoretical Calculations / (SOP)		ETAP Modified Network/ (SOP)		ETAP Existing Network/ (SOP)		Curve Type
Relay 8	0.08	**(1)**	0.08	**(1)**	0.083	**(1)**	**SIT**
Relay 5	0.081	**(2)**	0.082	**(2)**	0.1	**(4)**	**SIT**
Relay 3	0.1	**(3)**	0.09	**(3)**	0.09	**(3)**	**SIT**
Relay 1	0.34	**(4)**	0.34	**(4)**	0.19	**(2)**	**Definite Time**

V. CONCLUSION

Protection scheme is very essential in power engineering for safety and quality power delivery. To arrive at appropriate coordination, the parameters of the relay should be correctly examined. Power systems relays should be adequately coordinated to provide primary and back up security.

The result of the existing network in ETAP 19.0.1 when a 3-Phase fault is introduced at the Station Road feeder shows a wrong order of relay coordination and its adjoining protective devices. Thus, an adjustment on Time current curve (TCC) is done to solve the inappropriate operation leading to an improved case.

Manual computation and comparison of relay settings with simulated figures for both existing and improved cases reveal a slight difference between the existing case and improved case coordination. This means that the result obtained by both methods i.e., manual calculation and simulation are almost the same on improved case.

Lastly, a thorough comparison was carried out to justify result based on sensitivity, security and selectivity. The result shows that the improved case validates the attributes of a sound protective relay in response to fault.

VI. RECOMMENDATIONS

PHEDC should consider incorporation of numerical or digital relays in its networks for fast response time; and to also carry out regular routine test on the various protective devices in order to ascertain their functionality.

REFERENCES

Aguiyi Watson, Ayibapreye Benjamin (2022), Computation of Electric and Magnetic Field Strengths under Nigerian 330 KV Power Lines, *International Journal of Scientific Engineering and Applied Science (IJSEAS),* Volume-8, No. 2, pp. 83-90.

Hussain, M. H., Musirin, I., Rahm, S. R. A. Abidin, A. F., & A zmi, A. (2013). Optimal Overcurrent Relay Coordinatio n using Particle Swarm Optimization. *2013 Internation*

al Conference on Electrical, Control and Computer En gineering, 42-47

Uwho, K. O., Amadi, H. N. & Obire, P. (2022). Short Circuit Analysis for Effective Relay Coordination in Nigerian P ort Authority, Rivers State. *Journal of Emerging Trends in Electrical Engineering,* 4(3), 1-9.

Ogbuefi, U. C., Anyaka, B. O., & Mbunwe, M. J. (2019). Reactive power loss minimization on an interconnected electric power network. *Transactions on Engineering Technologies*, 207-228, https://doi.org/10.1007/978-981-13-2191-7_16

Birla, Dinesh; Maheshwari, Rudra Prakash; and Gupta, Hari Om (2005), Time-Overcurrent Relay Coordination: A Review, *International Journal of Emerging Electric Power Systems:* Vol. 2: No. 2, Article 1039. DOI: 10.2202/1553-779X.1039

Jayaprakash, J., Angelin, M., & Lakshmi, J. (2016). Planning and Coordination of Relay in Distribution System using ETAP Pakistan, *Journal of Biotechnology*, 13, 252-256.

Obire, P., Idoniboyeobu, D. C. & Braide, S. L. (2022). Protective Relay Coordination in an Injection Substation using Short Circuit Analysis. *International Journal of Advances in Engineering and Management (IJAEM),* 4(8),753-763.

Igbogidi, O.N., Idoniboyeobu, D. C., & Braide, S. L. (2018). Improved Relay Coordination in Port Harcourt Distribution Network: Case Study of RSU 2 X 15MVA, 33/11kV Injection Substation. *American Journal of Engineering Research (AJER), 7(7), 43-56.*

Saini, S. (2014). Overcurrent Relay Coordination for Phase and Earth Faults using ETAP. *Electrical and Electronics Department, Amity University (AUUP), Noida, India. Proceedings of 7th IRF International Conference, Pune, India,* ISBN: 978-93-84209-09- 4

Csanyi, E. (2018). The Fundamentals of Protection Relay Coordination and Time/Current Grading Principles.

Journal of Engineering, Emerging Technologies and Applied Sciences -– Volume 1 Issue 2, Nov. 2023

Available at ***https://www.ndu.edu.ng/journalofengineering/***

RESEARCH ARTICLE OPEN ACCESS

Absorbed Dose Rate of Some Body Organs in Diete-Koki Memorial Hospital, Opolo, Yenagoa, Bayelsa State

*Godwin E. Ogobiri, **Ibuama E. Abule, *Keneke E. Dauseye, **Uzoukwu P. Amanuche

*Department of Physics, Niger Delta University, Bayelsa State, Nigeria

**Department of Physics, Bayelsa Medical University, Bayelsa State, Nigeria

ogobirige@ndu.edu.ng

----------**********----------

Abstract:

The research work was carried out at Diete-koki Memorial Hospital, located at Opolo, Yenagoa, Bayelsa State, Nigeria. The Background Ionizing Radiation (BIR) was measured for five different locations in the Hospital with the aid of radiation device- Radalert x100 where locations such as X-ray room, Walkway, Accident and Emergency room, Reception and waiting room were measured and the mean value obtained for the various locations. The radiological parameters were calculated with an already established conversion factors and formula. The results shows that the Background ionizing radiation exposure (BIR) mean for each location, is indicated in the Bar chart, Background ionizing radiation (BIR) mean values ranges from 0.008±0.001 to 0.013±0.003 mSv/y respectively. The Absorbed dose rate (AbD) mean value ranges from 0.070±0.001 to 0.113±0.002 nGy/h. while the calculated Annual Effective Dose Rate (AEDE) mean values ranges from 0.107±0.001 to 0.411±0.003 mSv/y. The calculated mean values of Excess Life Cancer Risk (ELCR) ranges from 0.294 x10-3 to 0.630 x10-3. The percentage of Radiation Dose distribution rate in respect to different body organs shows that the ovaries recorded the lowest percentage of 13% as against the testes which have the highest percentage with 18%. All radiological parameter values recorded are in comparison with the World Permissible Limits as provided by UNSCEAR 2000.

Keywords **— Radiation, Background Ionization radiation, Dose Distribution, Dose rate, measurement**

----------**********----------

I. INTRODUCTION

Radiation is defined as the release or transfer of energy as waves or particles via space or a material medium. Radiation is the energy that shifts from one place to another as waves or particles. Radiation exposure is a part of daily life, some well-known sources of radiation include the sun, microwave ovens in our kitchens, and radios in cars. Most of this radiation does not represent a health risk to humans, but some does. At smaller dosages, radiation usually poses less of a concern nevertheless, at higher concentrations, it could. When radiation energy is strong enough, it may ionize atoms, or knock electrons out of atoms to create ions. When one electron is removed from an atom's electron shell - also known as "knocked out"—the atom acquires a net positive charge. This process is known as ionization, because this ionization has the potential to harm live cells and, more significantly, the DNA.

Radiation workers may wear dosimeters to track their radiation exposure, and the general public can use them to assess the radiation dosage they get from natural sources or medical treatments. The process of determining the effective dose involves multiplying the equivalent dose by a tissue weighting factor that is specific to the type of tissue exposed to radiation. In the event that multiple organs are exposed to radiation, the total effective dose for all exposed organs is then summed to determine the dosage that is effective for the organ (Biere et al., 2022).

$$Dorgan(\,mSvy^{-1}) = O \times AEDE \times F \quad (1)$$

where, O is the occupancy, 0.8, $AEDE$ is the annual effective dose equivalent, and F is the conversion

factor for organ dose from ingestion inside those cells.

Cancer risks are raised by ionization radiation exposure (Smith 2000). Ionizing radiation is useful in research, medicine, and building, but when handled incorrectly, it may be harmful to one's health. Radiation exposure damages living tissues. High doses can cause acute radiation syndrome (ARS), which manifests as skin burns, loss of consciousness, internal organ failure, and death. All doses can increase the risk of cancer and genetic damage. One type of cancer known as "thyroid cancer" frequently arises from nuclear weapons and reactors as a result of the biological products of the radiative iodine fission product. To now, estimations of the precise risk and likelihood of ionizing radiation-induced cancer in cells are based mostly on population-based data from the atomic bombs, although Dosimeters, which are instruments that measure how this knowledge is still lacking (Hans, 2019).

II. METHODOLOGY

The study was carried out at Diete-koki Memorial Hospital, located at Opolo, Yenagoa, Bayelsa State. The Background Ionizing Radiation (BIR) was measured for different five locations such as X-ray room, walk way, accident and emergency room, the reception, and waiting room. At each location, five points were measured with aid of radiation device-Radalert x100, which was held 1 meter above the ground. At each location, the BIR mean value was obtained and the radiological parameters was calculated as shown in the tables and bar charts below.

Figure 1: Back and Front view of the Radiation Monitoring Device- Radalert x100

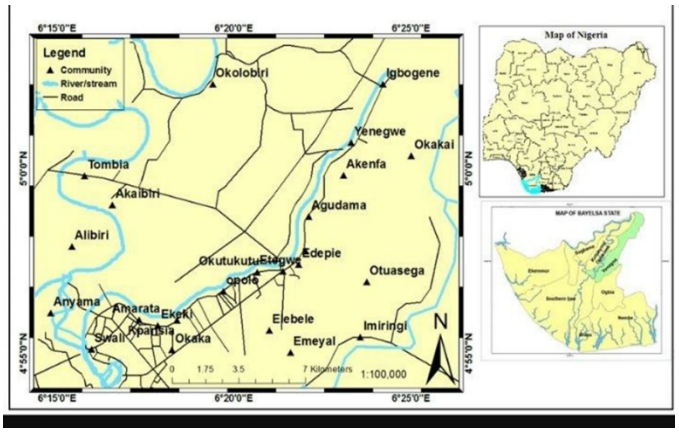

Figure 2: Geological map of the study area

The GPS location of the study area, Diete Koki Memorial Hospital, Opolo Yenagoa, Bayelsa State is Latitude 40 55’ 36.30” N and Longitude 6’3.50 E.

III. RESULTS AND DISCUSSIONS

The Background Ionizing Radiation (BIR) measurements and other radiological parameters for the various locations at Diete Koki Memorial Hospital, Opolo, Yenagoa, Bayelsa State, Nigeria is shown below.

Table 1: Reception showing the background ionizing radiation (BIR) measurements and other radiological parameters

LOCATION	BIR (mR/h)	ABD (nGy/h)	EDQ (mSv/y)	AEDE (mSv/y)	ELCR
Location 1	0.011±0.002	0.096	0.964	0.147	0.405
Location 2	0.005±0.001	0.044	0.438	0.067	0.184
Location 3	0.007±0.001	0.061	0.613	0.093	0.258
Location 4	0.011±0.002	0.096	0.964	0.147	0.405
Location 5	0.009±0.002	0.078	0.788	0.120	0.331
MEAN	**0.009±0.002**	**0.075**	**0.753**	**0.115**	**0.317**

Table 1 shows the Background ionizing exposure rate of the reception and other calculated radiological parameters. Location 2 recorded the lowest BIR value of 0.005±0.001 mSv/y as against location 1 and 4 with a BIR value of 0.011±0.002 mSv/y and with a mean value of 0.009±0.002 mSv/y.

Table 2: Waiting room showing the background ionizing radiation (BIR) measurements and other radiological parameters

LOCATION	BIR (mR/h)	ABD (nGy/h)	EDQ (mSv/y)	AEDE (mSv/y)	ELCR
Location 1	0.009±0.002	0.078	0.788	0.120	0.331
Location 2	0.012±0.002	0.104	1.051	0.160	0.442
Location 3	0.001±0.001	0.009	0.088	0.013	0.037
Location 4	0.008±0.001	0.070	0.701	0.107	0.294
Location 5	0.01±0.001	0.087	0.876	0.133	0.368
MEAN	**0.008±0.001**	**0.070**	**0.701**	**0.107**	**0.294**

Table 2 showing the background ionizing exposure rate of the waiting room with other calculated radiological parameters. Location 3 and 5 recorded the lowest BIR value of 0.001±0.001 mSv/y as against location 1 with a BIR value of 0.009±0.002 mSv/y with an average value of 0.008±0.001 mSv/y.

Table 3: X-ray room showing the background ionizing radiation (BIR) measurements and other radiological parameters

LOCATION	BIR (mR/h)	ABD (nGy/h)	EDQ (mSv/y)	AEDE (mSv/y)	ELCR
Location 1	0.016±0.003	0.139	1.402	0.213	0.589
Location 2	0.017±0.003	0.148	1.489	0.227	0.626
Location 3	0.012±0.002	0.104	1.051	0.160	0.442
Location 4	0.013±0.002	0.113	1.139	0.173	0.479
Location 5	0.007±0.001	0.061	0.613	0.093	0.258
MEAN	**0.013±0.002**	**0.113**	**1.139**	**0.411**	**0.630**

Table 3 shows the background ionizing radiation exposure rate of the X-ray room with other calculated radiological parameters. Location 5 with the lowest BIR value of 0.007±0.001 mSv/y as against location 2 with a BIR value of 0.017±0.003 mSv/y with an average BIR value of 0.013±0.002.

Table 4 shows the background ionizing radiation exposure rate of the walkway with other radiological parameters calculated. Location 3 with the lowest BIR value of 0.008±0.001 mSv/y as against location 1 and 3 with a BIR value of 0.013±0.002 mSv/y, with an average BIR value of 0.011±0.002 mSv/y.

Table 4: Walkway showing the background ionizing radiation (BIR) measurements and other radiological parameters

LOCATION	BIR (mR/h)	ABD (nGy/h)	EDQ (mSv/y)	AEDE (mSv/y)	ELCR
Location 1	0.013±0.002	0.113	1.139	0.173	0.266
Location 2	0.011±0.002	0.096	0.964	1.467	2.249
Location 3	0.008±0.001	0.070	0.701	0.107	0.164
Location 4	0.010±0.001	0.087	0.876	0.133	0.204
Location 5	0.013±0.002	0.113	1.139	0.173	0.266
MEAN	**0.011±0.002**	**0.096**	**0.964**	**0.173**	**0.464**

Table 5: Accident and emergency room showing the background ionizing radiation (BIR) measurements and other radiological parameters

LOCATION	BIR (mR/h)	ABD (nGy/h)	EDQ (mSv/y)	AEDE (mSv/y)	ELCR
Location 1	0.0080±0.001	0.070	0.701	0.107	0.294
Location 2	0.010±0.001	0.087	0.876	0.133	0.368
Location 3	0.010±0.001	0.087	0.876	0.133	0.368
Location 4	0.011±0.002	0.096	0.964	0.147	0.040
Location 5	0.013±0.002	0.113	1.139	0.173	0.479
MEAN	**0.010±0.001**	**0.090**	**0.911**	**0.139**	**0.310**

Table 5 shows the background ionizing radiation exposure rate at the accident and emergency room with other parameters calculated. Location 1 with the lowest BIR value of 0.008±0.001 mSv/y as against location 5 with a BIR value of 0.013±0.002 mSv/y, with an average BIR value of 0.010±0.001 mSv/y.

Table 6 shows the radiation exposure rate of selected body organs annually and Excess life cancer rate with the aid of already established conversion factors.

Figure 2 shows the BIR exposure mean for each location, from the bar chart the waiting room recorded the lowest BIR with a mean value of 0.008±0.001 mSv/y as against X-ray room which have the highest BIR mean value of 0.013±0.003 mSv/y.

Table 6: Effective Dose rate for different body organs

BODY ORGANS	CONVERSION FACTOR	CALCULATED AEDE MEAN (mSv/y)	ORGAN EFFECTIVE DOSE (mSv/y)
Lungs	0.64	0.189	0.121
Ovaries	0.58	0.189	0.110
Bone	0.69	0.189	0.130
Testes	0.82	0.189	0.155
Kidney	0.62	0.189	0.117
Liver	0.46	0.189	0.087
Whole	0.68	0.189	0.129

Figure 3 shows the absorbed dose rate (AbD) mean value for each location in the study area, the reception recorded the lowest with a mean value of 0.075±0.001 nGy/h as against the X-ray room which have the highest mean value of 0.113±0.002 nGy/h.

In Figure 4, the calculated Annual Effective Dose Rate (AEDE) mean for each location is shown. The waiting room recorded the lowest mean value of 0.107±0.001 mSv/y as against the X-ray room which have a mean value of 0.411±0.003 mSv/y.

Figure 5 shows the calculated mean values of Excess Life Cancer Risk (ELCR) for each location in the study area, the waiting room with the lowest mean value of 0.294 x10-3 as against the X-ray room which have a highest mean value 0f 0.630 x10-3.

In Figure 6, the pie chart shows the percentage Radiation Dose distribution rate in respect to the different body organs, the ovaries recorded the lowest percentage of 13% as against the testes which have the highest percentage with 18%. All radiological parameter values are in comparison with the World Permissible Limits as provided by UNSCEAR 2000.

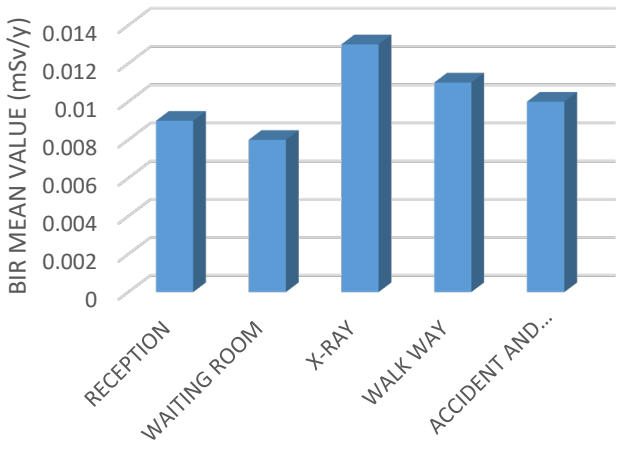

Figure 2: A bar chart of BIR mean values against locations

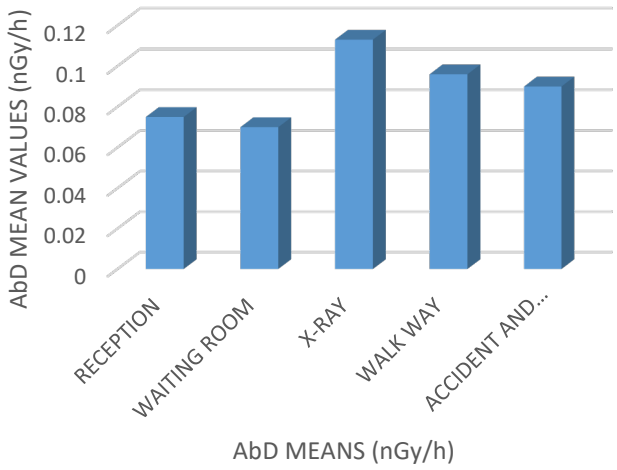

Figure 3: A bar chart of AbD mean values against locations

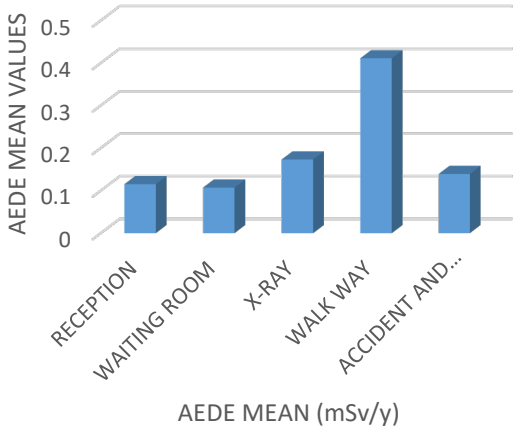

Figure 4: A bar chart of AEDE mean values against locations

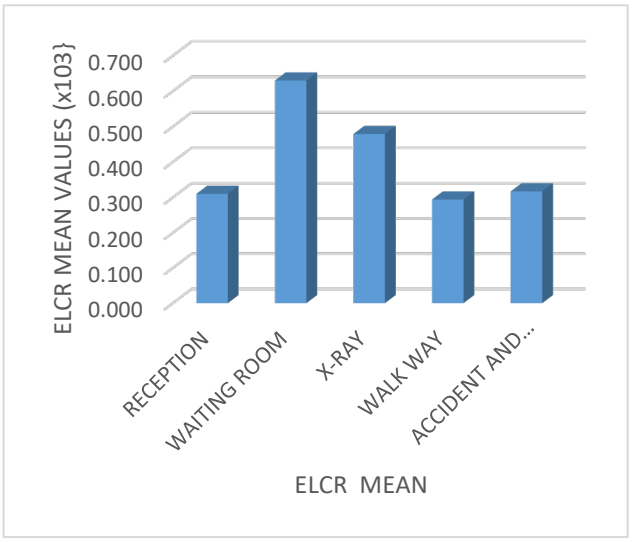

Figure 4: A bar chart of AEDE mean values against locations

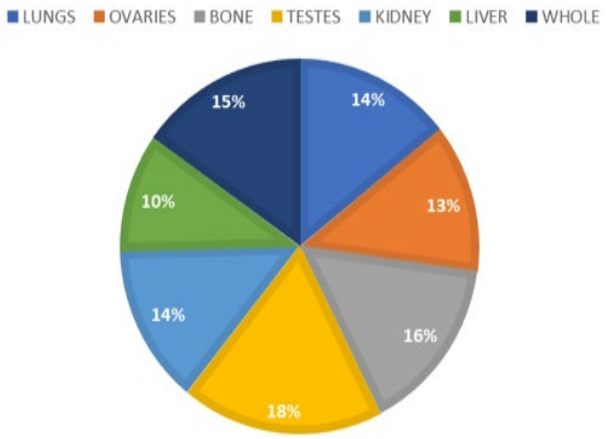

Figure 6: A Pie chart of percentage of Radiation Exposure rate against selected body organs

IV. CONCLUSION

The study was carried out at Diete-koki Memorial Hospital, located at Opolo, Yenagoa, Bayelsa State. The BIR was measured for five different locations such as X-ray room, walkway, accident and emergency room and the reception. The primary goal of this research work was to carry out a radiological risk assessment to determine the likelihood of cancer rate in the Hospital. The Pie chart the shows the percentage of Radiation Dose distribution for the different body organs with the ovaries recording the lowest percentage of 13% as against the testes which have the highest percentage with 18%. All radiological parameter values are in comparison with the World Permissible Limits as provided by UNSCEAR 2000. Hence, the Hospital is encouraged to regularly check or monitor background radiation of their environment in comparison with the world permissible limit.

REFERENCES

Avwiri GO, Agbalagba EO (2012) Studies on the Radiological Impact of Oil and Gas Activities in Oil Mineral Lease 30 (Oml30) Oil Fields in Delta State, Nigeria.

Biere, P. E., Ogobiri, G. E., Ajetunmobi, A. E., Aina, J. O. and Joel, R. R (2022). The Measurement of Scattered Radiation Doses and Estimation of Some Organ Doses

in X-Ray Rooms of Three Hospitals in Yenagoa, Bayelsa State, South-South, Nigeria.

Eisenbud, Merril; Gesell, Thomas F. (1997). Environmental radioactivity: from natural, industrial, and military sources. Academic Press. pp. 171–172. ISBN 978-0-12-235154-9. It is important to recognize that the potassium content of the body is under strict homeostatic control and is not influenced by variations in environmental levels. For this reason, the dose from 40K in the body is constant.

Hans H.S (2019). Nuclear Physics Experimental and Theoritical. New Age International Publishers.

Occupational Radiation Protection: Protecting Workers Against Exposure To Ionizing Radiation" (Pdf). International Atomic Energy Agency. 30 August 2002. Archived (PDF) from the original on 29 November 2003. Retrieved 21 October 2022.

Radiological Consequences of the 1957 Windscale Fire". 10 October 1997. Archived from the original on 17 May 2013. Retrieved 24 January 2013.

Smith F.A (2000). Applied Radiation Physics. World Scientific Publishing.

United Nations Scientific Committee on the Effects of Atomic Radiation (2000). Sources and Effects of Ionizing Radiation - UNSCEAR 2000 Report to the General Assembly, with Scientific Annexes (Report). Retrieved 12 September 2022.

World Health Organization (April 2006). "Health effects of the Chernobyl accident: an overview". Retrieved 24 January 2013.

Journal of Engineering, Emerging Technologies and Applied Sciences -– Volume 1 Issue 2, Nov. 2023

Available at ***https://www.ndu.edu.ng/journalofengineering/***

RESEARCH ARTICLE OPEN ACCESS

Advancements in Autonomous Battery Monitoring: A System with Auto-Return Home Integration

Fred Oyinbonogha Agonga*, Justice Chikezie Anunuso**, Babawuya Alkali**, Mohammed Shaba Abubakar***, Callistus T. Ikwouazom****

*Department of Mechanical Engineering, Niger Delta University, Bayelsa State, Nigeria
Email: agongofred@ndu.edu.ng
** Department of Mechatronics Engineering, Federal University of Technology Minna, Niger State, Nigeria
***Department of Mechanical Engineering Technology, Niger State Polytechnic Zungeru, Niger State, Nigeria
****Department of Information and Media Technology, Federal University of Technology, Minna, Niger State. Nigeria.-------

----------**********----------

Abstract:

As the adoption of autonomous systems continues to proliferate in various industries, the need for reliable and efficient battery monitoring solutions becomes increasingly crucial. This paper presents the development and implementation of an innovative Autonomous Battery Monitoring System (ABMS) equipped with Auto-Return Home Integration (ARHI). The proposed system addresses the limitations of existing battery monitoring technologies by combining real-time data analysis, autonomous decision-making, and the ability to return autonomously to a charging station when necessary. Furthermore, the ABMS incorporates adaptive charging algorithms that optimize the charging process based on historical usage patterns, reducing energy waste and extending battery lifespan. Additionally, the system offers remote monitoring and control capabilities, allowing operators to oversee multiple autonomous systems equipped with ABMS from a centralized interface. In practical applications, the ABMS with ARHI integration has demonstrated significant improvements in the reliability and autonomy of battery-powered systems, particularly in industries such as unmanned aerial vehicles (UAVs), robotics, and autonomous ground vehicles. The ability to proactively address battery issues and seamlessly integrate autonomous return-to-base functionality enhances operational safety, reduces operational costs, and extends the overall lifespan of battery packs. Atmega328 microcontroller, wireless data module HC-12 model is used with transmitter and receiver and system application. The microcontroller control or handles the analog to digital conversion, the wireless module handles data transmission between transmitter and receiver, while the system application collects, store the continue data entrance to the receiver into Microsoft excel, display the data in system screen and also, plot graph with the stored data.

Keywords — **Microcontroller, Voltage Divider Network, Transmitter, Receiver, Wireless Data Module, VB.NET app. USB Serial Port**

----------**********----------

I. INTRODUCTION

Autonomous Battery Monitoring System (BMS) is a technology designed to monitor, control, and optimize the performance of batteries used in various applications. With the widespread use of batteries in devices such as electric vehicles (EVs), drones, renewable energy systems, and backup power systems or portable electronic systems, there is a growing need for efficient battery management systems. BMS plays a critical role in ensuring the safety, longevity, and performance of batteries by monitoring and controlling various parameters such as temperature, voltage, state of charge and discharge. Autonomous battery monitoring system comprises of several components that work together to monitor and control the performance of batteries which include: A battery Management Unit (BMU) is the central

component of a BMS and is responsible for collecting data from various sensors and controlling the battery's performance. The BMU is typically equipped with a microcontroller, memory, the communication interfaces: The communication interface is used for transmitting data from the BMU to external devices such PC system or human machine interface (HMI), or a battery management software. Human-machine interface is graphical user interface that permits or allow the operator to view and control the performance and battery current status, while the battery is in use. HMI also have ability to display various parameters such as voltage, temperature, current, state of charge and discharge in real-time.

Today, the use of drone for various application has been widely embraced by developing and developed nations and this cannot be unconnected to its ability to be fly using renewable energy battery, ability to be fly and be control without on board pilot, ability to maneuver easily, ability to fix on board camera and also, ability to travel to high altitude (Agha, S. et al., 2022) but the major constraint in the use of drone today, is the limitation in its battery power source and the monitoring aspect of its battery capacity while it is engaged in flight mode. (Arada, G. P. et al., 2014).

For most drone accident disasters, are usually caused by the system components, which may include, sudden, transmission signal cut-off between the transmitter and the receiver, faulting BLDC motor or battery voltage drop while in the drone is in flight mission. Generally, the overall functionality of a drone is highly dependent to battery capacity and its maintenance during its usage (Conference, N. et al., 2019). The common type of the battery used today in drones are lithium polymer battery. This type of battery is made up of cells e.g., 2s, 3s, or 5s. the higher the number of the cells the higher the amount of voltage and current it can produce (Corral, L. et al., 2016). One of the major advantages of lithium polymer battery, is that, its cells have about four times the energy density of a nickel cadmium or nickel metal hydride (Grey, C. et al., 2020). Lithium polymer battery is introduced to enable portable electronics, such that, it can be use in drones to serve as source of its power and its efficiency can be determine or maintain through or by observing the state of charge (SOC), state of discharge (SOD) and temperature variation while it's in state of used (Khofiyah, N. et al., 2019). Therefore, this research work focuses, on designing and development of automatic battery monitoring system with auto-return home, when the battery voltage threshold has drop to the level that cannot sustain or guarantee the safety of the drone with may lead to crashing, during flight mission.

II. REVIEW OF RELATED LITERATURE

Today battery monitoring system can be deployed for monitoring a renewable energy system, back-up power station, electric vehicle and also in portable electronic devices such as in drones by using a wireless data transmission approach. The result or the output obtained from the performance evaluation shows that, the research work was remarkable and interesting one because, the system designed, was able to monitor, control and transmit data in real-time from one point to another but the challenge is in the area of data transmission range. The system was only able to transmit data effectively, only when within 10meters apart (Mattada, M. et al., 2022). The assessment and control of a back-up power system as always being a challenge of all times. (Pham, N. N. et al., 2022) developed an automated battery monitoring system with a transmitter and receiver, the major achievement of the designed was that, the transmitter and the receiver were able to communicate effectively, without data lost but the constraint of the designed is that, the electronic circuit used for the system was not properly soldered and arranged, which over time will affect, the entire system functionality.

The use of drone today, for various applications has quiet achieved many significant but the major challenge to its use, is the ease in the probability of it to crash. (Roslan, N. F et al., 2020) designed and implemented an IOT base battery monitoring system with CAN BUS. The author, used distributed topology approach, allowing the slave module to monitor and protect multi-cell battery pack. The battery temperature, state of discharge, battery current

and battery voltage were successful monitored and sent to the master module simultaneously. The design, lack an inbuild system application that can keep recording and saving of the battery reading parameters. The system built by (Series, C. 2020) Arduino uno microcontroller ADC port to convert analog battery voltage to its digital equivalence. The system was tested and fully implemented in electric vehicle and the result obtained was compared to that of multimeter direct measurement, which was found the same. This shows that, the objectives of the design were achieved as planned. For the creation of an effective and dynamic uninterrupted power supply, (Sharif, S. et al., 2015) constructed a smart power management system for uninterrupted power supply, by using microcontroller based intelligent uninterrupted power supply.

The system designed was used in a LAB viz, to monitor and control the switching of electrical appliance automatically, according to the available voltage in the UPS, during power failure. During performance evaluation test, the result achieved was satisfactory, because the power consumption rate reduces drastically and more energy is saved. The limitation of the work is that, there was a battery voltage fluctuation. Remote monitoring and control is the one of the most important requirements for maximizing process plant requirement (Wild, G. et al., 2017). For a diagnostic and data entrance monitoring purposes, in a battery monitoring system, the use of an indicator, that shows the continuous data coming in or receiving, compliment the system design. (Kumar, M. R. et al., 2018) implement a battery monitoring system, using a peripheral interface controller as a control unit with a universal asynchronous receiver/transmitter (UART) device. The major breakthrough of the design is that, the author, uses a liquid crystal display and a light emitting diode to show and display the measured parameters such as the battery state of discharge, current and voltage respectively but the design does not include the use of a prolific USB serial communication channel, which will enable the receiver to send onward data to PC system in order to achieve fast and reliable data deliver.

III. MATERIALS AND METHOD

This section deals with the entire system design analysis, material selection and system construction.

A. Required Components

The components required for this project is divided into hardware and software. The hardware part used include the following; Microcontroller (atmega328), HC_12 wireless Module, Voltage Regulator, Capacitor, Resistor and PCB Circuit. The software part includes; integrated Atmel Microchip programming software, VB.NET Programming Software and Proteus software.

B. Methods

Figure 1 shows the electric circuit diagram of the entire system hardware components used. The circuit illustrates how the reference battery voltage is connected to the transmitter circuit that handles the conversion of analog battery voltage to its digital equivalence. The microcontroller, sent the converted value to the wireless data module, which also sent same data to the receiver via air. The receiver is connected to the PC system by using prolific USB cable via PC serial port, for onward delivery of data to PC system. The VB.NET application, allowed for data collection, display, saved the said data and also permits or allowed data plotting through the use of Microsoft excel sheet. Following the required sequential steps, the microcontroller code was uploaded to the controller.

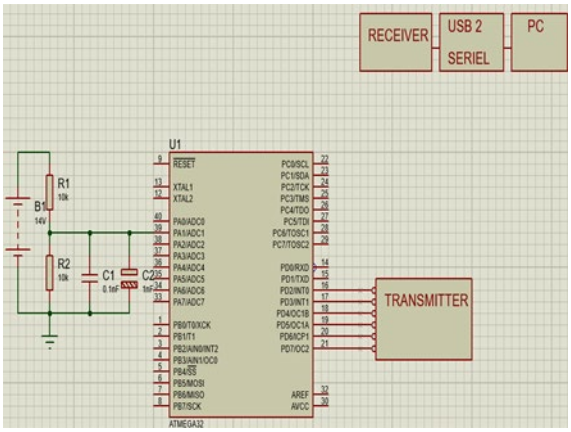

Figure 1: System Electric Circuit

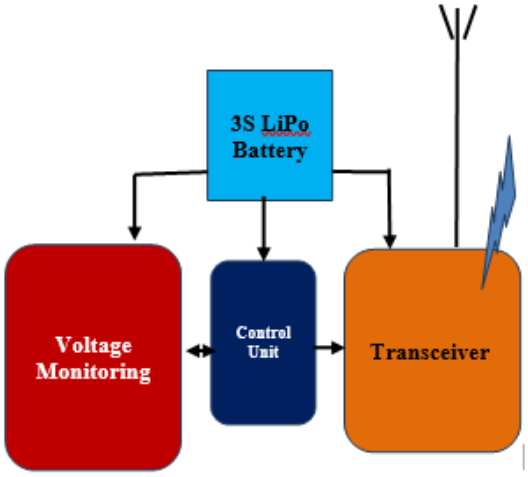

Figure 2: System Block Diagram

C. System Construction Procedures

The wireless data module VCC (power), GND (ground) are connected to 4.2volts via a diode and the module RX and TX pins are respectively connected to the microcontroller serial communication protocol in order to allow effective data transmission.

D. System's Algorithm

The Figure 3 is the algorithm of the system showing step by steps of how the system works. According to the flowchart, the Atmega ADC port sample the reference battery voltage, convert, and send to receiver. The receiver then, send to PC system and PC display the result through the use of VB.NET application.

E. MATLAB Virtual Simulation Model of Analog to Digital Conversion (ADC)

In the Battery state monitoring, the simulation model accurately captures the behaviour of the monitored battery, providing real-time data on parameters such as voltage, current, temperature, state-of-charge (SOC), and state-of-health (SOH). Figure 4 depicts the virtual simulation of the system designed; ADC toolbox MATLAB Simulink was used.

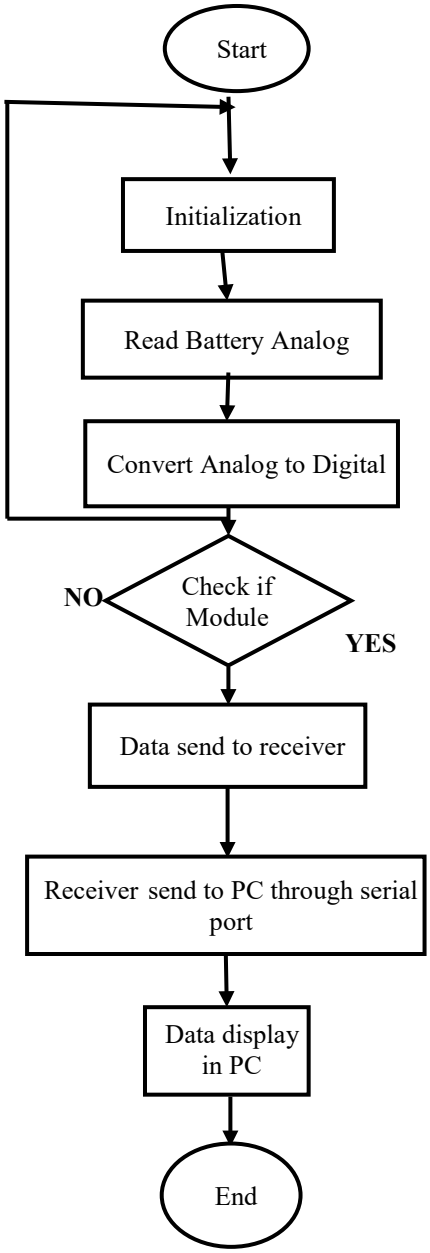

Figure 3: System Flowchart Diagram

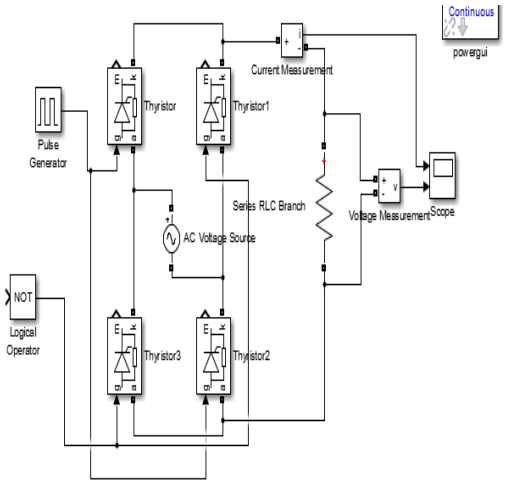

Figure 4: MATLAB Battery Simulink Model

F. VB.NET User Graphic Interface Application Design

Figure 5 depicts the VB.NET User graphic interface application design, it enables user for data collection, display store and graph plot.

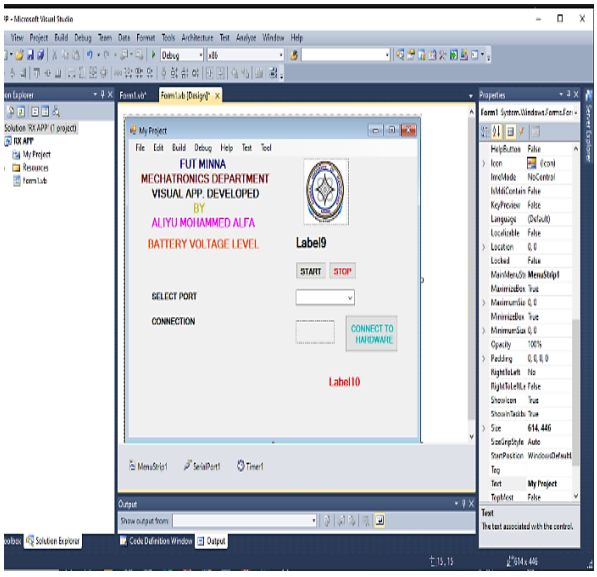

Figure 5: User Graphic Interface

IV. RESULTS AND DISCUSSION

Using the circuit diagram in Figure 1, a prototype of a battery monitoring system was developed. The system's design is depicted in Figure 6. It encompassed the voltage network divider to step down the reference battery voltage, the microcontroller to programmatically control every aspect of the system, a voltage regulator to control the voltage supply to the microcontroller, a transmitter and receiver for wireless signal communication, and a user graphic interface for data collection and storage.

Figure 6: System after final packaging

The Atmega328 ADC port pin enables the ADC sampling from the battery source and convert it to its digital equivalence through the transmitter and the result data is then send to the receiver through the use of wireless module. The final battery voltage reading is depicted in Figure 7 and is shown on a PC system using a VB.NET program. The continuous battery voltage reading value can also be recorded using the VB.net in an Excel spreadsheet, where the obtained values are plotted on a graph.

Figure 8 shows the analog to digital conversion. The amplitude of the graph represents the sine wave of the analog signal and the discrete part of the graph represent the analog digital equivalence. The signal was continuously sample, quantify and then produce its digital form equivalence.

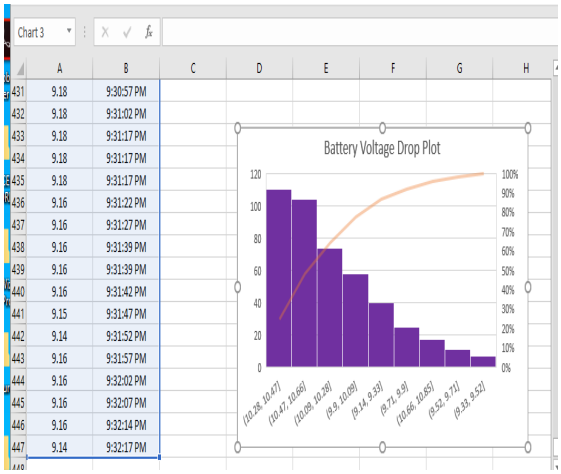

Figure 7: Battery Voltage Drop Plot

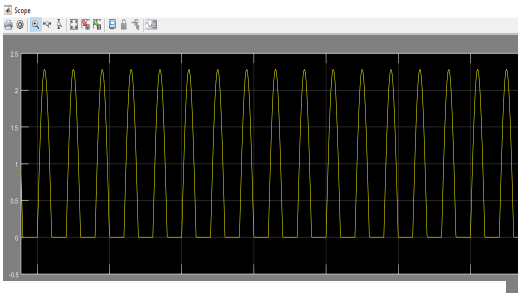

Figure 8: ADC Signal Conversion

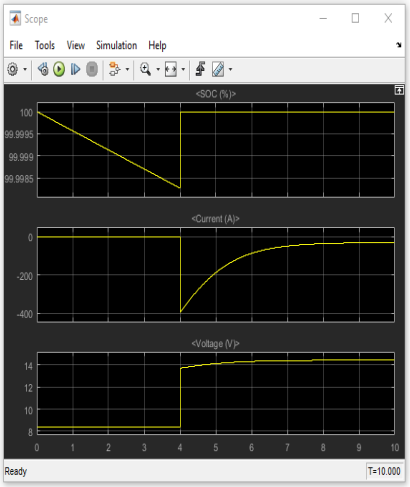

Figure 9: Battery Modelling

The charge state and discharge rate are shown in Figure 9. The first plot represents the battery status with a voltage amplitude of 100 volts, which indicates a charged battery, and over time it continues to slope downward as a result of the load connected to it. The second plot represents the current percentage and it maintains a steady state of 45% before it starts to drop downward, indicating that in the future, there will be a need for recharging. The final graphic displays the voltage state, by the chart, the voltage increases when the load is added from 0 to 100 percent and then gradually falls.

IV. CONCLUSION

As the use of drones to complete complex tasks has increased recently, it is crucial to make sure that the DC battery, which serves as the system's source of power, is a primary concern. The design and development of automatic battery monitoring with an auto-return home was carried out successfully by the earlier stated objectives.

To produce a fully working system design, each component of the system, including the transmitter, receiver, VB.NET app, and wireless data module, was all successfully interfaced.

REFERENCES

Agha, S., Mohsan, H., Qasem, N., Othman, H., & Khan, M. A. (2022). *A Comprehensive Review of Micro UAV Charging Techniques*. 1–30.

Arada, G. P., & Magsino, E. R. (2014). Development of a Power Monitoring System for Backup Lead-Acid Batteries. *Journal of Automation and Control Engineering*, *2*(1), 99–102. https://doi.org/10.12720/joace.2.1.99-102

Conference, N., Innovative, O. N., In, T., & Publications, N. (2019). *New Age Ups With Battery Monitoring Using Raspberry Pi*. *March*, 190–195.

Corral, L., Fronza, I., Ioini, N. El, & Ibershimi, A. (2016). *A Measurement Tool to Track Drones Battery Consumption During Flights*. *November 2018*, 0–12. https://doi.org/10.1007/978-3-319-44215-0

Grey, C. P., & Hall, D. S. (2020). *Prospects for lithium-ion batteries and beyond — a 2030 vision*. 2–5.

https://doi.org/10.1038/s41467-020-19991-4

Khofiyah, N. A., Sutopo, W., & Nugroho, B. D. A. (2019). Technical feasibility battery lithium to support unmanned aerial vehicle (UAV): A technical review. *Proceedings of the International Conference on Industrial Engineering and Operations Management*, *2019* (MAR), 3591–3601.

Kumar, M. R., Arshiya, S. A., Abiya, S. T., & Ananthi, R. (2018). *Battery Monitoring System Using IoT*. *3*(3), 126–128.

Mattada, M., Fatima, S., Viswanatha, V., Rasika, K., & Vishwanath, P. (2022). Smart power management system for uninterrupted power supplies (UPS) with priorities. *Global Transitions Proceedings*, *3*(1), 38–42. https://doi.org/10.1016/j.gltp.2022.04.007

Pham, N. N., Leuchter, J., & Pham, K. L. (2022). *Battery Management System for Unmanned Electric Vehicles with CAN BUS and Internet of Things*. 639–662.

Roslan, N. F., Mariam, W. A. N., & Muda, W. A. N. (2020). *Development of Battery Monitoring System using Arduino Uno Microcontroller*. *2*(4), 41–50.

Series, C. (2020). *Battery monitoring for stand-alone photovoltaic system*. https://doi.org/10.1088/1742-6596/1432/1/012054

Sharif, S., Petros, M., & George, K. (2015). *Remaining Useful Battery Life Prediction for UAVs based on Machine Learning*.

Wild, G., Gavin, K., Murray, J., Silva, J., & Baxter, G. (2017). *A Post-Accident Analysis of Civil Remotely-Piloted Aircraft System Accidents and Incidents*. *9*, 157–168. https://doi.org/10.5028/jatm.v9i2.701

